July 2019

High Enthalpy Storage Thermoset Network with Giant Stress and Energy Output in Rubbery State and Associated Applications

Jizhou Fan
Louisiana State University and Agricultural and Mechanical College, noah.fan@yahoo.com

HIGH ENTHALPY STORAGE THERMOSET NETWORK WITH GIANT STRESS AND ENERGY OUTPUT IN RUBBERY STATE AND ASSOCIATED APPLICATIONS

A Dissertation

Submitted to the Graduation Faculty of the
Louisiana State University and
Agricultural and Mechanical College
in partial fulfillment of the
requirements for the general exam of
Doctor of Philosophy

in

The Department of Mechanical Engineering

by
Jizhou Fan
B.S., Sun Yat-sen University, 2010
M.S., Central Michigan University, 2013
August 2019

ACKNOWLEDGMENTS

I would like to express my sincere gratitude and appreciation to my advisor, Dr. Guoqiang Li, for his guidance, supporting, patience and encouragement during my Ph.D studying period at Louisiana State University. He is not only my academic supervisor, but also the mentor of my life for future. He is the turning point for my academic career. His intelligent, innovated ideas are always out of ordinary thinking and they inspire and guide me to be a real engineer. I also want to thank my committee members Dr. Shengmin Guo, Dr. Genevieve Palardy for the supervising and valuable suggestion. I would also thank Dr. Gernald Schneider who is acting as the Dean's representative for the general exam and the dissertation.

I express my special appreciation for my wife Lu Zhang and my family, who supporting and understanding me emotionally and even more. More thanks are given here for my group members and the technicians who helping me to approach the place where I am today.

Additionally, I thank the following funding agencies for the financially supporting for me and my group including National Science Foundation (NSF), National Aeronautics and Space Administration (NASA). My great thanks are given to the Graduate School of LSU and the Department of Mechanical & Industrial Engineering for the offering Economic Development Award (EDA) for my first four years and the Enrichment Award (EA) for my first three years of my Ph.D study.

TABLE OF CONTENTS

LIST OF TABLES

LIST OF FIGURES

ABSTRACT

In this study, a new shape memory thermoset network with giant stress and energy output in rubbery state is synthesized and studied firstly since the low output in stress and energy in rubbery state has been a bottleneck for wide-spread applications of thermoset shape memory polymers (SMPs). Traditionally, stress or energy storage in thermoset network is through entropy reduction by mechanical deformation or programming. We here report another mechanism for energy storage, which stores energy primarily through enthalpy increase by stretched bonds during programming. As compared to entropy-driven counterparts, which usually have a stable recovery stress from tenths to several MPa and energy output of several tenths MJ/m3, our rubbery network achieved a recovery stress of 17.0 MPa and energy output of 2.12 MJ/m3 in bulk form. Subsequently, this new shape memory thermoset polymer is fabricated into powder and particle for to serve as the expansive additive of the cement used in petroleum industry. Shape memory polymer has been identified and studied as a new generation of the expansive additive for the cement from our previous study. It has showed a good expansion ability and the preservation of the mechanical property. However, for the deeper unground, the higher temperature as the trigger of shape memory effect is necessary. Here we report the new shape memory polymer with the giant stress and energy output can achieve a 1.2% circumferential expansion by adding 6% weight percent in particle form. Moreover, it can enhance the mechanical property in terms of compressive strength, Young's modulus and the compressive strain at the same time which is a rare accomplishment by single type additive. Moreover, the E-glass fiber FRP rebar and the reinforced concrete can be obtained. The curved FRP can produce 77.8 MPa bending recovery stress.

CHAPTER 1. INTRODUCTION

This dissertation consists six chapters. First Chapter introduces the whole dissertation. Second and Third chapters are based on the published paper. The Fourth chapter is based on the preparation of a submitted paper. The fifth chapter is the summary of the completed work and the sixth chapter is the future work of the project summarized in chapter five and the possible exploration of the project in Chapter 2 and 3. The work in each chapter is individually independent but proceeding in an essential logic and step by step with the aim of achieving the final objective of this study. All chapters except this chapter document the process and the result of the Ph.D. candidate under the supervision of the advisor as well as the committee members.

1.1. Motivation

1.1.1. The General Motivation for An Engineer

As the motivation for conventional scientific work, it generally can be considered as two catalogs. Firstly, what is the scientific story behind a phenomenal exiting. As a common term it is mentioned as “why”. The following question as the other catalog is “how to use it”. The people focusing on the different aspect are commonly called “scientists” for the first catalog and some ones are called “engineers” for the second one. As the modern engineers, for completing the real applications and exploring more inventions, to answer both questions is necessary. If a breakthrough you want to achieve, the reason for the limitation and the scientific content behind it will be the first question. After knowing “why”, based on the knowledge and the experience, some innovated ideas will come out. This certainly is not an easy work and sometimes you need some inspiration. Nevertheless, the solid knowledge is the basic start. When some limitation is broken down and some breakthrough you have obtained, to answer the question “how to use it” turns to a more significant job for an engineer. As a material engineer, to break the limitation of the property

of materials and conduct the good materials into appropriate applications are two core jobs. In this study, the logical step by step research is carried out by this idea.

1.1.2. The Motivation for This Study

Shape memory polymer as a class of smart materials have been a topic of intensive research for years. In addition to shape memory, which means a deformed temporary shape can return to its original permanent shape upon stimulation, can also release stress if free shape recovery is not allowed. The fact that SMPs can memorize both shape and stress has rendered them with many potential applications such as actuators, self-healing, sealants, morphing structures, stent, suture, soft robot, smart textile, etc. Considering the practical application, low output in stress and energy in rubbery state has been a bottleneck for wide-spread applications of thermoset shape memory polymers. However, in many applications, higher recovery stress is needed, or higher recovery stress leads to better results such as higher healing efficiency in self-healing applications. Traditionally, stress or energy storage in thermoset network is through entropy reduction by mechanical deformation or programming. The enhancement of stress memory can be achieved by enriching energy storage during programming. Based on the basic thermodynamics, the process of programming either reducing the entropy of system or enhancing the enthalpy of the system. Conventionally, the entropy elasticity is the acknowledged driving force for shape and stress memory in previous SMPs, we believe that storing enthalpy during programming should be a way to further increase the recovery stress and energy output.

Considering the engineering application, this study is not only motivated by the scientific innovation and understanding, it also aims to conduct the shape memory polymer with the improved property into significant product of industry and daily life. As the next step of this study,

the new application by the new shape memory polymer network will be explored. The product for petroleum industry, civil and structural industry etc. is the long-term motivation for this study.

1.2. Objectives

For the first step of this study, to design a new polymer network and find an approach to store the energy from programming into the system by enthalpy is the proceeding objective. Since this idea is not based on the acknowledged agreement of the shape memory polymer, the new understanding and the establish of the theory will be discussed as the next objective.

Once the new polymer is obtained and the theoretical understanding is established, the new shape memory polymer will be used as the expansive additive of cement for oil well in petroleum industry. Moreover, the new thermoset polymer will be also used as the matrix of the fiber reinforced polymer rebar used in concrete beam.

1.3. Research Outline

The research of this study is followed as the following step by step proceeding. The high enthalpy storage thermoset network with giant stress and energy output in rubbery state is investigated firstly. Then, the understanding of this property is summarized as the multiple energy well model. Then, the theoretical understanding in molecular level was studied. Afterwards, the programmed shape memory polymer is fabricated into powder and it serves as the expansive additive of the class G cement. The comprehensive study of this new expansive cement system is conduct. Finally, the new shape memory polymer is manually pultruded with type E glass fiber to form the new fiber reinforced polymer rebar. The mechanical property, shape memory effect and stress recovering are investigated. A summary of the content of each chapter is presented as the followings.

In chapter 2, To obtain a thermoset network with high recovery stress and energy output through enthalpy storage, a commercially available epoxy (EPON 826) was reacted with a rigid diamine named isophorone diamine (IPD), which can provide a large steric hindrance. Beside the conventional study of the shape memory effect, the energy storage and releasing were evaluated. The form and the resource of the energy are confirmed by Differential Scanning Calorimetry (DSC) test, Raman spectroscopy and Near Edge X-ray Absorption Fine Structure (NEXAFS) Spectroscopy.

In chapter 3, the energetical, structural and conformational characteristics during the compression deformation is discussed. The result of the characterization such as stepwise iso-strain programming profile, Raman spectroscopy etc. are understood in molecular level. The possible energy storage and release by classic theory is discussed. The further effort for the conformation of the enthalpy storage is conducted. Consequently, the multiple energy well model for amorphous thermoset shape memory polymers is summarized.

In chapter 4, the new shape memory polymer synthesized by EPON-IPD was programed in the bulky form and then it was fabricated into powder and particle two forms to serve as the expansive additive for the class G cement, which is common cement used in the oil well sheath. The expansion ability and the mechanical property are estimated. For evaluating the mixability and pumpability, the rheology property is also tested. The dispersion and interaction between the additive and the cement is also studied by end notched flexure method, scanning electron microscopy and X-ray photoelectron spectroscopy.

In chapter 5, the study of the fiber reinforced polymer rebar made of EPON-IPD and glass fiber is presented. The volume fraction for glass fiber as high as 70% can be obtained. The shape memory effect and mechanical property are tested for the curved FRP. The bending recovering

stress are tested. The straight FPRs with another layer as the thread were used as the rebar for the concrete beam and the three-point bending test were conducted and the cracking mode was observed.

In the chapter 6, the future work is discussed based on the result in the chapter 5. Also, the expansive study for the chapter 2 and 3 is also presented.

CHAPTER 2. HIGH ENTHALPY STORAGE THERMOSET NETWORK WITH GIANT STRESS AND ENERGY OUTPUT IN RUBBERY STATE

2.1. Introduction

Shape memory polymers (SMPs) have been a topic of intensive research for years [1-10]. In addition to shape memory, which means a deformed temporary shape can return to its original permanent shape upon stimulation, such as heat [11], light [12], moisture [13], pH [14], etc., SMPs can also release stress if free shape recovery is not allowed [1]. The fact that SMPs can memorize both shape and stress has rendered them with many potential applications such as actuators, self-healing, sealants, morphing structures, stent, suture, soft robot, smart textile, etc. [1-10]. While many stimuli approaches have been used in SMPs such as host-guest transition [15], anisotropic-isotropic transition [7], etc., thermal transition has been the most popular method because some other methods such as electricity and magnetic field also cause indirect heating [2,16]. Heat induced shape memory effect is triggered primarily by glass/verification transition and melt/crystallization transition [7]. For thermally triggered SMPs, a bottleneck is the low recovery stress [17]. From Table 2.1, which summarizes several thermoset SMP systems cited as having very high stabilized recovery stress in the literatures, the majority exhibit stabilized recovery stress from tenths MPa to several MPa [1-10]. However, in many applications, higher recovery stress is needed, or higher recovery stress leads to better results such as higher healing efficiency in self-healing applications [18].

For classical SMPs with glass transitions, entropy has been identified as the driving force for shape or stress recovery [1,2]. During the transition from glassy state to rubbery state for amorphous thermoset polymers, it is not uncommon to see one to two orders decrease in the modulus of the polymers. The dramatic reduction in modulus through the transition is necessary for the SMP to demonstrate excellent shape recovery; however, it sacrifices stress recovery. The

Table 2.1. The stress release and energy output in rubbery state for typical compression programmed pure thermoset shape memory polymers, recovery stress and energy output of a shape memory alloy, and energy output of typical elastically deformed metals.

Material Type	**Recovery Stress (MPa)**	**Real Energy Output* (MJ/m^3)**	**Over-Estimated Energy Output** (MJ/m^3)**	**Pre-strain of Compression programming**
EPON-IPD	17	2.12	3.82	45%
(meth)acrylate [19]	~1.5	N/A	~0.23	30%
Styrene based crosslinked SMP [20]	0.5	N/A	0.13	50%
Epoxy (TEMBO) [21]	0.12	N/A	0.05	80%
304 stainless steel [22]	N/A	0.10	N/A	1%
Ductile cast iron [22]	N/A	0.46	N/A	2.3%
Red brass [22]	N/A	0.83	N/A	4%
Shape memory alloy*** [23]	240	N/A	3.96	3.3%
PCL-2T-MA**** [24]	N/A	1.5	N/A	400%

*The real energy output is calculated by the area of the enclosed by the recovery stress-recovery strain curve for polymers. For metals, it is calculated by the elastic part of the area of stress-strain curve.

** The over-estimated energy output is calculated by the area of the right triangle determined by the fully constrained recovery stress and free shape recovery strain as the two vertexes of the right triangle.
***Tension programming (assuming modulus of elasticity of 85GPa, and 100% recovery ratio).
****Tension programming to 400%; the 1.5MJ/m^3 energy is storage energy.

flexible rubbery state suggests that the SMP can only release a low stress. In other words, for higher recovery stress, the SMP in rubbery state must be stiffer; however, it may suffer from lower shape memory. Therefore, for entropy driven SMPs with thermal transitions, the contradictory requirement between recovery strain and recovery stress renders most thermoset SMPs with excellent shape memory but poor stress memory. Therefore, it is a grand challenge on how to increase the stress memory while maintaining excellent shape memory. Ideas other than entropy driven must be sought.

The enhancement of stress memory can be achieved by enriching energy storage during programming. Based on the basic thermodynamics, $\Delta G = \Delta H - \Delta TS$, where ΔG, ΔH and ΔS are the change of Gibbs free energy, enthalpy and entropy, respectively, and T is the absolute temperature; hence, the stored energy consists of both entropy and enthalpy. Obviously, stress recovery and energy output depend on the energy input during programming and the energy storage in the temporary shape after programming [17]. Because entropy elasticity is the acknowledged driving force for shape and stress memory in previous SMPs, we believe that storing enthalpy during programming should be a way to further increase the recovery stress and energy output.

2.2. Experimental Section

2.2.1. Synthesis of High Enthalpy Storage Thermoset Shape Memory Polymer

Due to the attractive potential as a mechanical actuator in future structural applications, a two-component thermoset network was chosen as the representative model polymer in this study. To uncover the relationship between the conformational, structural, energetical and mechanical characteristics at molecular level, a pure polymer network without reinforcing filler is an

appropriate object. Commercially available epoxy (EPON 826, DuPont, USA) was used as the first component in the network. To enhance the enthalpy storage, intense steric hindrance is necessary to construct a stiff network. To prevent from losing stoichiometry during the reaction, a high reacting efficiency is required. Therefore, a rigid isophorone diamine (IPD), named as 5-Amino-1,3,3-trimethylcyclohexanemethylamine (Sigma-Aldrich, USA), was selected as the other component in this network. Because the functionality of epoxy is two while the functionality of diamine is four, each 100g EPON 826 was reacted with 23.2g IPD to balance the stoichiometry. The reagents were mixed by a mechanical mixer for two minutes at room temperature, and then were placed into a rectangle Teflon mold. The air bubbles were extracted by vacuum at room temperature. After one hour curing under 150°C, a thermoset network was obtained.

The reagents are shown in Figure 2.1 and the reaction pathways are illustrated in Figure 2.2, respectively.

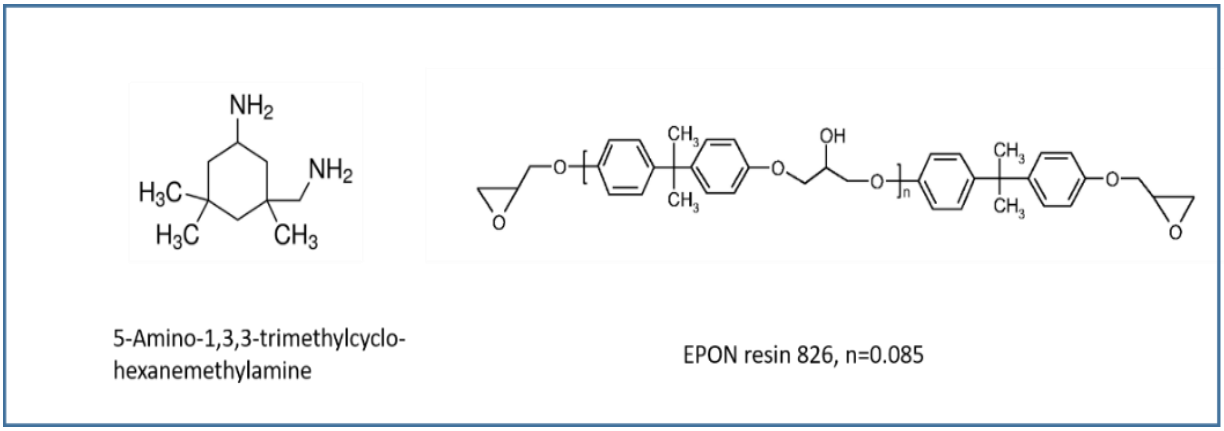

Figure 2.1. The molecular structure of the chemicals for the reaction.

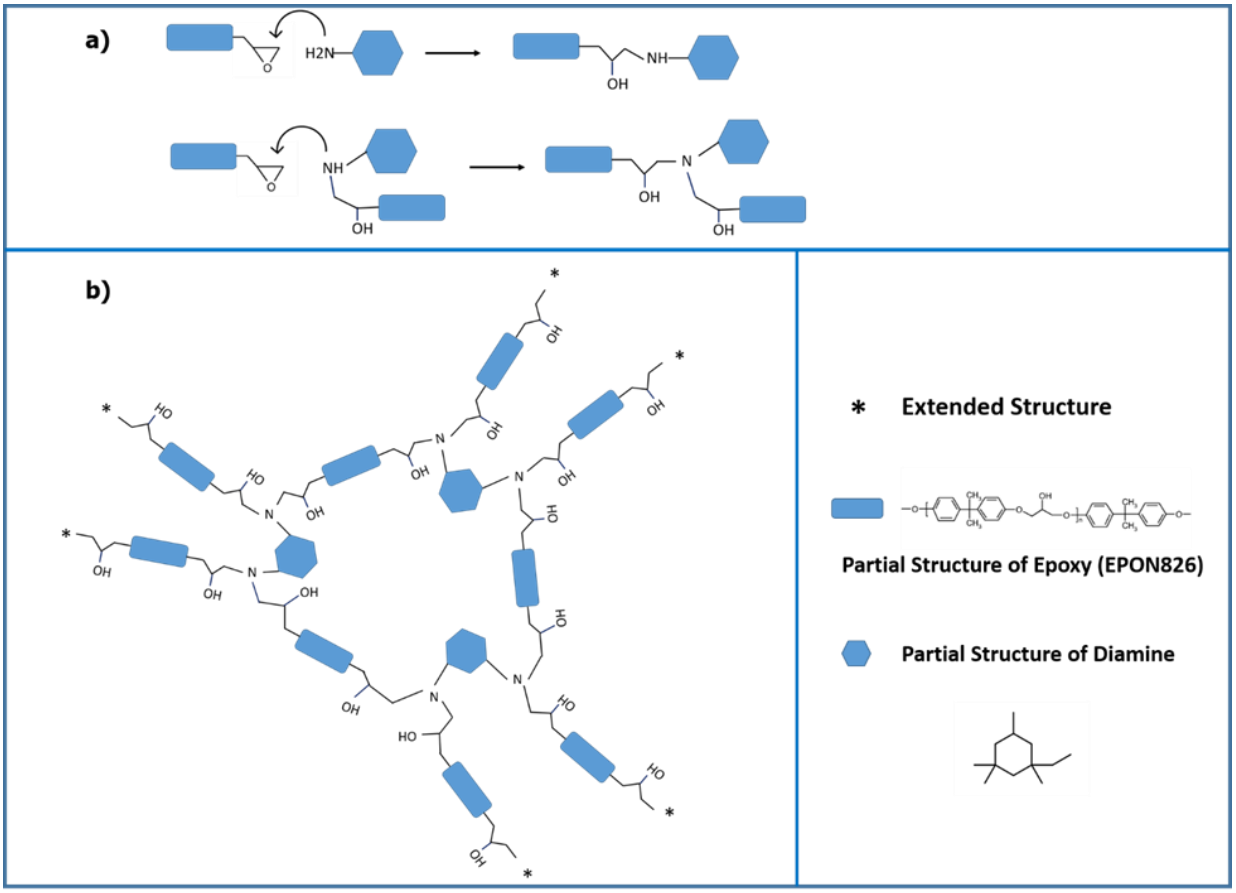

Figure 2.2. The possible reaction pathway for the EPON-IPD network. The part (a) presents how one amino group reacts with an epoxy group. The part (b) shows the network formed by nine EPON 826 molecules and three IPD molecules. The stars indicate the extension of the rest of the network.

2.2.2. Method for Thermal and Thermomechanical Property Characterization of the Synthesized Polymer Network

2.2.2.1. Differential Scanning Calorimetry (DSC) Test

The DSC test was performed by DSC 4000 (PerkinElmer) for the investigation of the thermal behavior of the synthesized polymer network and the enthalpy release for the programed sample. The glass transition range and glass transition temperature were determined by the second heating branch. The temperature scan was conducted as following steps: (1) equilibrate at 30°C for three minutes, (2) heat to 170°C, (3) equilibrate at 170°C for three minutes, (4) cool down to 30°C, and

(5) equilibrate at 30°C for three minutes. Then the heating and cooling cycle is repeated from step 2 to step 5. All heating and cooling rates were controlled as 10°C/min.

2.2.2.2. Dynamic Mechanical Analysis (DMA)

The thermomechanical property of the synthesized polymer network was analyzed by a TA Instruments Q800 Dynamic Mechanical Analyzer. Using the multi-frequency mode, the three-point bending test was carried out with fixed displacement. The temperature was scanned at a rate of 10°C/min.

The thermal expansion behavior was also measured by the DMA under the controlled force mode. The fixture was changed to the tensile clamps. The cyclic temperature was scanned from -25°C to 180°C.

2.2.3. Sample Preparation and Programming

2.2.3.1. Sample Preparation and Compression Programming

A perfect alignment is a significant factor for the uniaxial compression test. Hence, the cured bulky polymer network was cut and then carefully milled into a cuboid. The tolerance for each pair of parallel surfaces was less than ten micrometers. All edges of the cuboid samples are between 6.5 mm and 7.5 mm.

Uniaxial compression programming was then conducted. Before this process, the oven, specimen and fixture have already been heated at 170°C for over an hour, to avoid the effect of thermal expansion. The compression process is shown in Figure 2.3. Step one represents the relationship between the stress and strain during the compressive deformation up to 45% strain at 170°C. After this, stress relaxation occurred in step two (Note: in the literature, step 1 and step 2 are usually treated as one step. For clarity of presentation, we divided them into two steps). The step three shows the relationship between stress and temperature during the cooling process, while

holding the strain constant. The air-cooling process was performed by opening the door of the oven only. It is interesting to note that the unloading step, which is needed for a typical programming, is coupled with the cooling step. The load becomes zero at about 80°C, due to thermal contraction of the specimen. The compression programming was completed when the temperature drops to room temperature.

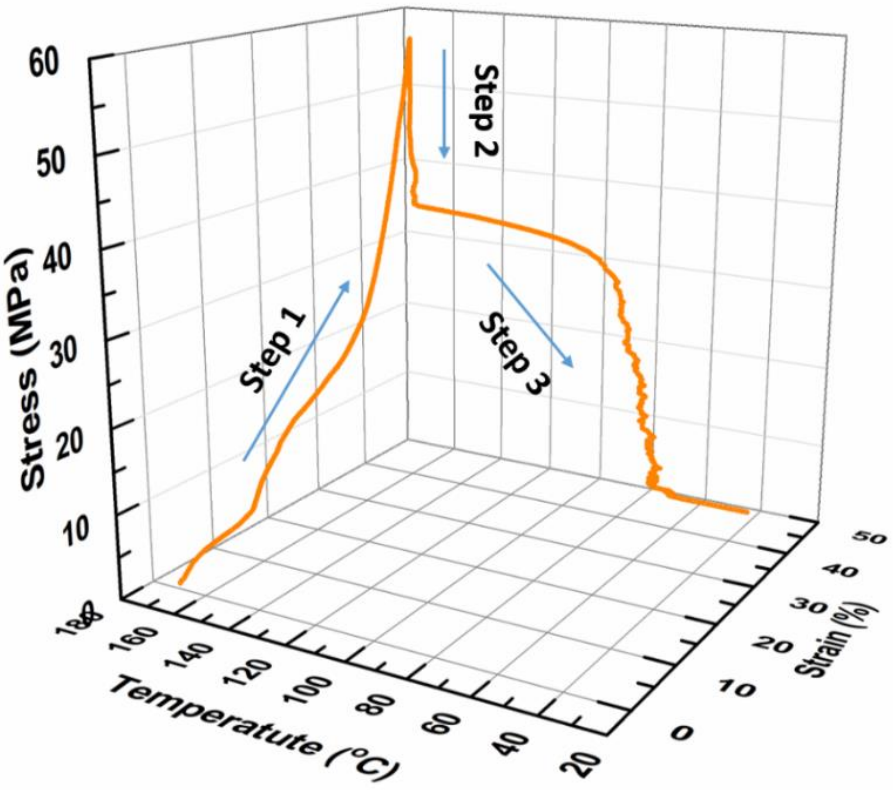

Figure 2.3. The relationship between stress-strain-temperature during the compressive programming at 170 °C (step 1), the stress relaxation at 170°C (step 2) and the cooling and unloading process (step 3).

2.2.3.2. Sample Preparation and Tension Programming

During tensile programming, the specimen with a dimension of 14.5 mm × 50 mm × 5mm was mounted onto one end of the grips of the mechanical test machine before the oven was equilibrated at 170°C for an hour. Then, the specimen was fixed by tightening the other end of the

grips and tensile programming was executed. The specimen was stretched to 10% strain at 170°C. After holding for 10 minutes, the pre-stretched specimen was cooled down quickly to room temperature by spraying water onto the specimen while holding the programming strain constant. The load was then removed to fix the programed shape.

2.2.4. Fixity Ratio Test

In order to understand the shape fixity capabilities of the SMP, we have tested the shape fixity ratio of the polymer at different programming strains. Both the mean and standard deviation are given. Each shape fixity ratio in the table is the average of the test results of three compression programming with the same programming strain. The compression programming was conducted at 170°C.

2.2.5. Shape Memory Effect and Recovery Stress Test

2.2.5.1. Free Shape Recovery Test

Free shape recovery, as an important feature of shape memory polymers, is influenced by the deformation manner during the programming process. The polymer network in this study was an entirely continuous network. Permanent deformation rarely happens except for breaking the chemical bonds. Consequently, without defect and damage of the network, the free recovery should reproduce the permanent shape. To test this property, the sample, prepared in last section, was compressed by the Mechanical Testing System (MTS) QTEST 150 machine for 40% of strain at 170°C. After the sample was cooled down to room temperature and unloading, it was placed back into the oven and was heated up to 170°C to trigger the free shape recovery.

2.2.5.2. Fully Constrained Stress Recovering

The fully constrained recovery stress of a shape memory polymer indicates the potential as a mechanical actuator for future structural applications. Recovery stress is obtained by heating the

network to above the glass transition temperature (in rubbery state), but without allowing any recovery strain. In order to obtain the stabilized recovery stress, the specimen was held at the recovery temperature for hours. To investigate this property, the fully constrained recovery stress test was conducted on specimens programmed by 45% compressive strain. The test was conducted by the MTS QTEST 150 machine for 8 hours. Before placing the programmed sample into the oven, the inside environment of the oven has been stabilized at 170°C for one hour.

2.2.5.3. Study for the Effect of Programming Temperature of Recovery Stress

To consider the effect of programming temperature on the recovery stress, two types of additional compression programming were conducted. In one type, a new compression programming at the glass transition region (150°C) has been conducted. The pre-strain is 45%, and the fixed strain is 41.8%, which is almost the same as the fixed strain by programming at rubbery state (170°C) with the same pre-strain 45%. The similar fixed strain makes the comparison meaningful.

In the second type of programming, three specimens were programed into the same fixed compressive strain which was 32% at different temperatures (20°C (glassy state), 150 °C (glass transition zone), and 170 °C (rubbery state)). All the programmed specimens, then, were recovered at 170°C under the fully constrained conditions.

2.2.5.4. Relationship between Recovery Stress and Recovery Strain

A significant advantage for shape memory polymers, as compared to shape memory alloys (SMAs) or ceramics, is their large recovery strain. While SMAs have a very high fully constrained recovery stress, may be in hundreds of MPa, their free recovery strain is very small, may be less than 10%. Eventually, SMPs may output comparable energy against SMAs [25]. For shape memory materials, fully constrained recovery stress and free shape recovery strain are the two

extreme cases of measuring their memory capability. If recovery strain is allowed, the recovery stress will be reduced. In many applications, stress recovery must be accompanied by strain recovery, such as using shape memory effect for closing wide-opened cracks in self-healing applications or as actuators. Therefore, it is highly desired that SMPs have high recovery stress with considerable recovery strain. Actually, the area generated by the recovery stress – recovery strain curve is a direct measurement of the energy output. To obtain the relationship between recovery stress – recovery strain, the recovery stress at different recovery strains is tested as follows. A fully constrained recovery stress test for samples programmed by 45% strain was used to obtain one boundary point in the recovery stress – recovery strain curve, here zero recovery strain. The value of the recovery stress was measured after the stress was stabilized for 1.5 h at 170°C. Another boundary point is the free shape recovery test, here zero recovery stress. The samples were allowed to recovery free of constraint in the oven at 170°C for half an hour. For other points in the recovery stress – recovery strain curve, the clamp of the MTS machine was positioned to allow 2.5%, 7.5%, 12.5%, 17.5%, 22.5%, and 32.5% recovery strains, respectively. All the tests were conducted at 170°C for 30 – 40 minutes to obtain stabilized recovery stress. The exact recovery time was determined by the variation of the stress. When the change of the recovery stress was less than 0.01MPa in 10 minutes, the value was taken and the test was stopped. The whole process was repeated for three different samples.

2.2.6. Stress Relaxation, Strain Effect and Mechanical Behavior Test

2.2.6.1. Stress Relaxation Behavior at Different Temperature Zones

At room temperature, the polymer network, which is in glassy and non-equilibrium state, will also relax to the equilibrium state although it will take a very long time. This circumstance is referred to as physical aging. At a high temperature, especially when it is close to the glass

transition zone, the relaxation is accelerated significantly. Thus, to analyze the compression behavior during programming, the relaxation performance is needed. The stress relaxation test was conducted at four different temperatures, which were 120°C, 155°C, 170°C and 175°C. All samples were compressed to 40% strain, and then the deformation was maintained to let the stress relaxation occur. All relaxation data were normalized by the peak stress, σ_0, obtained at the end of compression. Although the higher temperature softens the thermoset network more, the intense steric hindrance helps the electrons pack more tightly. Consequently, the network is stable at even higher temperatures and this is one of the reasons for the giant stress recovery at rubbery state.

2.2.6.2. Strain Rate Effect on Stress Storage

Due to the time-dependent behavior of the polymer network, loading rate should have an effect on the relaxation behavior. We have conducted the stepwise stress relaxation test with three strain rates: 0.1mm/mm/min, 0.25mm/mm/min, and 0.5mm/mm/min.

2.2.6.3. Mechanical Behavior at Room Temperature

Most applications of SMPs require that they work at ambient temperature. Hence, the mechanical property at room temperature is important. SMP samples were compressed until fracture at room temperature by the MTS QTST 150 machine. The strain rate was 1mm/min.

2.2.6.4. Tensile Behavior at Rubbery State

The tensile stress-strain behavior of the SMP was also investigated at rubbery state. The specimens were fabricated into a rectangular shape with a dimension 14.5 mm × 50 mm × 5mm. The strain is calculated by the gauge length of 15mm of the specimen, which is the length between the two marks. The test temperature was 170°C, and the strain rate was 0.03 mm/mm/min. One can see that the polymer can only be stretched by about 12% strain before it fractures at 170°C. The peak stress or tensile strength of the SMP is about 7.1 MPa. Therefore, when we tested the

tensile recovery stress of the SMP, we selected 10% strain as the tensile programming pre-strain at 170°C.

2.2.7. Stepwise Iso-strain Compression-relaxation Test

Temperature, as a critical parameter affecting the mechanical properties of polymers, can be separated into different regions around the glass transition. When the temperature is lower than the glass transition zone, sufficient energy input is needed to render the coordinated segmental rotation to occur. Within the glass transition zone or at even higher temperatures, the bond rotation can happen at any strain because the thermal energy has already overcome the energy barrier for segmental bond rotation. Therefore, the deformation applied is an energy source to compel the polymer network into a non-equilibrium and locally high energy state. The relaxation will happen to stabilize the total energy towards a locally low energy state simultaneously. Thus, the characteristics of the relaxation is associated with the conformational and structural evolution during deformation. However, the relaxation reflected on the testing machine is always delayed because the relaxation is time dependent. Hence, to uncover the conformational and structural variation hidden during the deformation, a stepwise iso-strain compression-relaxation test was performed as follows. The sample was equilibrated in rubbery state, which was 175°C, before compression. In each step, two percent compressive strain was applied, and then relaxation was allowed for four minutes. The sample was compressed for a total of forty-four percent of strain. This test was conducted by the MTS QTEST 150 machine with an assembled oven controlled by a Eurotherm Controller (Thermodynamic Engineering Inc. Camarillo, CA).

2.2.8. Characterization of Bond Length Change

2.2.8.1. Raman Spectroscopy

Raman Spectroscopy, as a characterization method for the vibrational energy of chemical bond, is a very useful tool for revealing the variation of the bond length [26,27]. In this study, bond length is a significant parameter for enthalpy storage. After programming (rubbery state compression, cooling and unloading), a temporary configuration is fixed in the network. Whether or not the bond length has been changed can be observed by Raman Spectroscopy at room temperature. The measurements for the samples programmed by different strains were performed by LABRAM integrated Raman spectroscopy system manufactured by Johin Yvon Horiba. The 1mW He-Ne Laser was used as the excitation probe and the wavelength was 632.81nm. Both focusing and collecting the backscattered light were carried out by a 10× objective lens. The chemical shift was scanned from 800 cm^{-1} to 1300 cm^{-1}. The shifting of peaks is labeled with the type of bond. Both qualitative and semi-quantitative result can be obtained.

2.2.8.2. Near Edge X-ray Absorption Fine Structure (NEXAFS) Spectroscopy

To further confirm the change of bond length, the NEXAFS technique was also used. NEXAFS as a specific element related technique can resolve the electronic structure of molecule or molecular fragments [28, 29]. Carbon is the main element in the synthesized polymer network. Therefore, the C 1s K-edge spectrum was collected and used for the analysis of carbon involved bonds. The first peak was identified as the C 1s→ π* (C=C) peak at 285.4 eV by polystyrene. The spectrum collection was carried out by the GEOL 7900 X-ray absorption spectrometer associated with the low energy beamline from the synchrotron located at the Center for Advanced Microstructures and Devices (CAMD), Baton Rouge. The grounded polymer powder was mounted on the copper tape as the testing sample. Subsequently, the sample was anisotropic and the shifting

of the peak in the spectrum was due to the variation of the bond length only. The compressed polymer network by different strains was milled by sandpaper gently in a -20°C environment to reduce the heat produced by friction.

2.2.9. Steric Hindrance

To prove the argument of the "steric effect", we take four steps. Step 1, based on the knowledge of organic chemistry and the chemical networks that have already been investigated, we assume that a certain group or groups provide the significant steric effect to the EPON-IPD network. Step 2, we find a diamine molecule with the exact or very similar structure but without the groups which are assumed to supply the steric hindrance. Step 3, we react the new diamine with the EPON826 and obtain a new thermoset network. Step 4, we test the thermal property, recovery stress and the energy storage mechanism to check if our argument of the "steric effect" is correct or not.

The first three steps are illustrated as the Figure 2.4. We assume that the groups providing the significant steric hindrance are the methyl groups in the IPD molecule including position one and position three (the ones with scissor). The ideal diamine is the molecule without these three methyl groups as shown in Figure 2.4. By searching the available and commercialized molecules, the 1,3-Bis (aminomethyl)cyclohexane (BACH) is chosen as the model diamine because it is a very similar molecule with the ideal structure but without the high steric hindrance (methyl groups); see Figure 2.4. To keep stoichiometry, the molar ratio of EPON and BACH is two to one.

In step 4, the thermal property of the synthesized EPON-BACH network is tested by DSC. With the same method as that used for the EPON-IPD network, the new thermoset polymer is compression programmed into 45% pre-strain. The recovery stress is also investigated. The only difference here is the temperature for the programming and recovery which is 160°C, other than

170°C for the EPON-IPD network. The 160°C is 10 °C higher than the end-set point for the glass transition region for the EPON-BACH, which ensures that the programming and the recovery occur at the rubbery state for this new thermoset polymer.

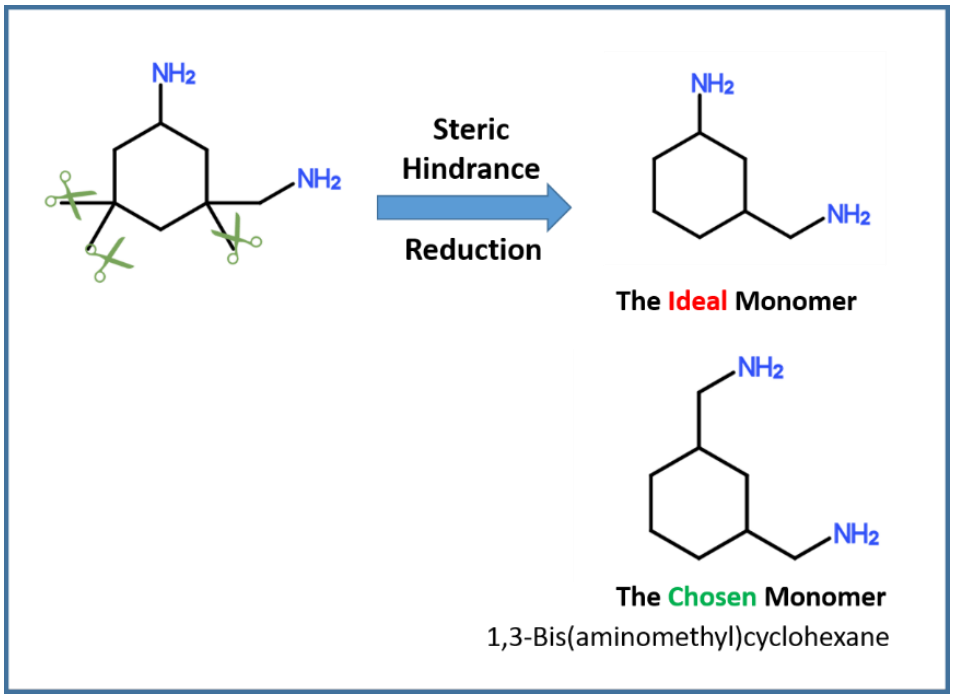

Figure 2.4. The ideal and the chosen monomer (diamine) to prove the resource of the steric effect.

2.3. Results and Discussion

The free shape recovery test is illustrated as the Figure 2.5. The fixity ratios by different programming pre-strains are listed in the Table 2.2.

Figure 2.6A shows the fully constrained stress recovery test results. The maximum recovery stress, as high as 17 MPa in rubbery state, was obtained and maintained. The recovery stress versus recovery strain through partially constrained shape recovery test is plotted in Figure 2.6B. Based on Figure 2.6B more than 6 MPa stress can still be maintained even when the programmed sample with 45% pre-strain is allowed to recover 10% of strain. This stress is adequate to drive crack

closure in real world applications [18]. Based on this recovery stress - recovery strain curve, the energy output, i.e., the area included by the recovery stress - recovery strain curve, is calculated to be 2.12 MJ/m^3, which is much higher than other thermoset SMPs or even elastically deformed metals and is even comparable to some shape memory alloys (SMAs), as given in Table 2.1.

Table 2.2. Shape fixity ratios of the samples with different compression programming pre-strains.

Compressive Programming Pre-strain (%)	10	20	30	40	45
Shape Fixity ratio (%)	89.3 ± 5.3	87.9 ± 4.0	88.3 ± 3.2	84.9 ± 2.1	89.6 ± 2.2

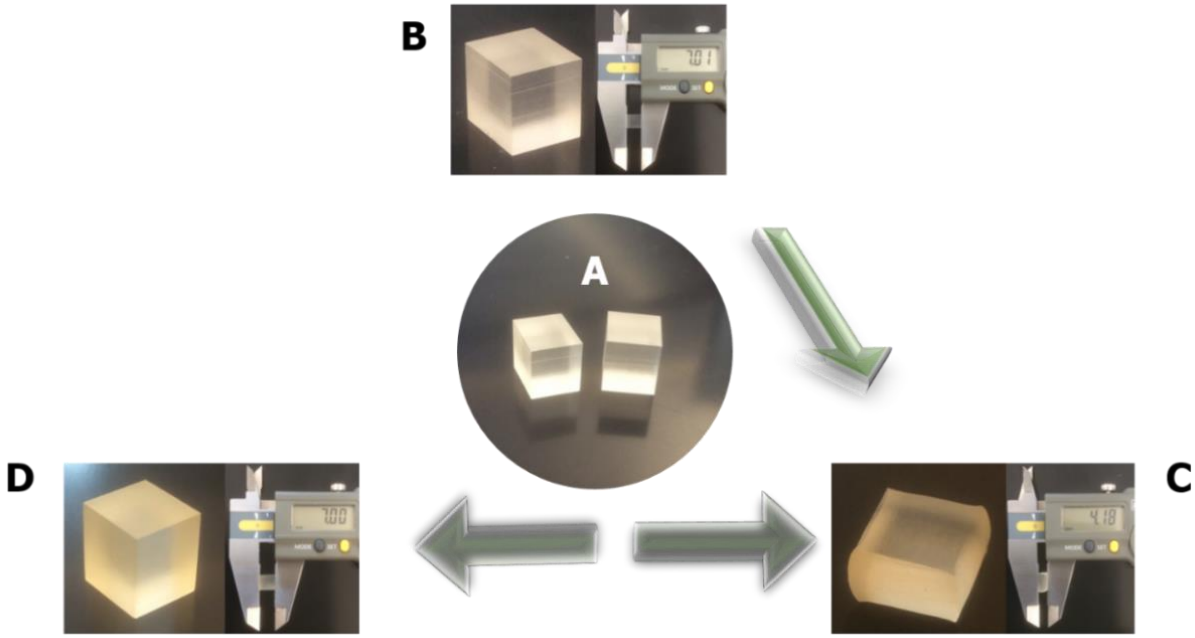

Figure 2.5. The prepared samples and the free shape recovery test. (A) The cut and milled cuboid samples. (B) The sample before the compression programming, which shows that the side length of the cuboid sample is 7.01 mm. (C) The sample after programming, which is compressed by 40% strain, and the height of the cuboid sample is 4.18 mm. (D) The sample after the free shape recovery, almost fully restoring the original permanent shape (the side length becomes 7.00 mm after free shape recovery as compared to original length of 7.01 mm). This suggests that the high enthalpy storage network has excellent shape memory ability.

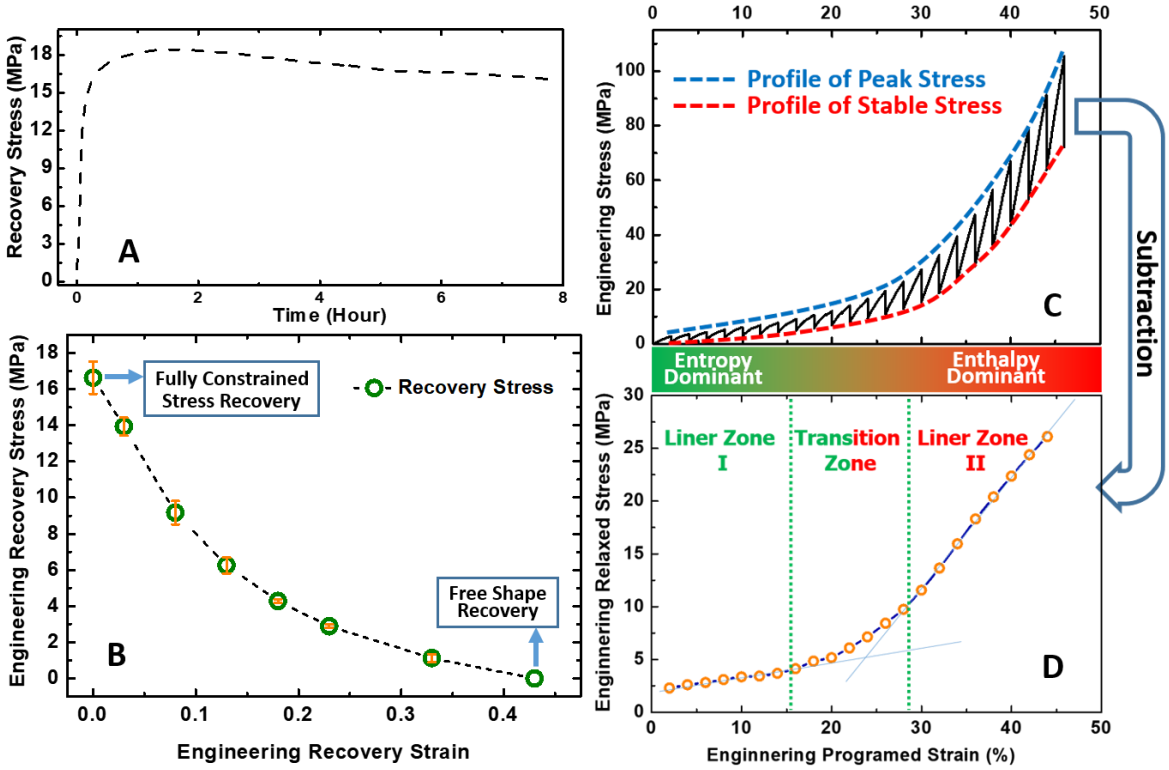

Figure 2.6. The stress and energy storage and recovery behavior for the high enthalpy storage thermoset shape memory polymer. (A) The fully constrained stress recovery profile in rubbery state (recovered at 170°C for 8 hours; the glass transition zone is between 140°C – 160°C) for a sample compression programmed with 45% pre-strain at a strain rate of 0.5mm/mm/min and temperature of 170°C. The recovery stress in the rubbery state is about 17.87 MPa at 1.0 hour, 17.0 MPa at 1.5 hours, and 16.07 MPa at 8 hours. (B) The relationship between the recovery stress and recovery strain (the recovery stress was taken at 1.5 hours). The test procedure is given in section 4.3 in the Supplementary Materials. The free shape recovery ratio was 99.9%. The energy output, which is calculated based on the area of the recovery stress-strain curve, is about 2.12 MJ/m^3. (C) The stepwise iso-strain programming profile. In order to elucidate the different modes for energy storage, step-wise iso-strain compression programming was also conducted. In each step of loading, the strain increases; the stress then relaxes while holding the strain constant, which completes the one loading-relaxation cycle. In each step, the sample was compressed to 2% strain and then let it relax for 4 minutes. (D) The change of programming stress after relaxation, or stored stress, with programming strain. The stored stress increases as the programming strain increases, which suggests that more energy input leads to more energy storage, and thus higher recovery strain and higher recovery stress. The stored energy is calculated by the area of this relaxation stress-strain curve, which is 4.10 MJ/m^3.

Figure 2.6C shows a stepwise iso-strain programming experiment or stepwise stress relaxation test in order to reveal the energy storage mechanism in this thermoset network. We conducted this experiment because stress relaxation is a mechanism for energy storage during programming [30].

In each step, the sample was compressed to 2% strain and then let it relax for 4 minutes. Subtracting the stabilized stress (stress after relaxation) from the peak stress in each step, the stress relaxation profile is obtained, as shown Figure 2.6D. Two distinct linear zones, separated by a transition zone, can be identified. The slope of the second linear zone, which represents the relaxed modulus of the polymer, is much higher than that of the first zone. This is a physical evidence that this thermoset network has a giant recovery stress. The three zones in Figure 2.6D indicate that the energy storage follows two different mechanisms during the programming process. In Linear Zone I (LZ1), the energy is stored through entropy reduction. In the Transition Zone (TZ), the energy storage is through both entropy reduction and enthalpy increase, but gradually with more and more share by enthalpy as the programming strain increases. In Linear Zone II (LZ2), the energy is primarily stored by increase in enthalpy. From Figure 2.6D, the stored energy, which is the area included by the relaxation stress-strain curve, is calculated to be 4.10 MJ/m^3. Therefore, the energy output efficiency is 2.12 MJ/m^3 / 4.10 MJ/m^3 = 51.71%.

The energy storage mechanism can also be understood at the molecular level. The synthesized EPON-IPD network can be treated as a continuous elastic body in rubbery state when the unreacted residual monomers and defects are neglected. From low to high energy state, only three molecular structural parameters, which are the dihedral angle, bond length, and bond angle, can be changed during the programming process [31]. The dihedral angle can be changed by bond rotation; while the change in bond length and bond angle might happen by stretching, compressing or bending the chemical bonds. In general, bond angle is determined by the type of orbiters such as sp2, sp3, etc., and it is the most difficult parameter to change. Therefore, it is assumed that bond angles are constant in this study. During mechanical deformation (programming), the parameter with low energy state can be changed first, which is the dihedral angle. Each change in the dihedral angle

leads to a new, ordered or aligned conformational configuration of the network, or entropy decrease, which corresponds to the LZ1 in Figure 2.6D. With further deformation, the dihedral angle change becomes more difficult because (1) the free volume is reduced; and (2) the available conformational configurations become less. Therefore, the deformation is shifted gradually towards bond length change. Clearly, bond length changes do not render new conformational entropy changes, but they increase enthalpy. This gradual shift from entropy decrease to enthalpy increase corresponds to the TZ in Figure 2.6D. With higher programming strain, the energy will be primarily stored by the bond length change, i.e., enthalpy increases, leading to the LZ2 in Figure 2.6D. The bond length starts to change in TZ and change more in LZ2 are confirmed by the Raman Spectroscopy and Near Edge X-ray Absorption Fine Structure Spectroscopy (NEXAFS) as shown, respectively.

Figure 2.7 confirms enthalpy release during free shape recovery by differential scanning calorimetry (DSC) tests. Two thermal cycles were conducted for the un-deformed (control) and 40% compression strain programmed samples. Both samples show the same glass transition region in the second heating curve, because the first heating cycle has eliminated the history of programming. For the programmed sample, a high enthalpy release is confirmed by the inverse peak presenting in the first heating curve. The release starts at the on-set point of the glass transition zone sharply. Considering both the baseline shifting and the normal glass transition, the total specific enthalpy released by the stretching bond is -2.85 J/g. The negative sign means energy release. Considering that the density of the sample is 1.142 g/cm^3, the enthalpy release density is 3.25 MJ/m^3. Compared with the total energy stored in the system, which is 4.10 MJ/m^3, it is found that 79.3% (3.25 MJ/m^3 / 4.10 MJ/m^3) of the energy stored is in the form of enthalpy.

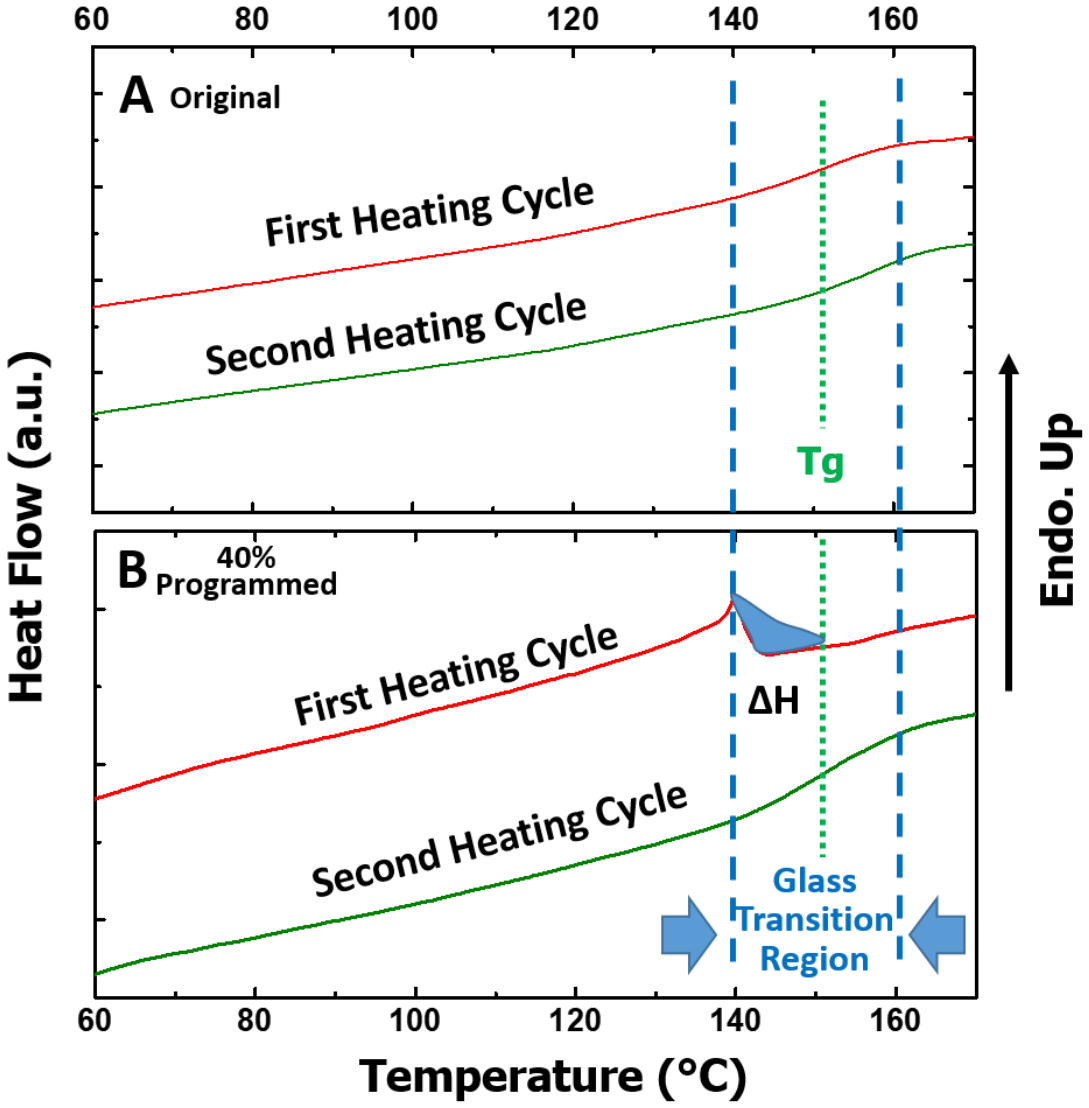

Figure 2.7. The testing and confirmation for the enthalpy release during the free shape recovery process by DSC. (A) The DSC test results for the original SMP after the synthesis. To avoid the post-curing and to match the thermal history with the programmed sample, the sample of original SMP was heating at 170 °C for over one hour before the DSC test. The typical glass transition curve, glass transition region, and glass transition temperature can be identified in the second heating cycle. (B) The DSC test results for the 40% compressive strain programmed sample. An inverse peak emerges during the first heating cycle in the pre-T_g region. The enthalpy release is confirmed by this first order transition. This is due to the retreat of stretched bonds formed during programming, which leads to release of the stored enthalpy, and the enthalpy release is ΔH = -2.85 J/g. The negative sign means the release of enthalpy. After release of the stored enthalpy, the second heating cycle also presents the classical second order glass transition curve. Based on the density of the sample, the specific enthalpy storage is 3.25 MJ/m^3. Determination of the end points and baseline for calculating the enthalpy can be found in Figure 2.8.

The enthalpy calculation based on the DSC curve depends on the selection of the baseline and the endpoints. Unlike melting or crystallization, which have a clear peak and usually the associated software in the DSC machine can automatically calculate the enthalpy, glass transition (second order transition) is signified by a change in the base line, indicating a change in the heat capacity of the polymer. In order to determine the end points of the transition zone, the baselines before and after the transition are extrapolated; see the two dashed pink lines in the second heating cycle curve in Figure 2.8. Then the glass transition zone is determined as the temperature range at the intersection of the extrapolated baselines and the line extrapolated from the linear portion during the phase transition (dashed red line in the second heating cycle in Figure 2.8). The intersections of the dashed red line and dashed pink lines were treated as the end points of the glass transition region in this study.

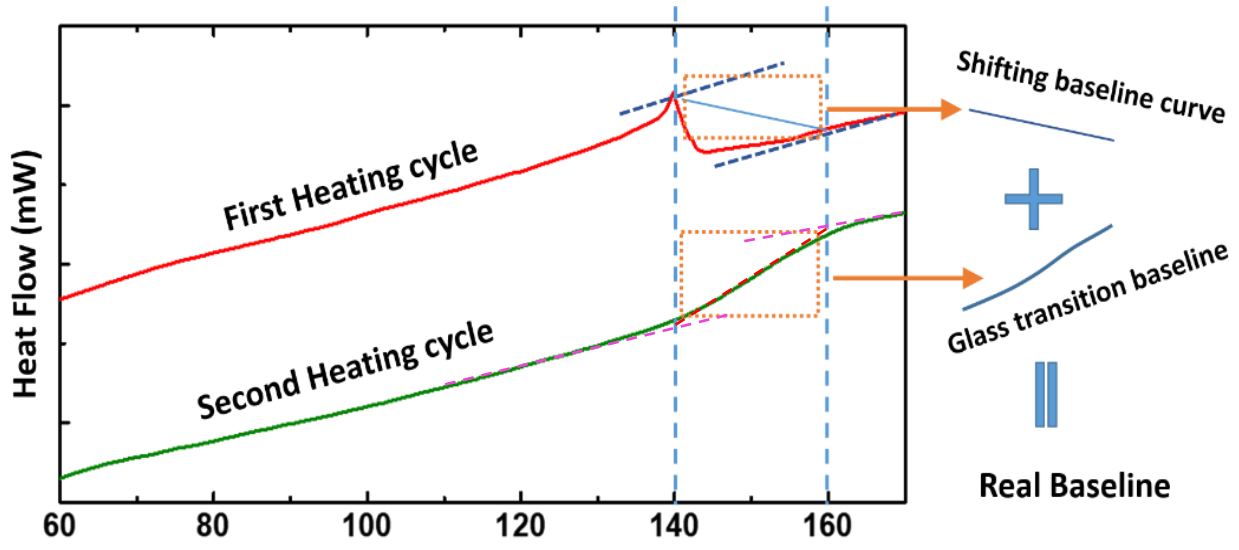

Figure 2.8. The first and the second heat flow curve during heating for the programed sample with 40% pre-strain and the baseline correction. The baseline of the heat release can be separated into two portions which are shifting baseline curve and the glass transition baseline.

Next, we discuss how the baseline for the first order transition (enthalpy), i.e., the first heating cycle for the compression programmed specimen, was determined. We considered the natural physical process occurred during the first heating cycle of the programed sample. We assumed

that the inverse peak shown in the first heating cycle in Figure 2.8 was a result of two competing physical processes. The first process was the normal glass transition, which absorbed heat, and the second process was the enthalpic energy release, which gave off heat. We also assumed that the evolution of the heat flow due to the glass transition alone was almost the same between the first and second heating cycles (Normally, there is a little difference between the first and second heating cycles due to the processing history.). We further assumed that the actual baseline of the first heating cycle for the programmed sample was separated into two parts. The first part was the glass transition and the trend of the baseline was the same as the second heating cycle "glass transition baseline" shown in Figure 2.8. The heat flow due to the enthalpy energy release can cause the "glass transition baseline" shift to lower value. This "shifting baseline curve" shown in the Figure 2-8 was used as the correction for the "glass transition baseline". In this study, we assumed that the "shifting baseline curve" was a straight line connecting the two end points in the glass transition region. The combination of the "shifting baseline curve" and the "glass transition baseline" was the real baseline for calculating the energy release. Based on this real baseline, the heat release between 140 °C and 150°C was calculated to be 2.85 J/g by integrating the heat flow curve. Based on the density of the EPON-IPD, the enthalpy release was found to be 3.25 MJ/m^3.

The dynamic mechanical analysis (DMA) profile is illustrated as the Figure 2.9. The thermal expansion behavior was also measured by the DMA under the controlled force mode. The fixture was changed to the tensile clamps. The cyclic temperature was scanned from -25°C to 180°C. The obtained data are shown in Figure 2.10. From the calculation based on the data presented in Figure 2.10, the coefficient of thermal expansion is 1.25×10^{-4} $°C^{-1}$ for the EPON-IPD network.

For tension programmed specimens, the recovery stress evolution with time was determined following the same procedure as compression programmed specimens; as shown in Figure 2.11.

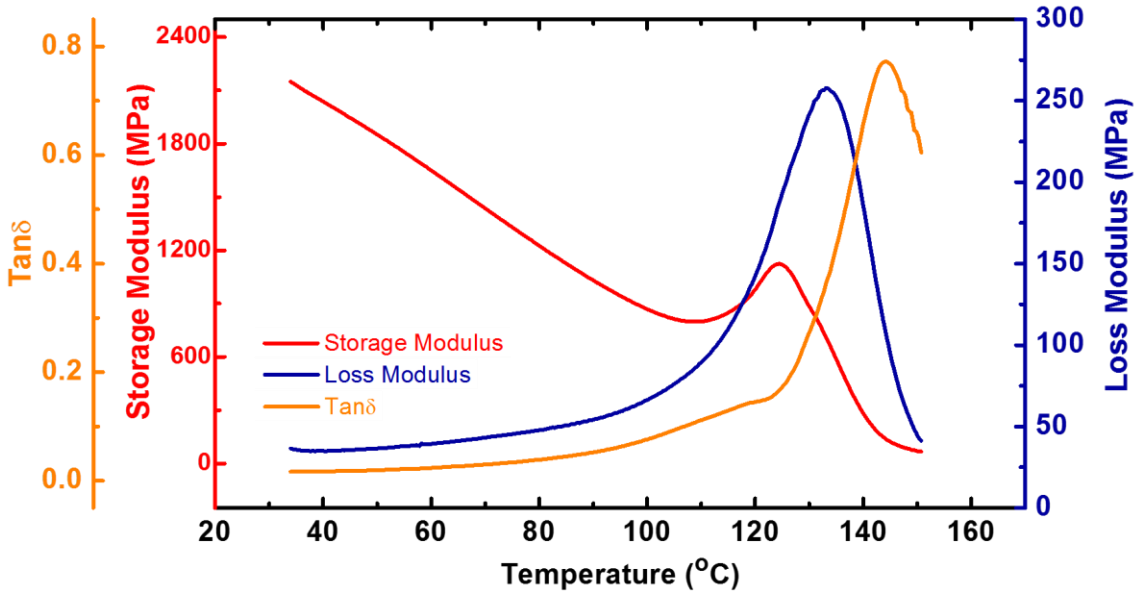

Figure 2.9. The dynamic mechanical analysis profile for storage modulus, loss modulus and tan δ against the temperature scanned from room temperature to 150°C. Based on the peak of tan δ, the glass transition temperature is between 140°C and 150°C, which is slightly lower than the result from DSC. Discrepancy between DSC and DMA measurements has been common. Instead of several MPa for most entropy driven thermoset SMPs at temperature approaching the end of the glass transition region, which is a requirement for good shape recovery, the storage modulus of our polymer network is about 65 MPa at 150°C.

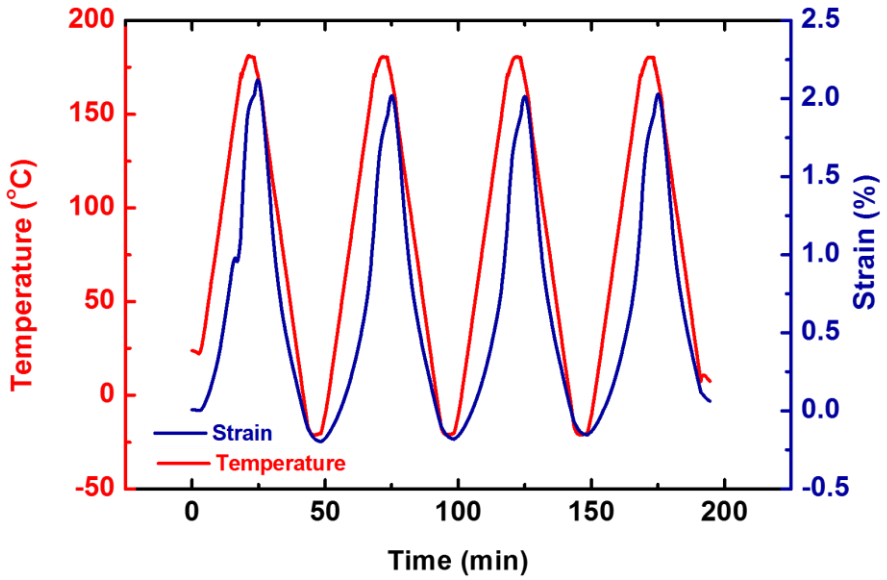

Figure 2.10. The thermal expansion test performed by DMA. The average coefficient of thermal expansion, which is equal to the strain during heating dividend by the corresponding temperature increment, is found to be 1.25×10^{-4} °C^{-1} for the EPON-IPD polymer network. The serval rounds of heating and cooling cycles lead to almost the same test results.

From Figure 2.11, one can see that the specimen with 10% tensile pre-strain can produce 5.1 MPa stable recovery stress in the rubbery state. As shown in the later study, the tensile programming stress with 10% strain is about 7.0 MPa. We would say that with 7.0 MPa stress input, 5.1 MPa stress output (recovery stress) is reasonably high. However, because the tensile fracture strain of the polymer at 170 °C is about 12%, we did not do tensile programming higher than 10%.

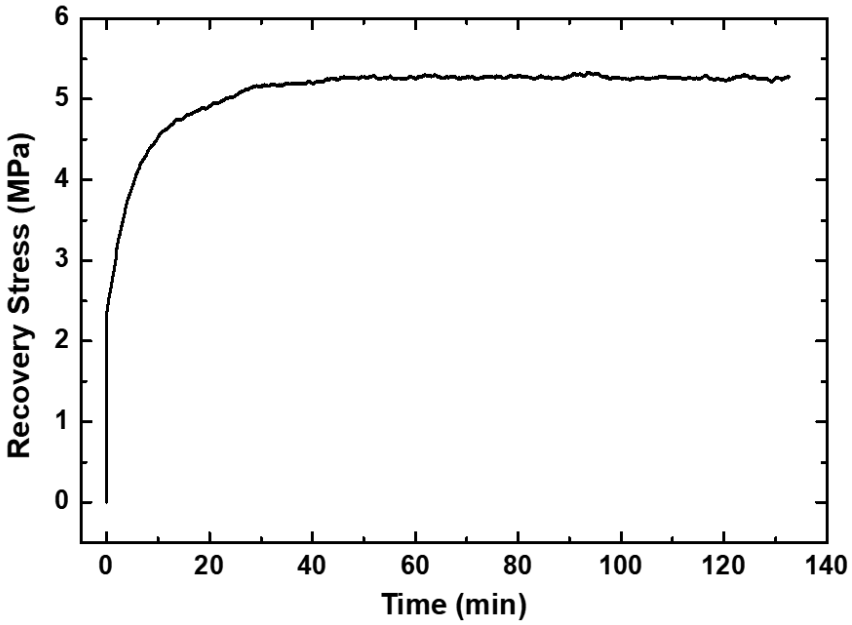

Figure 2.11. The development of recovery stress with time for the EPON-IPD specimen after 10% tensile programming.

From Figure 2.12, the peak recovery stress is about 15MPa and the stable recovery stress is about 14 MPa. Both the peak value and the stable value are lower than 17MPa, which is the stable recovery stress produced by the specimen programed in the rubbery state. This is an unusual phenomenon for shape memory polymers (SMPs). For entropy driven SMPs, the recovery stress is usually higher when the programming temperature lowers, i.e., glassy state programming has higher recovery stress than programming at glass transition zone, and the least is programming in the rubbery state. This can be understood due to the temperature memory effect, i.e., the recovery

temperature is lower if the programming temperature is lower. At lower recovery temperature, the stiffness of the SMPs is higher, leading to higher fully constrained recovery stress.

For the enthalpy driven shape memory EPON-IPON network, it stores energy primarily through the enthalpy increase due to the change in bond length. Therefore, how much enthalpy is stored or how many bonds are stretched during programming determine the recovery stress produced in the rubbery state. As discussed in the manuscript, the bonds can be changed only when they are rotated to a very high energy level. Therefore, if some regions (segments) are not soft enough to rotate, most bonds located in the segments are not stretchable. This means that the ability for enthalpy storage is not fully taking effect. At higher temperatures, bond rotation is more likely, and thus enthalpy can be increased through bond stretch. In conclusion, for this enthalpy driven SMP, programming in rubbery state leads to higher recovery stress than that in glass transition zone, which can be further validated by Figure 2.13.

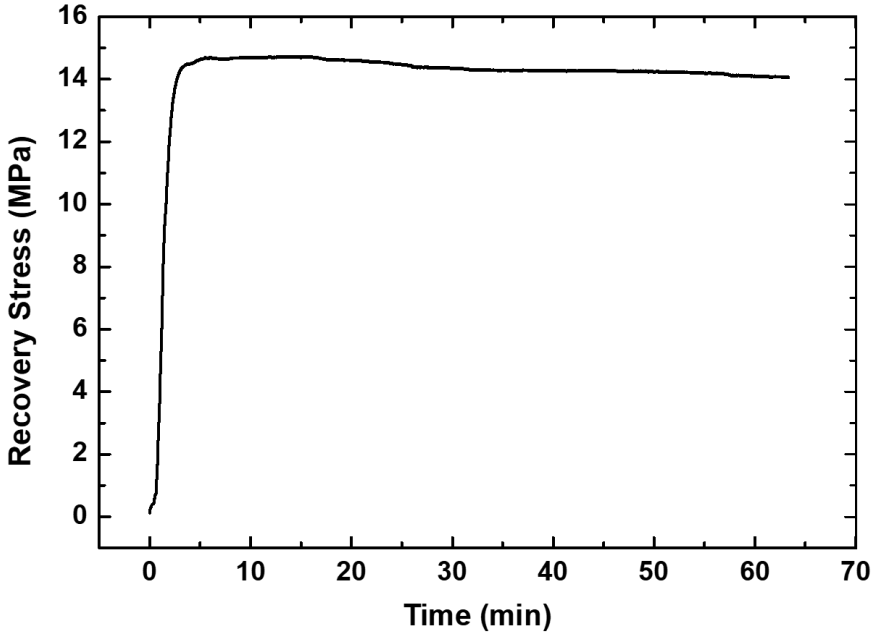

Figure 2.12. The recovery stress development with time at 170 °C (in rubbery state) for the specimen programed at 150°C (within glass transition region).

From Figure 2.13, it is clear that higher programming temperature can produce higher recovery stress. This is a proof of the argument that, for this enthalpy driven SMP, higher programming temperature leads to higher recovery stress. It is interesting to note that, for this SMP, temperature memory effect still exists. The specimen programmed at lower temperature recovers at slightly lower temperature. As mentioned previously, for entropy driven SMPs, this may lead to higher recovery stress for specimens programmed at lower temperature. For this enthalpy driven SMP, although this effect still exists, programming at lower temperature still leads to lower recovery stress. This is an evidence of enthalpy dominance in this SMP system.

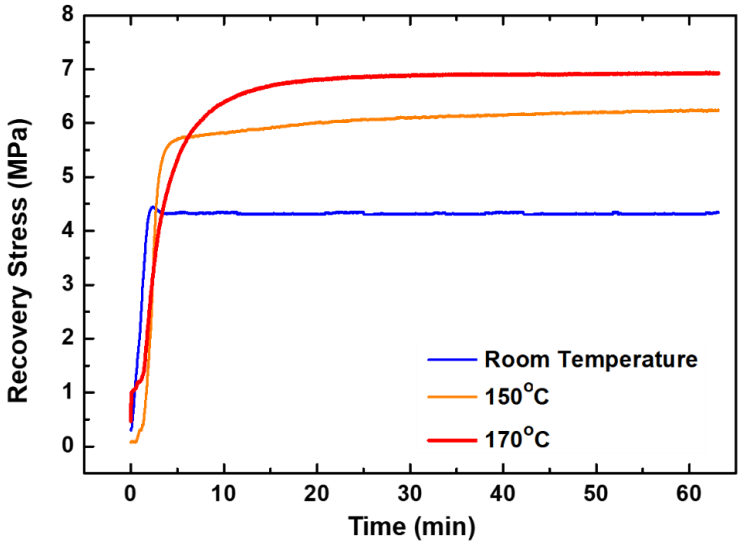

Figure 2.13. The recovery stress of the programed specimens with a fixed strain of 32% programmed at different temperatures. The recovery process was performed at the same temperature in rubbery state which is 170 °C.

We have conducted the stepwise stress relaxation test with three strain rates: 0.1mm/mm/min, 0.25mm/mm/min, and 0.5mm/mm/min; see Figure 2.14A, B, and C. As expected, the stress increases as the strain rate increases; and the relaxed stress, or stored stress, Figure 2.14D, also increases. This is understandable because higher strain rate means shorter time for stress to relax. It is noted that, regardless of the strain rate, the three zones exist; see Figure 2.14D. This suggests

that the stress is stored by both entropy and enthalpy. However, we do see that higher strain rates lead to higher residual stress or stored stress, suggesting higher recovery stress and energy output.

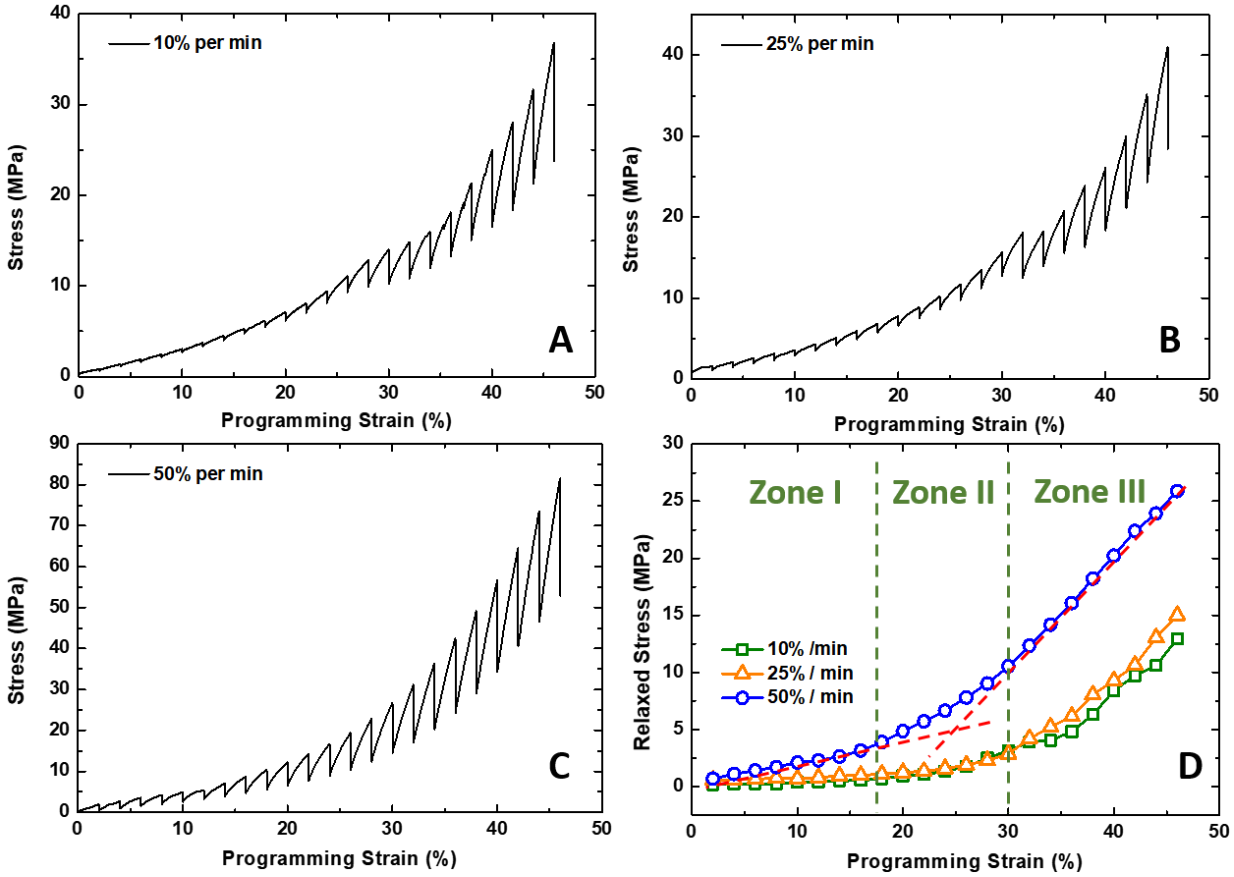

Figure 2.14. The relationship between the stress and strain for stepwise programming and the corresponding relaxed stress by different deformation strain rates. (A) The strain rate is 10% per minute. (B) The strain rate is 25% per minute. (C) The strain rate is 50% per minute. (D) The relaxed stress or stored stress for each step of the three different stepwise programming.

The relaxation and cold compression profile are showed as the Figure 2.15 and Figure 2.16.

For the tensile behavior, as Figure 2.17, at rubbery state. one can see that the polymer can only be stretched by about 12% strain before it fractures at 170°C. The peak stress or tensile strength of the SMP is about 7.1 MPa. Therefore, when we tested the tensile recovery stress of the SMP, we selected 10% strain as the tensile programming pre-strain at 170°C to make sure the pre-strain is in the safe range at the same time with enlarge the recovery stress as much as possible.

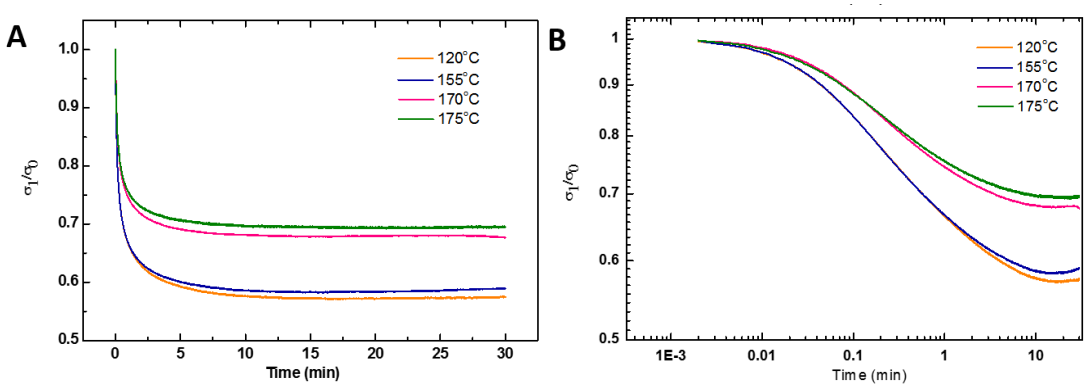

Figure 2.15. The stress relaxation profile (normalized stress with time) for EPON-IPD polymer network under different temperatures. (A) Linear scale and (B) logarithmic scale. Stress relaxation is much larger at glassy state (120°C) and glass transition zone (155°C) than at rubbery state (170°C and 175°C).

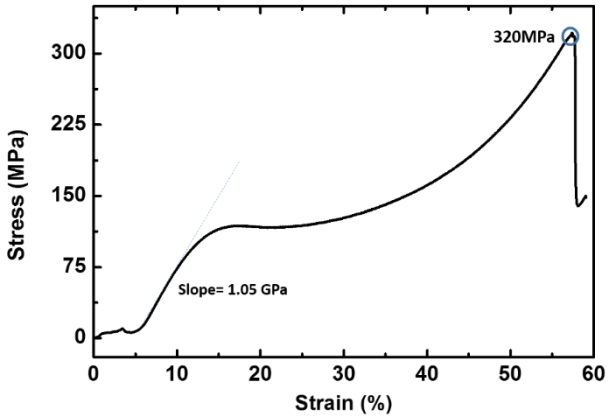

Figure 2.16. The compression stress-strain curve for the EPON-IPD polymer network at room temperature (glassy state**)**. The network shows a typical linear elasticity, yielding, strain softening, plastic flow, strain hardening, and fracture at 320MPa.

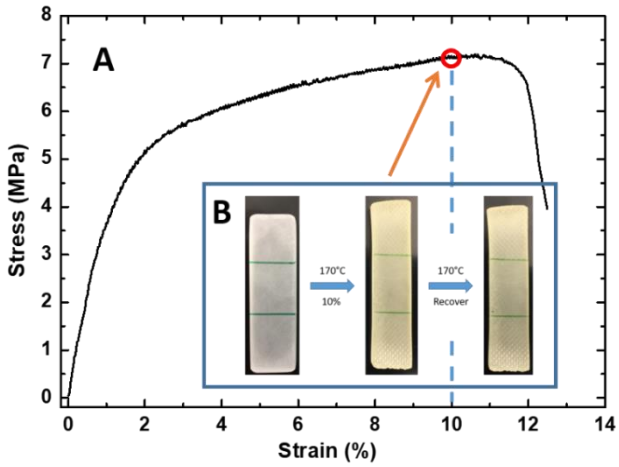

Figure 2.17. (A) The relationship between stress and strain during the tensile test for a rectangular EPON-IPD specimen at 170 ˚C. (B) The images of a specimen before and after the tensile programming and the specimen after recovery with 10% programming strain.

The bond length change during the programming is confirmed qualitatively by the Raman spectroscopy as the Figure 2.18 and the near edge X-ray absorption fine structure spectroscopy as the Figure 2.19. The quantitively analysis is discussed in the next chapter.

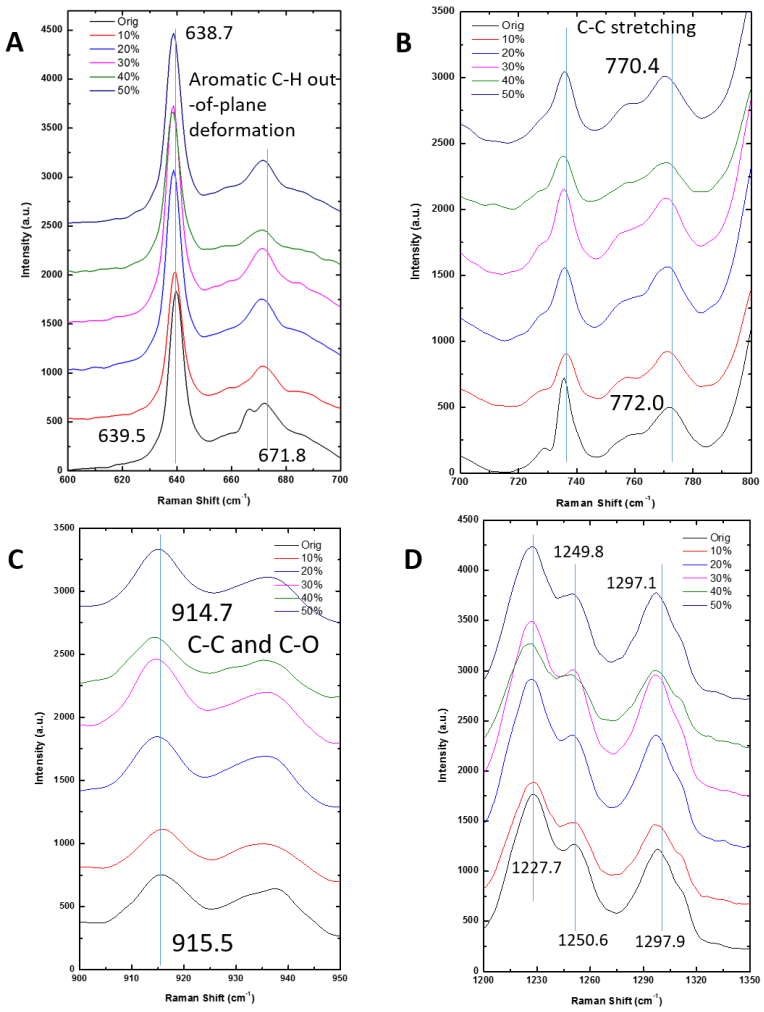

Figure 2.18. The bond length change confirmed by Raman spectroscopy. (A) Peaks for aromatic C-H out-of-plane deformation. (B) Peaks for C-C stretching. (C) Peaks for C-C or C-O stretching. (D) C-O stretching and phenolic C_4-O_2 stretching (1227.7 cm^{-1}); C-O-C stretching of the epoxy group (1250.6 to 1249.8 cm^{-1}); and C-O stretching (ether groups) and C-C stretching (1297.9 to 1297.1 cm^{-1}). From this Raman Spectroscopy, no shift happens for the programmed sample with 10% pre-strain such as Figure 2.18C, where the pre-strain locates in the LZ1 in Figure 2-6C. Therefore, bond rotation or dihedral angle change is the only mechanism for the deformation. The peaks begin to shift towards lower frequency direction for the sample with 20% programming strain, which falls on the TZ in Figure 2.6C, meaning that the bond length begins to be stretched. Therefore, bond enthalpy starts to increase. Larger shift occurs for samples programmed by 30%, 40%, and 45% pre-strains, indicating that the bond length is stretched more and more in LZ2 Figure 2.6C.

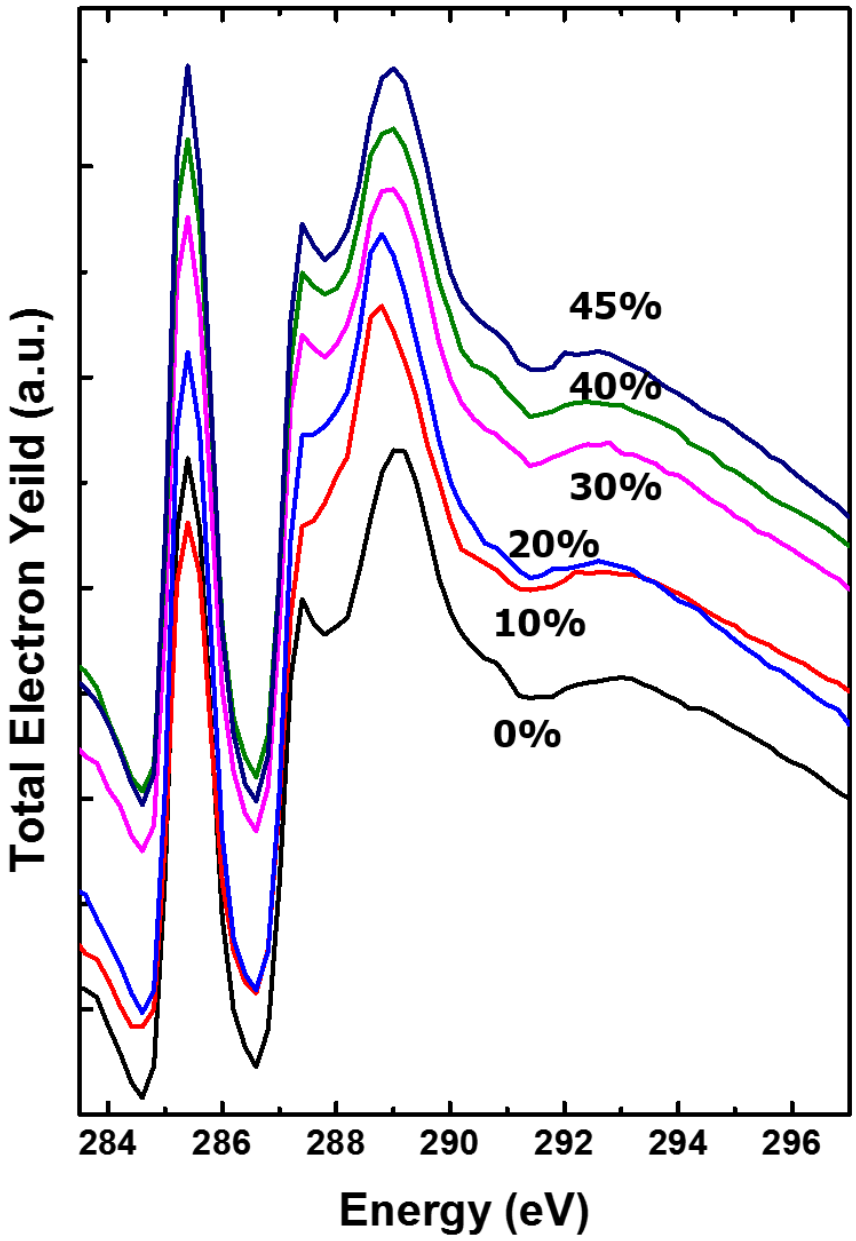

Figure 2.19. The change of bond length confirmed by Near Edge X-ray Absorption Fine Structure Spectroscopy. The first peak located at the 285.4 eV is identified as the C 1s→ C=C* (ring) resonance, which is calibrated by polystyrene. The second and the third peaks located at 287.4 eV and 289.0 eV are peaks associated with the C-H bond in the ring. The area used in the study is the wide peak located in the energy higher than 291eV. The carbon associated single bonds are the resonance for peaks such as C-C, C-O or C-N bond. It is seen that there is no shift between the 10% programmed sample and the control sample without programming. Therefore, the bond length of the carbon associated single bond does not change. With the increase in programming pre-strain, the peaks begin to shift towards lower energy direction, which proves that the bonds are stretched. Larger programming strain leads to larger shift in peaks, suggesting higher bond stretch, which is similar to the result by Raman Spectroscopy.

For the investigation of the steric hindrance, the thermal property of the synthesized EPON-BACH network is tested by DSC and the result is shown in Figure 2.20. The range of the glass transition is between 140°C and 150°C, which is a comparatively high glass transition range. This means that the EPON-BACH network is also a rigid thermoset polymer. With the same method as that used for the EPON-IPD network, the new thermoset polymer is compression programmed into 45% pre-strain as illustrated in Figure 2.21A. The recovery stress is also investigated, and the result is shown in Figure 2.21B. The only difference here is the temperature for the programming and recovery which is 160°C, other than 170°C for the EPON-IPD network. The 160°C is 10 °C higher than the end-set point for the glass transition region for the EPON-BACH, which ensures that the programming and the recovery occur at the rubbery state for this new thermoset polymer.

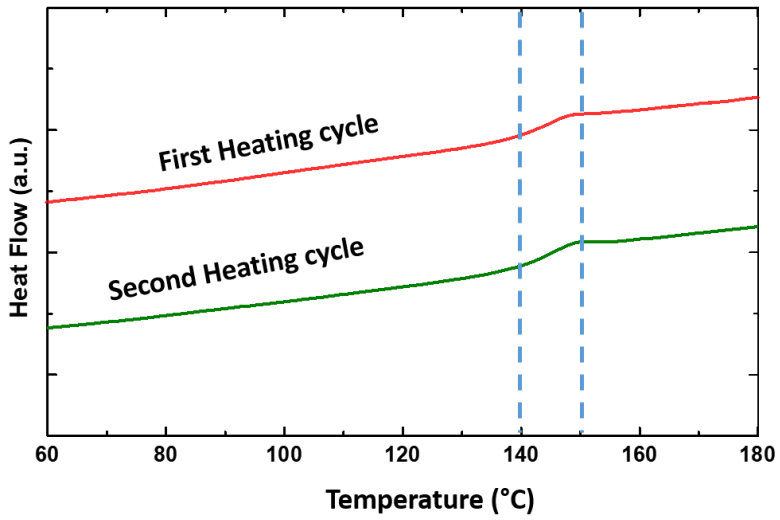

Figure 2.20. The DSC data for the un-programmed EPON-BACH thermoset network including the first and the second heating cycle.

From Figure 2.21A, one can see that the maximum compressive stress (about 38 MPa) corresponding to the 45% pre-strain is lower than the EPON-IPD network, which is about 60 MPa, suggesting that the EPON-IPD network is stiffer. From Figure 2.21B, the recovery stress for the EPON-BACH is only about 8.5MPa which is much lower than the EPON-IPD network (17 MPa).

This is a clear evidence that, the polymer network without the methyl groups cannot provide the steric hindrance and thus the recovery stress is much lower.

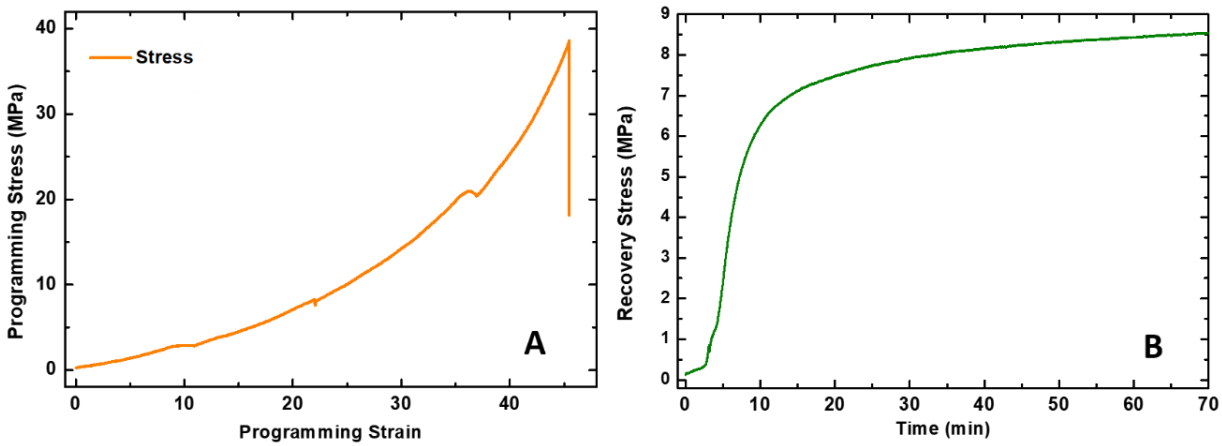

Figure 2.21. (A) The programming stress with strain and (B) the recovery stress evolution with time for the EPON-BACH thermoset polymer.

To verify the mechanism for the energy storage, the programmed EPON-BACH sample with the 45% pre-strain is characterized by DSC and the result is shown in Figure 2.22. Different from the EPON-IPD network, no inverse peak appears during the first heating cycle. It is proved that there is no enthalpy release during the free shape recovery process. Combining with the result of the recovery stress, it is concluded that the very similar thermoset network EPON-BACH, without the methyl groups attached on the cyclohexane structure in the diamine, cannot store energy in the form of enthalpy during the programming and the recovery stress is much lower than the EPON-IPD network, which consists of the methyl groups to provide the steric hindrance. Therefore, the argument on “steric hindrance” due to the methyl groups is valid.

2.4. Conclusion

Low output in stress and energy in rubbery state has been a bottleneck for wide-spread applications of thermoset shape memory polymers (SMPs). Traditionally, stress or energy storage in thermoset network is through entropy reduction by mechanical deformation or programming.

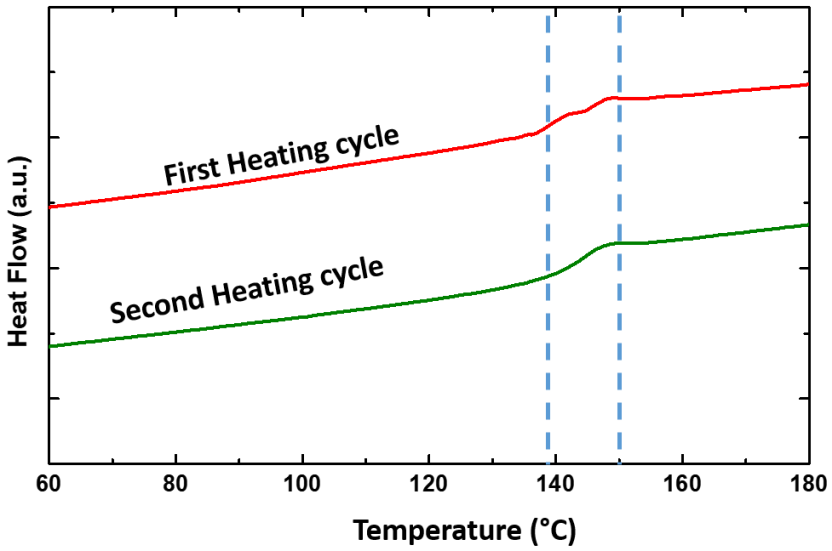

Figure 2.22. The DSC data for the 45% programmed EPON-BACH thermoset network including the first and the second heating cycles.

We here report a new mechanism for energy storage, which stores energy primarily through enthalpy increase by stretched bonds during programming. As compared to entropy driven counterparts, which usually have a stable recovery stress from tenths to several MPa and energy output of several tenths MJ/m^3, our rubbery network achieved a recovery stress of 17.0 MPa and energy output of 2.12 MJ/m^3 in bulk form. The giant stress and energy release in the rubbery state will enhance applications of thermoset SMPs in engineering structures and devices.

CHAPTER 3. THE THEORETICAL UNDERSTANDING OF THE HIGH ENTHALPY STORAGE THERMOSET NETWORK WITH GIANT STRESS AND ENERGY OUTPUT IN RUBBERY STATE

3.1. The Molecular Level Understanding

Figure 3.1 illustrates the relationship between deformation (energy input) and relaxation (energy storage) in different zones. Counter-intuitively, the compressive deformation does not shorten the bond length; instead, the bonds are stretched as shown in the schematic in Figure 3.1B. In LZ1 in Figure 2.6D, the deformation and relaxation are only related to the bond rotation as shown in Figure 3.1A. With the increase in deformation, the total energy is excited to an energy level between the bond rotation energy and bond stretch energy. Because structural relaxation accompanies deformation, the total energy, after structural relaxation, assumes its stable energy state similar to the rotational energy state, and thus the bond length returns to its original length. With further increase in deformation, the total energy will gradually assume a higher energy state, away from the rotation energy state, but towards the bond stretch energy state, which leads to the TZ in Figure 2.6D. With even further increase in compression deformation, the stabilized total energy is more towards the bond stretch energy, which is LZ2 in Figure 2.6D. As a result of the enthalpy increase, around 43.8 MPa of internal stress can be stored by the stretched bonds; see calculation in section 3.3.

During the compressive deformation, the polymer network is in a non-equilibrium state at any instant. The stress relaxation is coupled with deformation. At each increment of deformation, the total free energy is excited to a higher level, most likely unstable. Due to the coupling of structural or stress relaxation, the excited energy level is relaxed back to a local “energy well”, to minimize the total free energy.

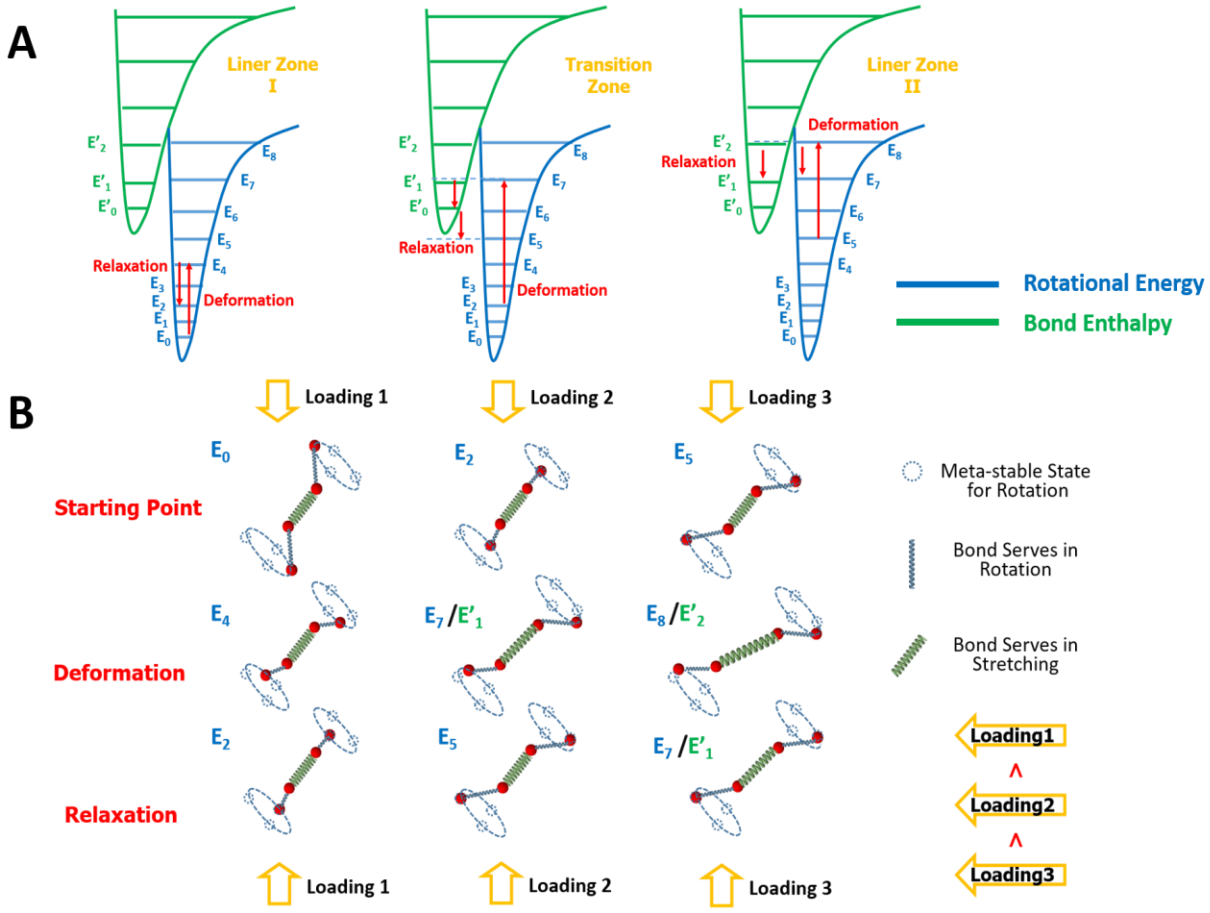

Figure 3.1. The energetical, structural and conformational characteristics during compression deformation. (A) The energetical evolution corresponding to linear zone I (LZ1), transition zone (TZ) and linear zone II (LZ2). Deformation excites the energy to a higher level, most likely an unstable energy state; and after structural or stress relaxation, retreats to a local lower energy level, leading to meta-stable state. For example, in the LZ2, deformation excites the rotation energy level from E_5 to E_8, and relaxation retreats the energy level in terms of bond enthalpy to E_1'. (B) The structural and conformational evolution corresponding to LZ1, TZ and LZ2. The blue springs stand for rotating bonds and the green springs represent stretching bonds. The dashed circles are the possible locally meta-stable positions for the rotating bonds. Under loading 1, only bond rotation happens during both deformation and relaxation. Under loading 2, which is larger than loading 1, both bond rotation and stretching can happen during the deformation. However, the stretched bonds retreat during the relaxation. Under loading 3, which is the highest loading, the stretched bond can be stabilized in a certain conformation. The simplification made here is that the rotating bonds (blue springs) are fixed length during the deformation and the relaxation. The reality is that the rotating bonds can also be stretched.

3.2. Enthalpy Energy Storage and Recovery Stress

3.2.1. Enthalpy Storage

The chemically cross-linked network in the rubbery state can be treated as a supramolecule. When the deformed subject is treated as an elastic body in rubbery state, the energy stored is described by the Mooney's equation [32-34]:

$$W = C_1\left(\alpha_x^2 + \alpha_y^2 + \alpha_z^2 - 3\right) + C_2\left(\frac{1}{\alpha_x^2} + \frac{1}{\alpha_y^2} + \frac{1}{\alpha_y^2} - 3\right) \qquad (S_1)$$

where C_1 and C_2 are constants, α_x , α_y and α_z are stretches in three-dimensional coordinate. For example, $\alpha_x = L_x/L_{x0}$ where L_x is the length after deformation in x direction and L_{x0} is the original length along the x axis. If the volume is assumed to be a constant, $\alpha_x\alpha_y\alpha_z = 1$. As a simplified case, let $\alpha_x = \alpha$, $\alpha_y = \alpha_z = 1/\alpha^{1/2}$, the retractive stress τ , given by $\frac{dW}{d\alpha}$, is:

$$\tau = 2C_1\left(\alpha - \frac{1}{\alpha^2}\right) + 2C_2\left(1 - \frac{1}{\alpha^3}\right) \qquad (S_2)$$

If α is the stretch ratio in uniaxial test by a mechanical testing machine, the retractive stress can be used as the prediction of the deformation stress applied by loading. When α is greater than 1, the sample is under tensile test. On the other hand, if the sample is compressed, the value of α is less than one. In this case, the value of τ is negative, which represents that the retractive stress turns to tension.

The first term in the right-hand side of equation S_2 is actually related to the change of conformational entropy. The change of the conformational entropy per volume (ΔS) is described by the following equation:

$$\Delta S = -\frac{\rho R}{2M_j}\left[\alpha^2 + \frac{2}{\alpha} - 3\right] \qquad (S_3)$$

where ρ is density, R is the gas constant, and M_j is the molecular weight between closest crosslinking points or chain entanglements. The associated retractive or expansive stress (σ_s) is derived by $-d(T\Delta S)/d\alpha$ as the following equation:

$$\sigma_S = \frac{\rho RT}{M_j}\left[\alpha - \frac{1}{\alpha^2}\right] \qquad (S_4)$$

Obviously, if let $2C_1 = \rho RT/M_j$, equation S_4 becomes the first term on the right-hand side of equation S_2; in other words, the first term on the right-hand side of equation S_2 is indeed generated by entropy change.

Although the equation S_2 can be used for many cases of polymer deformation in rubbery state, especially for rubbers, the second term on the right-hand side needs more understanding. The physical meaning of the constant C_2 in the second term of equation S_2 is not fully understood. For most rubbers, the second term functions as a correction term because the result of the first term is not far away from the test result. However, for the EPON-IPD network, if only the entropy term is used for the calculation of the retractive stress, i.e., using equation S_4 alone, the retractive stress is calculated to be $\sigma_s = 20.5\,MPa$ when the following parameters are used: $\rho = 1.143 \times 10^{-3} g.mm^{-3}$, $R = 8.314\,J.mol^{-1}.K^{-1}$, $T = 170\,℃ = 443K$, $M_j = 446.29\,g.mol^{-1}$ and $\alpha = 0.6$. This retractive stress value is much lower than the corresponding programming stress as shown in Figure 2-6C, which is about 60 MPa. Therefore, entropy alone cannot capture the energy stored in the network. It is noted that, since the functionality of EPON is two and the functionality of IPD is four, it means that each EPON molecule is shared by two IPD molecules, but each IPD molecule is shared by four EPON molecules. Therefore, the weight of the repeating unit should be defined as one EPON molecule and half IPD molecule. This repeating unit can also serve as the chain between the cross-linking points and the molecular weight is 446.29 g/mole.

Therefore, for programming strain up to 40%, mechanism other than entropy must be considered. From the next section, we will find that the stress needed to stretch the bond is about 43.8 MPa. If we combine the entropy stress 20.5 MPa and the enthalpy stress 43.8 MPa, we obtain a total stress that needed to deform the sample is 64.3 MPa, which is very close to the programming stress of about 60 MPa. Therefore, for larger programming strain, enthalpy increase is indeed a way of storing energy. From the equation S_2, the second term on the right-hand side is possibly dominant more than the first term because the value of α is less than 1 in compression programming. The $1/\alpha^3$ term is greater than $1/\alpha^2$. Therefore, the second term is likely related to enthalpy increase, or bond stretch.

From the analysis in the main body of the paper, the energy storage is still entropy dominant when the programming strain is less than 20%, which can be confirmed by equation S_4. The calculated entropic stress is 2.5 MPa and 5.7 MPa for the 10% and 20% programmed sample. They are comparable with the programming stress in Figure 2.6C, which are 4.1 MPa and 9.0 MPa, respectively. The sample with 10% programming strain only needs a slight correction by the second term of equation S_2. The sample with 20% programing strain needs a little more correction by the second term in equation S_2 because the bond length stretching enthalpy has already begun to take effect in the transition zone.

3.2.2. Recovery Stress

The energy storage mechanisms in the shape memory network can be further explained by the recovery stress. Let's first assume that the energy is stored by entropy only. The recovery stress at the maximum programming strain can be estimated by the following empirical equation for the change of entropy [35]:

$$\Delta S_S = 5.2819\ (\varepsilon_{max})(\sigma_R) \qquad (S_5)$$

and

$$\Delta S_s = 1.4011 \frac{(tan\delta_{max}^2)(v_j)^{0.6613}}{\ln(v_j)} \qquad (S_6)$$

where ΔS_S is the stored entropy, ε_{max} is the maximum programming strain and the σ_R is the associated recovery stress, $tan\delta$ is the ratio of loss modulus to storage modulus, and v_j is the cross-link density which equals to ρ/M_j as defined in equation S_3 or S_4. The constants in equations S5 and S6 were obtained by curve fitting. Plugging in equation S_5 to equation S_6, the empirical equation for σ_R can be derived as follow:

$$\sigma_R = \frac{1.4011(tan\delta_{max}^2)(v_j)^{0.6613}}{5.2819(\varepsilon_{max}) \times \ln(v_j)} \qquad (S_7)$$

By using the same parameters applied to section 3.2.1 and the value of $tan\delta$ being 0.77 (from the data in Figure 2.9), σ_R is calculated for the 45% programed sample, which is equal to 7.0 MPa. This value is much lower than the measured recovery stress shown in Figure 2.6A and B in the main text. Therefore, entropy reduction alone fails to predict the test result. Enthalpy increase can explain the difference between the measured recovery stress (about 17 MPa) and the entropic recovery stress (7 MPa).

3.3. Stress Needed to Change the Bond Length

From section 3.2, energy storage mechanism other than entropy reduction must be considered to explain the difference between test results and model predictions. The vibrational energy associated with the chemical bond is an effective indicator for the change of the bond length such as carbon-carbon single bond. Raman spectroscopy, as the characterization technique analyzing the vibrational energy corresponding to the chemical bonds, is a powerful tool to determine the change of the bond length qualitatively. The semi-quantitative approximation can also be done by

using the proportionality constant, between the change of chemical bond shift and the stress needed to cause the bond shift. The detailed theoretical explanation is as follows.

The potential energy of chemical bond during the deformation is approximated by the Morse function [36] for anharmonic oscillation:

$$U_p = D_e(1 - e^{-b(x-x_0)})^2 \qquad (S_8)$$

where U_p is the potential energy, D_e is the dissociation energy which is the energy needed to break the bond. Here b is a constant that equals to $\sqrt{k_e/2D_e}$, where k_e is the force constant at the minimum point of this function. The term $(x - x_0)$ is the change of interatomic distance.

The second derivative of equation S_8 provides the force constant of the oscillation as the following:

$$k = 2b^2 D_e(2e^{-2b(x-x_0)} - e^{-b(x-x_0)}) \qquad (S_9)$$

According to Tashiro [37], the chemical shift or frequency (ν) is proportional to $\sqrt{k}$. From equation S_9, in a small range around x_0, k decreases monotonically as shown in Figure 3.2. Therefore, when Δx is positive, $\Delta \nu$ is negative and the chemical bond is under stretching. To the opposite, when Δx is negative, the force constant increases, causing the frequency shift to higher values.

Based on Rretzlaff and Wool [38], the variation of frequency ($\Delta \nu$) is proportional to the applied stress. In our case, the change of the chemical bond shift in the Raman spectroscopy is observed without external loading, thus it is caused by the internal stress. This internal stress is also proportional to $\Delta \nu$.

The standard method to characterize the correlation between the Raman peak shift and the internal stress is the *in-situ* testing. The variation of the Raman shift should be observed during the

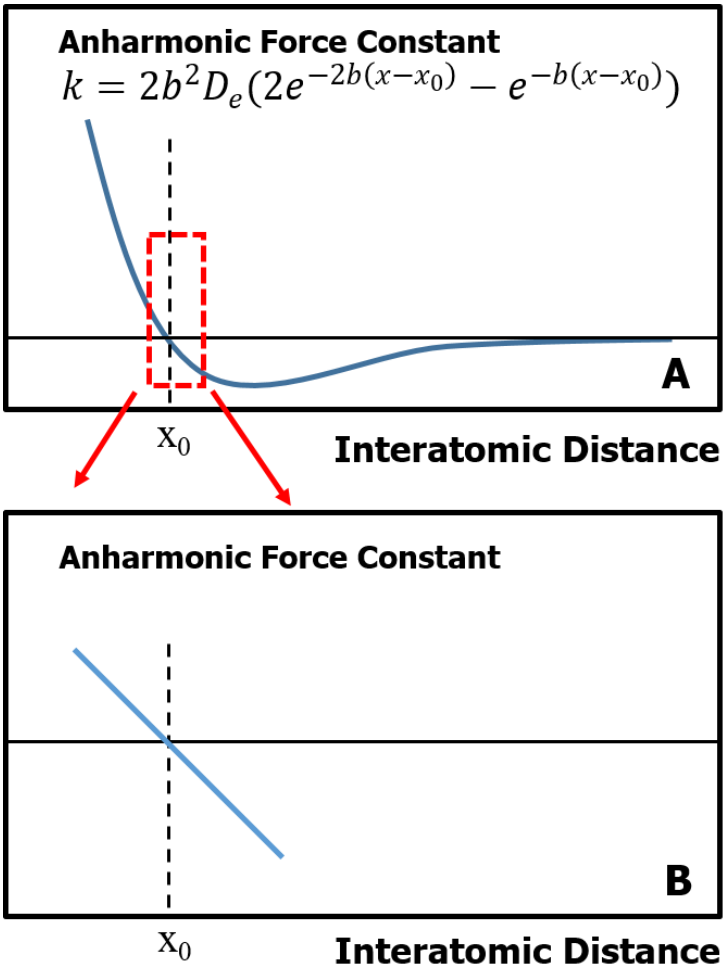

Figure 3.2. The relationship between force constant of anharmonic oscillation. (A) full range of interatomic distance and (B) the small range around x_0. In a small variation around x_0, k decreases monotonically.

deformation. The relationship between the peak shift and the external loading can be assumed as a linear fashion. During Raman test, the deformation is stepwise or very slow. Therefore, the internal stress is assumed the same as the external loading. Curve fitting may also be needed to estimate the precise coefficient. Based on this discussion, the EPON-IPD network also needs the coefficient for all the types of bonds. Without the *in-situ* Raman spectrometer associated with the mechanical deformation accessories, as a rough estimation, we turn to the equation proposed by Wei et al. [39], which links the internal stress, Raman shift, and modulus of elasticity of the materials:

$$\sigma_{bond} = \frac{E}{1-\nu} \times \frac{\Delta\omega}{\omega_0} \qquad (S_{10})$$

where σ is the residual stress, E is the Young's modulus, ν is the Poisson's ratio, Δω is the variation of the Raman shift, and ω_0 is the reference Raman peak (original peak). The Poisson's ratio for the EPON-IPD is set as 0.48, which is an acceptable value for the nearly non-compressible thermoset polymer. The variation and the reference Raman peak can be obtained by the Raman spectrum. An additional parameter is the Young's modulus of the programed sample. Because the Raman spectrum was collected from the programed samples at room temperature, the Young's modulus with the same condition should be tested and utilized. Hence, the programed EPON-IPD sample with the 45% pre-strain is deformed with a very small strain as shown in Figure 3.3. The Young's modulus of the programed sample is estimated by the slope of the initial stress-strain curve, which is 16.0 GPa. The variation of the Raman shift for different types of bond due to the stretching is calculated and summarized in the Table 3.1.

Table 3.1. The variation of the Raman shift of the different bonds due to programming to 45% strain.

Bond type	C-H	C-C	C-O (ester)	C-OH
ω_0 (cm^{-1})	639.5	772	915.5	1250.6
ω_{final} (cm^{-1})	638.7	770.4	914.7	1249.8
Δ ω (cm^{-1})	0.8	1.6	0.8	0.8

It is noted that Eq. S_{10} is based on one single type of bonds. In our SMP, it consists of several types of bonds; see Table 3.1. Because the Young's modulus in Eq. S_{10} is for the entire network, we cannot use it to obtain the internal stress for each individual bond and then sum them up. A

better way may be to use the rule-of-mixture's approach, which needs to consider the percentage of each type of bonds within the network. Therefore, Eq. S_{10} is revised to Eq. S_{11}:

$$\sigma_{interal} = \frac{E}{1-\nu} \times \left(\frac{\Delta\omega_{CH}}{\omega^o_{CH}} \times \frac{N_{CH}}{N_{total}} + \frac{\Delta\omega_{CC}}{\omega^o_{CC}} \times \frac{N_{CC}}{N_{total}} + \frac{\Delta\omega_{CO-ester}}{\omega^o_{CO-ester}} \times \frac{N_{CO-ester}}{N_{total}} + \frac{\Delta\omega_{CO-Epoxy}}{\omega^o_{CO-Epoxy}} \times \frac{N_{CO-Epoxy}}{N_{total}}\right) \quad (S_{11})$$

where $\sigma_{internal}$ is the stored internal stress due to programming. *N* stands for the number of bonds and the subscript of *N* means the type of bond in a representative molecular unit (repeating unit). The subscript "total" is the sum of the number of bonds for all types of bonds within the repeating unit, i.e., $N_{total} = N_{CH} + N_{CC} + N_{CO-ester} + N_{CO-Epoxy}$.

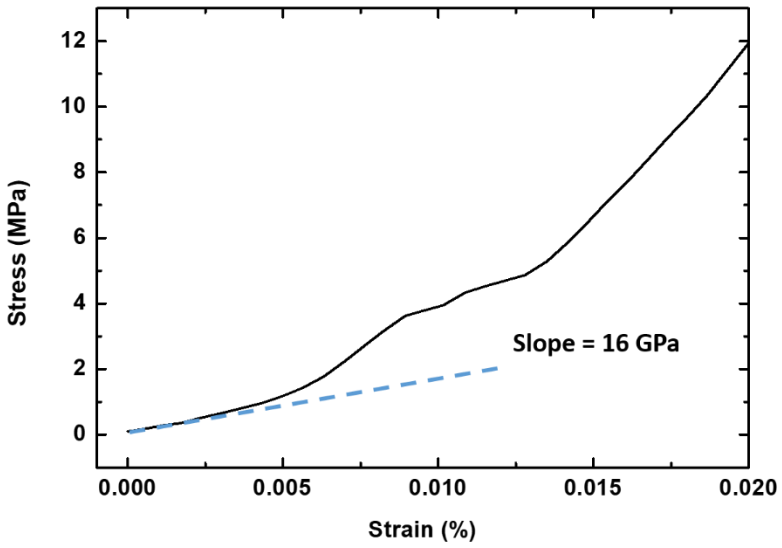

Figure 3.3. The stress-strain curve for the programed sample with 45% pre-strain. The sample was deformed within a very small strain.

Next, let us count the numbers for each type of bonds in the repeating structure. This percentage is the same for the whole network when we neglect the defects and end groups. For simplification, we also neglect the repeating unit in EPON 826 because only very low portion of the EPON has the repeating unit (8.5%). We count the number of bonds per Figure 3.4, which

includes Aromatic C-H: 8; ester C-O: 4; C-OH: 2; and -C-C-: 6 + (4/2) = 8. All counts are straightforward except for the number of carbon-carbon single bond. Firstly, there are 6 such bonds in EPON structure which are excluding the carbon connecting the benzene ring. There are four in the IPD which are excluding the carbon belonging to cyclic hexane. Because only half of the IPD needs to be counted, the four bonds are divided by two. Consequently, the total number of carbon-carbon single bonds are eight.

Plugging in all the parameters in Eq. S_{11}, we find that $\sigma_{internal}$ = 43.8 MPa. Combining the entropic stress of 20.5 MPa, the total internal stress due to programming is 64.3 MPa, which is close to the programming stress of 60 MPa. It has been known from polymer physics that both entropy and enthalpy, along with other factors, contribute to energy storage [40]. Again, this very rough estimation confirms that, for this new thermoset SMP, both entropy and enthalpy contribute to energy storage; however, with higher programming strain, enthalpy storage predominates.

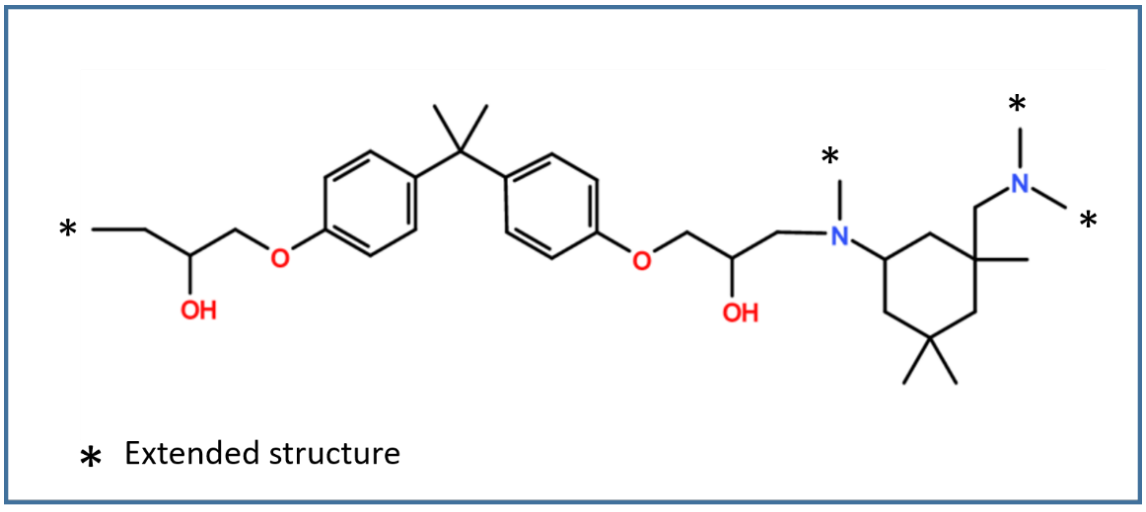

Figure 3.4. The structure of a repeating unit of the EPON-IPD network.

3.4. Multiple Energy Well Model

3.4.1. The Shape Memory Effect Understood Through Multiple Energy Well Model

Figure 3.5A visualizes these natural characteristics hidden in the programming process. Each instantaneous non-equilibrium state is regarded as a locally high energy state and each instantaneous equilibrium state is regarded as a locally low energy state, the so called meta-stable state. This can be demonstrated by an analogy of a ball resting on an energy hill with many "energy wells or dips". The physical meaning for the movement of the ball can be understood as a change of the conformation or structure. Hence, the ball is named as a conformational or/and structural ball (CSB). Each apex of the well corresponds to a local high energy state (non-equilibrium); each valley of the well corresponds to a local low energy state (equilibrium). At each instant of deformation, the ball is excited to the apex, leading to non-equilibrium; after structural relaxation, the ball retreats to the bottom of the nearest valley, achieving local energy minimization, so that the network is in a meta-stable state. Theoretically, the real profile of the locally high or low energy state is continuous because of the numerous conformations available in the network. Moreover, each energy well should be extremely narrow. To visualize and simplify the idea for further discussion, the "well-shaped" discontinuous energy states are illustrated in Figure 3.5A.

Figure 3.5A also shows how the energy is stored and how the shape is fixed during the programming process. Microscopically, the heat absorption enhances the motion of electrons and reduces the electron cloud density. Consequently, the deformation can be applied more easily and higher energy level can be achieved. When the temperature drops while maintaining the programming strain, the electrons localize to the associated atoms and this meta-stable conformation or structure of the network is frozen by the amplified energy well (the dotted green line in Figure 3.5A). CSBs will locate at the bottom of the new cold energy well. Because the depth

of the energy well is enlarged, the CSBs are difficult to jump out of the cold well without a sufficient energy input. Therefore, the temporary shape is fixed. When the temperature is lower than the glass transition zone, the bonds are not easily rotatable due to the lack in free space. Although the stretched bonds, which contain enthalpy, try to return the network to their original configuration after cooling and unloading, their energy is not sufficient to overcome the energy barriers formed by the surrounding neighbors. Hence, the enthalpy is stored in the stretched bonds.

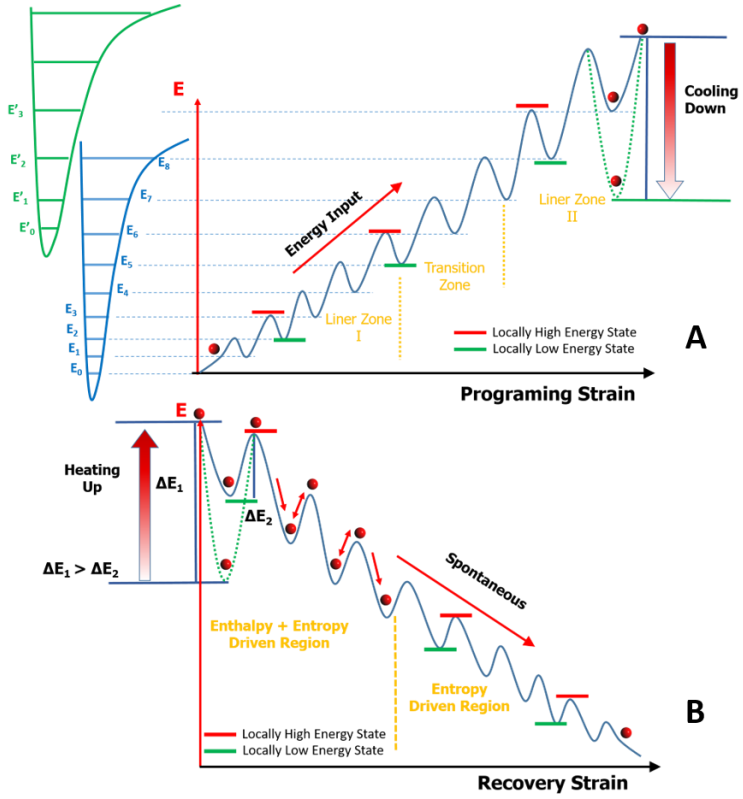

Figure 3.5 The "multiple energy well" model for amorphous thermoset shape memory polymers. (A) Programming. During programming at temperature above the glass transition zone, the network climbs up an energy hill with local energy well (or dip) (blue line) for local, meta-stale states. At the end of programming (after cooling and unloading), a deep energy well (dashed green line) is formed and thus the network is in a locked, non-equilibrium state. (B) Recovery. Energy input, such as heating, is needed to drive the cold energy well (dashed green line) back to the hot energy well (solid blue line) and help the CSBs (red circles) jump out of the final energy well, roll down the energy hill, and achieve shape recovery without external constraint, or stress recovery with external constraint.

Figure 3.5B shows the shape recovery process. For the free shape recovery, the cold energy well (the dotted green line) gradually gains energy and switches back to the hot energy well (the solid blue line) when the programmed network is reheated. Once a critical temperature is achieved, here the onset point of the glass transition zone, some bonds become rotatable. The CSBs are gradually lifted from the bottom of the well. The stretched bonds will attempt to contract and release their enthalpy by rotatable bonds into the whole continuous network. With further increase in temperature (energy input), the CSBs are lifted to the edge of this energy well by the stretched bond. If the absorbed energy of CSBs is greater than the energy barrier of the energy well and the network is not constrained externally, the CSBs can overcome the energy barrier and plunge back to the lower energy well. Eventually, CSBs will stabilize at the ground energy state. Macroscopically, the network restores the permanent shape, suggesting completion of the free shape recovery.

The stress recovery can also be discussed based on this energy well model. If the network is confined, the CSBs will stay at the edge of the last energy well (the deepest blue energy well) formed at the end of programing in Figure 3.5A and generate the recovery stress. This recovery stress can be separated into two parts: the thermal stress and the memorized stress. The thermal stress is generated by the more strenuous movement of electrons in space. This drives the green colored energy well (cold) back to the blue colored energy well (hot) in Figure 3.5B. The memorized stress can be further separated into two categories. The first category is generated by the micro Brownian motion which is related to the entropy. The second category is generated by the retreat of bond length which is enthalpy related. During the reheating, in the glassy state, the thermal stress plays a major role. Once the temperature comes to the onset point of the glass transition zone, the memorized stress starts to release. For entropy, it generates recovery stress by

micro Brownian motion; for enthalpy, the bond length shortening applies forces to rotatable bonds, and accelerates the velocity of micro Brownian motion to even higher energy level. The increased velocity, or kinetic energy, will transfer to the boundary of the specimen contacting the test machine, to produce the impact force or recovery stress, similar to gas motion in a container. In the energy well model, the stored stress highly depends on the depth of the final energy well (deepest blue well). The deeper the energy well, the more the energy can be stored and the higher the recovery stress is.

3.4.2. Detailed Explanation of the Multiple Energy Well Model

3.4.2.1. General Scheme

The concept of energy well against change of conformation is not a creation out of nothing. The potential energy changes by the rotational dihedral angle for butane and conformation for cyclohexane have been estimated for decades as the illustration shown in Figure 3.6. The butane can be treated as the smallest polyethylene which is a dimer. During the rotation of σ bond in the middle, the potential energy of the molecule fluctuates in a well-shape. When the methyl groups, which are electron rich groups in a butane, are closest to each other, the electron-repelling leads to the highest potential energy. The spatial position between chemical bonds is the electron acceptable space (we can call it electron acceptor or electron hole). When the electron rich group is stabilized in the space lacking electrons, the total potential energy of the molecule is reduced. Once electron rich groups find the most comfortable positions as shown in Figure 3.6A-a and j, the potential energy touches the ground state. On the other hand, the stable positions that can still be found are local lowest potential energy states which are called metastable states as shown in Figure 3.6A - c and e. It is obvious that the potential energy of the metastable state is higher than the ground state, and more polymer repeat units form more metastable states. For example, the

metastable state in butane is 3.8 kJ/mol higher than that of the ground state. The energy evolution by free rotation of chemical bonds was first studied by Flory [41] and Tylor in 1940s [42]. The "multiple energy well" model is based on this established knowledge. Nevertheless, some differences need to be pointed out. Firstly, the metastable position of bonds is not only affected by the intramolecular interaction like butane but is also affected by the intermolecular interaction. In other words, the circumstance of the rotatable segments in a polymer network also affects the variation of the energy states. All interactions in molecular level can be generalized by electron repelling (peak of energy well) or electron stabilization (bottom of energy well) by electron acceptable space (electron acceptor) or electron vacancy space (electron hole). During the rotation of the chemical bonds, the local metastable position can be reached. The process of searching then staying at a metastable position can be imaged as the CSBs fall into an energy well. Secondly, both tension and compression cannot rotate the torsional angle to exceed the limit, which is 180 degrees. Therefore, during the programming of the polymer network, the pattern of potential energy is not symmetry as butane. Only half of the pattern can be revealed and it is kept ramping up.

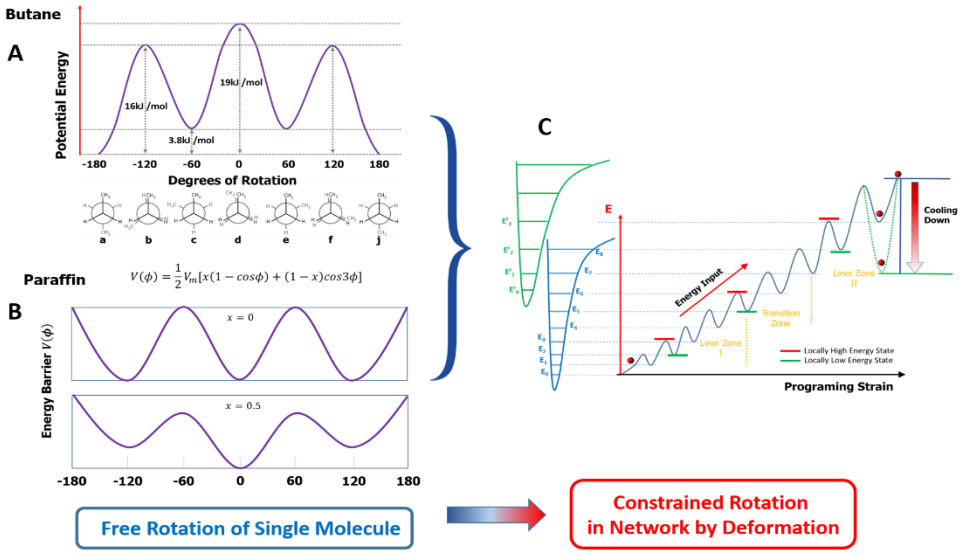

Figure 3.6 The origin of "multiple energy well" model. (A) The relationship between potential energy and rotational angle for butane. (B) Two different cases for the energy barrier curve of paraffin based on Taylor's equation. (C) "multiple energy well" model.

3.4.2.2. Free Shape Recovery versus Exothermic Chemical Reaction

The free shape recovery, as a spontaneous process associated with Gibbs free energy variation, has a lot of analogies compared with an exothermic chemical reaction as shown in Figure 3.7. The classical interpretation of a chemical reaction is described as follow. Although the free energy of reactants is higher than the product, the reaction will not occur without the activation energy. Before the spontaneous process happens, the reactants need to be excited into a high energetical level by heat, light, microwave or others. The total free energy will be stabilized by the variation of the molecular structure or degree of freedom. The Gibbs free energy of reactants is higher than the products and the free energy can be separated into enthalpy part and entropy part. The enthalpic part is due to the type of chemical bonding that is changed. In shape memory effect, although the free energy of the fixed polymer network is higher than the original shape, it will not recover spontaneously without energy input. After the excitation by heating, the spontaneous transition will happen. The total energy is stabilized by the conformational and structural variation in the network during the recovering. The total free energy of the polymer network can also be separated into the enthalpic part and entropic part. The difference between these two phenomena is that the chemical bonds, regardless of reactants or products, exist naturally. The conformation or structure of the polymer network located at high energy state needs programming.

3.4.2.3. Recovery Rate

The recovery rate of SMPs during free shape recovery is a significant property for all shape memory polymers. In this “multiple energy well” model, it corresponds to the time for the CSBs to roll down to the ground state. The free recovery process can be divided into two regions. The driving force for the high-energy region is the combination of entropy and enthalpy. In this region, the CSBs will be pulled back to low energy well by the stretched bonds. Subsequently, the CSBs

located at the peak of an energy well is not in an equilibrium state. In this case, the driving force from the stretched bonds is the dominant factor for controlling shape recovering rate. In the low-energy region, the driving force that helps the CSBs fall back into low energy well is entropy only. If the chance of falling into an old or new energy well is equal, the frequency of CSBs vibrating in one energy well will determine the recovery rate. These characteristics is affected by the intrinsic property of the network, the environment of rotatable bond, and the temperature.

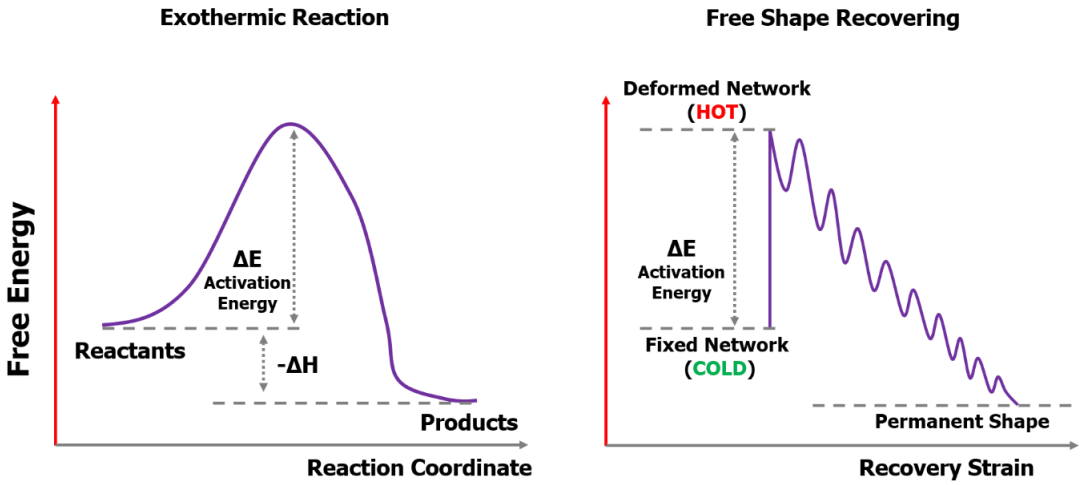

Figure 3.7. The comparison of the exothermic reaction and free shape recovery. Both of them share the same mechanisms: while the internal energy is high in the non-equilibrium state, the systems need external energy input to overcome the energy barrier and trigger either the exothermic reaction or shape recovery.

3.4.2.4. Recovery Ratio

Although the "multiple energy well" model assumes that the polymer network contains no defect and no permanent deformation happens during the programming process, this model is capable of explaining the shape memory effect (SME) with plastic deformation by slight modification as shown in Figure 3.8. Even for a perfect polymer network, permanent deformation can happen such as breaking chemical bonds due to "over-programming". It happens much more easily for physically crosslinked SMPs because the network is constructed by chain entanglements or intermolecular interaction. The shape is hardly recovered when permanent deformation occurs.

In this case, the term named shape recovery ratio is employed to define the recovered shape or strain quantitatively.

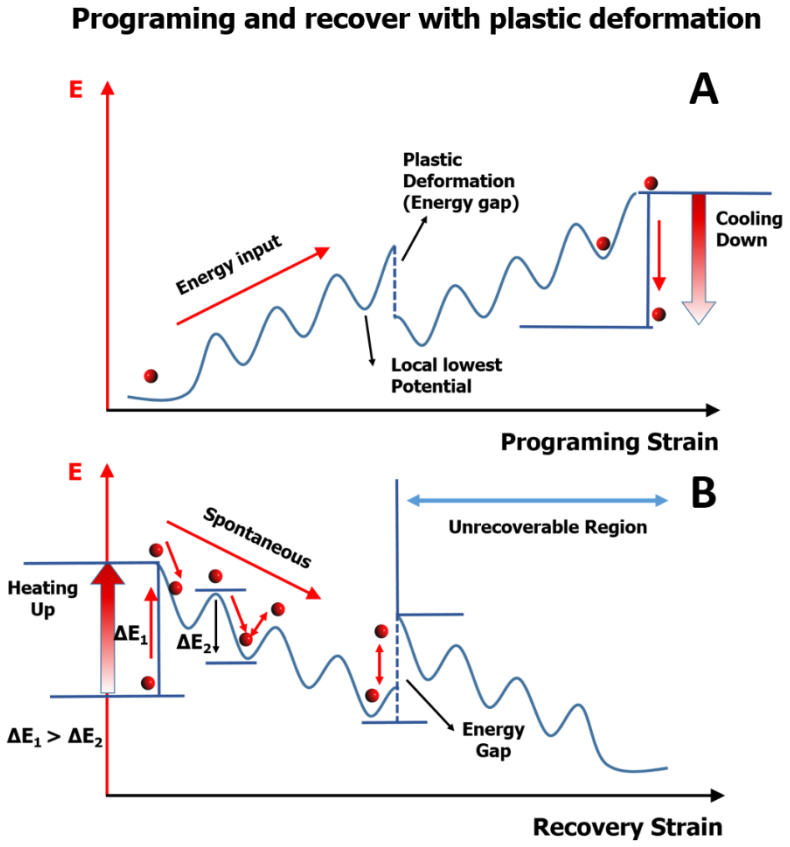

Figure 3.8. The interpretation of plastic deformation by "multiple energy well" model. (A) The formation of energy gap during the programming. (B) The plastic deformation prevents the shape recovering by an energy gap.

As shown in Figure 3.8B, energetic wells will break into discontinuous pieces if the permanent deformation happens. The energy absorbed when the SME is triggered will be consumed by the completed recovering part. If the rest of the energy is not able to overcome the energy gap formed by permanent deformation, the shape recovering will not happen for the residual shape (strain).

CHAPTER 4. STIMULI-RESPONSIVE CEMENT COMPOSITE WITH GIANT EXPANSION AND ENHANCED MECHANICAL PROPERTIES

4.1. Introduction

4.1.1. Expansive Additives for Cement

As an inherent property of cement, “dry shrinkage” can induce internal stress in structures. [43-47] Once this internal stress exceeds a critical value, such as the tensile strength of the cement, cracking will occur. Due to the need for extra water to ensure workability, dry shrinkage and corresponding cracks are unavoidable for conventional Portland cement, which is a grand challenge facing several industrial sectors. Based on different engineering applications, these cracks can lead to water permeation, gas or liquid leakage, corrosion of steel rebar or even collapse of some important structures. To compensate this disadvantage, some expansive systems have been designed, studied and applied since around eighty years ago. [43, 44] According to the foundation established by these investigations, some expansive cement systems have been used widely in civil engineering and petroleum industry. Among these systems, Ettringite system and magnesium oxide system are two main catalogs.

Ettringite system is named by the production of the chemical reaction during the expansion process. The main components are calcium sulfo aluminates (CaO-Al_3O_2-SO_3) series. So-called “expansive cement” is mentioned as the cement products mixed with these additives. Based on the main components, three types of expansive cement are standardized such as K-type, M-type and S-type. The admixture for the K-type cement is anhydrous Hauyne ($3CaO{\cdot}3Al_2O_3{\cdot}CaSO_4$), gypsum ($CaSO_4$) and quick line ($CaO$). For the M-type cement, it is gypsum and alumina cement. For the S-type, the admixture is gypsum and tricalcium aluminate (C_3A). When these admixtures are mixed with reasonable ratio of Portland cement, the corresponding expansive cement is obtained. Ettringite is the production of the reaction from calcium sulfo aluminate, calcium oxide

calcium sulfate and the right amount of water. The formula of Ettringite is $3C_3A \cdot 3CaSO_4 \cdot 32H_2O$. Here, C means CaO and A means Al_2O_3. The expansion mechanism of the Ettringite is still only be hypothesized. The common agreement is the swelling theory and crystal growth theory. Sometimes, the mechanism occurs differently due to the different conditions. [45, 47]

The second system for the expansive cement is magnesium oxide system. The expansion mechanism of this type of additive is the hydration reaction of the magnesium oxide. Compared to the ettringite system, this expansion process can last a very long time during both the early age of setting and the late age. Consequently, it can compensate the thermal shrinkage which is always happen at the late age of setting and this can prevent the thermal crack in mass cement and concrete structure, for example a dam. For the real application, the reactivity of the magnesium oxide needs certain method to control. The main approach to control this is the careful temperature performance of calcining and the residence time during the formation of the magnesium oxide. As a commercial product, the cement with a high concentration of magnesium oxide can be used directly or the additional amount of the magnesium oxide as the additive for the normal cement also works. [48-50]

For these systems as the expansive additive, some faults still limit their applications. Firstly, the additives both react with water. Especially for the ettringite, a massive amount of water is needed. So, the slurry with low portion of water is not suitable. Secondly, the temperature is another limitation. Regarding ettringite, the temperature can't exceed 70°C because the decomposition will happen. The temperature lower than 60°C is also not appropriate for the magnesium oxide system due to the slow hydration manner. Thirdly, the mechanical performance is reduced in terms of strength and stiffness. To meet the essential expansion, a certain amount of the expansive additive is necessary. However, in certain system, the strength and modulus are

significantly reduced by a small amount of addition of the additive. Fourthly, the expansion behavior of these systems still needs the enhancement. As the mention above, the amount of the additive is limited by controlling the mechanical property, consequently, the linear expansion for most of the systems is small. For example, 5% weight percent of MgO in G type cement only expands about 0.01% in linear expansion. More MgO than 5% will be the hazard for maintaining the mechanical property. [49] Therefore, if one additive has the following properties: (1) it doesn't react with water, (2) the temperature for the expansion process can be controlled or designed, (3) the mechanical performance of cement can be enhanced, (4) the efficiency of expansion is very high, it will be a promising candidate for the next generation of the expansive additive for cement.

Shape memory polymer is a new class of additive for the expansive admixture for cement which has the shape memory effect. [51, 52] Considering the expected properties as mentioned above, a polymer normally does not react with water. This is first benefit. Regarding the shape memory polymer, essentially, it is not a special type of polymer. But, it is a property of the polymer coming from the certain mechanical deformation with the appropriate polymer network. The process of this mechanical deformation is mentioned as "training", "education" or "programming". Several necessary elements are needed for this shape memory effect. Firstly, it needs certain phase transition including glass transition, melt/crystallization transition, order/disorder transition, etc. Secondly, it needs a trigger such as direct heat, indirect heat (current or voltage, etc), light, moisture, pH, etc. Thirdly, it needs mechanical deformation which is can be tensile, compression, bending or twisting. Finally, it needs a stable network. This network can be physical network such as entanglement of chains or ion cluster. It also can be chemical crosslinking points. For an example, assuming we use the direct heating, which is the most common trigger for the shape memory, and the glass transition, the typical process of a shape memory cycle is as following. At

the low temperature, the polymer is at the glassy state (cold). The original shape at this state is named as the permanent shape. When the sample is heated up until exceeding the glass transition region, it enters the rubber state. This soften polymer then can be deformed easily by a loading. If the loading is kept and the sample is cooled down to the cold state (glassy state), this mechanical deformation can be "memorized". This process is the so-called "programming". The new shape is called temporary shape. When the cooled sample is heated again up to the rubbery state, the shape memory effect is triggered, and the sample will transform back to the permanent shape from the temporary shape and this is so-called "recovering". The classic focus for the shape memory effect is for the transformation of the shape and it is where the name of this phenomenon comes from. However, as another intrinsic property of polymers, the compressibility is never paid attention before it is used as the expansive additive. The compressibility for the polymer means the volume of a polymer is possibly reduced by a mechanical deformation. Due to the shape memory effect, this reduced volume can be fixed by programming and it can grow back by a trigger. As a result, theoretically, all polymers can be the candidates for expansive additive of cement because all polymers have certain degree of shape memory effect. Because the transition temperature for the polymer is a selectable and designable property, a wide range of temperature can be used for the expansion. The efficiency is another advantage of shape memory polymer. It is much bigger than the expansion of ettringite and MgO. Nevertheless, how much the change of volume can be fixed or memorized is also another factor. This is determined by the detail of shape memory effect behind the polymer. For mechanical property, polymer typically is considered as the additive for the enhancement of the toughness or tensile strength. Compressive strength is still hard to enrich. Thus, it is more difficult to enhance the compressive strength at the same time with toughness or tensile strength.

4.1.2. Expansive Cement in Petroleum Industry

In petroleum industry, cement acts as a barrier to isolated oil- and gas-bearing zones from other formation to avoid any potential gas migration. With wide-spread application of hydraulic fracturing treatments and inherent large pressure fluctuations during these treatments, issues like sustaining casing pressure [53] and methane emissions [54] are appearing more frequently. These problems are also an indication that more work is needed to improve well integrity. To provide zonal isolation in a well, a strong bonding between cement and casing, and cement and surrounding rock interfaces is imperative. Recently developed numerical models can predict cement delamination at these interfaces, these models have revealed a complex behavior of cement sheath failure during its service life as a function dependent on a series of parameters [55, 56].

A series of factors can lead to debonding failure of the cement along its interfaces. During the productive life of the well, the pressure of the reservoirs gradually decreases due to depletion that causes casing contraction [57]. Also, during production, the casing can move as a result of subsidence of the formation [58] Cement shrinkage due to hydration may reduce cement volume around 4% [59]. Finally, mechanical or chemical degradation [60] in the long-term can lead to debonding. Depending on the severity, the failure can vary from small channels to microannulus ranging from partial debonding to whole circumferential debonding.

Expanding additives can mitigate these problems owing to their expansion after the initial cement set, resulting in the development of a stress condition in the cement that helps to sustain bonding during pressure variations. The overall result is improved zonal isolation. Regardless, the environmental condition for the sheath of the well is different from the common case for the use of cement. Different terrain or depth underground can lead different temperature and pressure. For the temperature, it can be as high as 150 °C. Under the extreme condition like this, ettringite

systems, where the expansion is based on crystal growth from chemical reactions, are not suitable to be used. [56, 61, 62]. Many of these additives are showing problems related to its stability [63]. For the magnesium oxide system, the high temperature may not a challenge. However, the common cement type for the sheath of well is class G or class H. The reduction of compressive strength for these two types of cement by MgO is too massive. Moreover, when considering the expansion of the sheath of the well, the circumferential expansion is more important than the linear expansion. Based on the relationship between them, the circumferential change is only 35% of the linear change. Consequently, the ability of expansion needs to be enhanced tremendously. As the requirement of these, some new types of additive of cement for petroleum industry is demanded. The use of shape memory polymers as an inert expansive additive, to overcome this limitation, was first proposed by D. Taleghani and G. Li *et a*l. [51]. In this work, the commercially available ionomer named "surlyn" was used. The polymer beads were programmed by compression and then they were served as the expansive additive for H class cement. These programed surlyn beads were active by the heat generated by the curing of cement which is between 50°C and 100°C. Although the compressive strength and modulus were reduced by this additive, they were able to meet the satisfaction of the requirement of most oil and gas fields operations. However, the strength of class G cement is much lower than the class H cement. So, the use of it as the additive of class G cement may lead to a big challenge. Moreover, it may not suitable for the high temperature zone underground. The work was further extended by using the additive in the shape of fiber to improve the tensile mechanical properties of the cement sheath and control fracture propagation [52].

Different techniques can be used to evaluate cement expansion/shrinkage. Works by Goboncan and Dillenbeck [64] and van Eijden *et al*. [65] provide a review of current methods and

equipment available. In this work, the annular expansion ring test is used, which is the test recommended by American Petroleum Institute (API). The annular ring mold consists of a bottom plate, inner ring, outer expandable ring with two steel balls in the outer face, and a top plate. As the annular ring is fully confined from top to bottom, the expansion is linear horizontally.

4.1.3. Introduction for This Study

This study is the following and expansion of the previous study of the high enthalpy storage thermoset network with giant stress and energy output in rubbery state. As mentioned above, shape memory polymer has been introduced as the expansive additive of the cement by our previous study. The property of the expansion has been confirmed. Nevertheless, some problems are still existing. First, for the cement used in deep underground, the temperature is as high as 150°C and the expansion additive at this temperature range is needed. Secondly, the mechanical property of the cement is still reduced by the addition of the additive of shape memory polymer. So, the amount of the expansion additive is limited. Thirdly, with this limited the weight percentage of the additive, the best circumferential expansion is between 0.5% and 1% which is still not achieved. Based on the demanding of the new expansive additive made from shape memory polymer and the property of the new shape memory network by EPON-IPD, this new shape memory thermoset polymer is very possible a good candidate for the new expansive additive for cement.

To serve as the additive of the cement, the bulky EPON-IPD material is fabricated into particle and powder two forms. Due to this, the factor of size can also be studied. With the sample methodology of the previous study, the expansion manner, mechanical properties are tested. Moreover, the rheology of the slurry is also characterized. The mixability and pumpability can be indicated by the result of the rheology test. The dispersion of the additive and the interaction between the additive and cement are studied by scanning electron microscopy and the associated

energy dispersive X-ray spectroscopy. The interaction is also evaluation by the X-ray photoelectron spectroscopy and the mechanical method established by our previous study which is call end notched flexure test.

4.2. Experimental Study

4.2.1. Materials

The bulky EPON-IPD is synthesized by the same procedure described in the Chapter 2. The type G cement is provided from the group of Pennsylvania State University. The cement is used directly without any further purification or modification.

4.2.2. Fabrication of the Shape Memory Expansive Additive

The bulky EPON-IPD was obtained first as the raw SMP. The raw SMP block sample was uniaxially compressed at 160°C until some crack appeared (about 45% of compressive strain). This is for the convenience of breaking the bulky sample into smaller pieces. After cooling the compressed SMP block sample down to the room temperature, it was broken into pieces and crashed by press again into much smaller sized grains. These crashed grains were milled by the PQ-N2 planetary ball mill machine (Across international). Every half hour, the ball milling machine was stopped, and sieves with one-millimeter holes was used to obtained different sized particles, all the way to fine powders. All product was screened by a 150 μm sieve to make sure that the size of powder is small than 150 μm and the particle size is bigger than that. The fabricated powder and particle are showed as the Figure 4.1.

4.2.3. Expansion Test

Class G cement was used with 0.44 water/cement ratio. The expanding additive was dry-blended with the cement at four different concentrations by weight of cement (BWOC), 1, 2, 4 and 6%, before the addition of water.

The evaluation of the cement expansion is conducted by following API RP 10B-5 (API, 2005), which provides the standards to measure expansion of the cement sheath. Following its preparation, the slurry is placed in the annular ring expansion test and the mold is taken to a curing chamber for 24 hours to cure under 320 ºF (160 ºC), and 3000 psi (20 MPa) pressure. The linear expansion was measured by measuring the distance between the steel balls on the mold before and after curing, and applying the following equation to calculate the circumferential expansion:

$$\Delta L = (L_f - L_i) \times 0.358$$

where L_f and L_i are the final and initial distance, the different of them suggests the linear expansion, respectively, measured in millimeters.

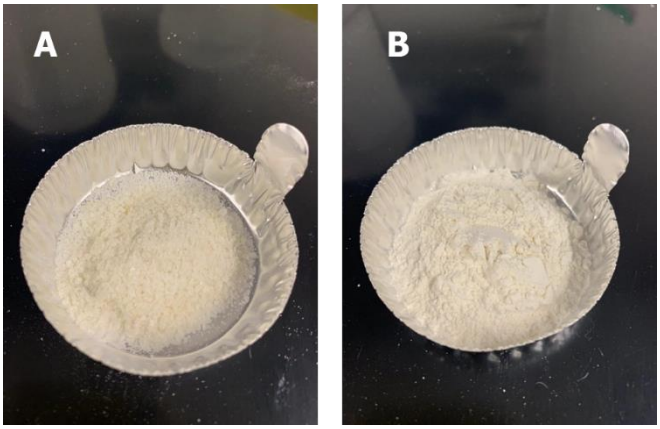

Figure 4.1. The product of ball-milled EPON-IPD. A (particles), B (powder).

4.2.4. Rheology Characterization

A rotational rheometer (Fann model 35) was used to measure the slurry's rheological properties. The measurements were taken at ambient temperature. The relationship between the shear stress and shear strain rate was measured. The plotted curve was used to curve fit the parameters in Herschel-Bulkley model, from which, the mixability and the pumpability are analyzed.

4.2.5. Mechanical Evaluation

4.2.5.1. The Mechanical Property by Compression

The sample preparation of the compression test followed the API-10B ASTM standard. Two inches cube samples were fabricated. The cement and the cement with the additive were cured at 65°C under about 7MPa for 48 hours. Before the test, the samples with the mold are placed in the 23°C water for 24 hours.

4.2.5.2. The Mechanical Property under Flexure

The three-point bending test was used to test the effect of the additive on the flexure strength. The span length is 50.8mm. The width and the height of the samples are 15mm and 20mm, respectively. The samples with different concentration of additives were also cured at the 65℃ under atmospheric pressure for 48 hours. Again, before the test, the samples with the mold were immersed in the 23°C water until 15 minutes before the test.

4.2.6. Scanning Electron Microscopy

The morphology of the microstructure of the pure cement and the cement with the additives are imaged by the Quanta^{TM} 3D Dual Beam^{TM} FEG FIB-SEM system. The samples with powder additives fractured by compression test are utilized. The interfacial fracture surface is observed.

4.2.7. Energy-dispersive X-ray Spectroscopy and Element Mapping

The element distribution is characterized by the energy-dispersive X-ray spectroscopy (EDS) system (Pegasus) integrated with the FEG FIB-SEM system under 20 kV. The total collecting time for the mapping is 17 minutes. The linear scanning is also conducted for the study of the interfacial interaction between the cement grain and the particle surface.

4.2.8. Measurement of the Contact Angle

The wetting property is characterized by the measurement of the contact angle of cement slurry on a flat bulky sample made from EPON-IPD. The contact angle is measured by the software associated with the machine.

4.3. Results and Discussion

The expansion of the particles and powder are illustrated in Figure 4.2. Both curves follow a liner relationship between the expansion and the concentration of the SMP additives. For the cement with powder additive at a concentration of 6%, the linear expansion reached as large as 1.4%. The expansion results are much higher than the ones obtained by Ettringite systems, which is only 0.25% expansion at a concentration of 5% additive, and the MgO system. Considering the recovery stress of the EPON-IPD is around 17MPa, the reason that it can expand under 3000 psi is that further three-dimensionally compressive programming was conduct by the test condition.

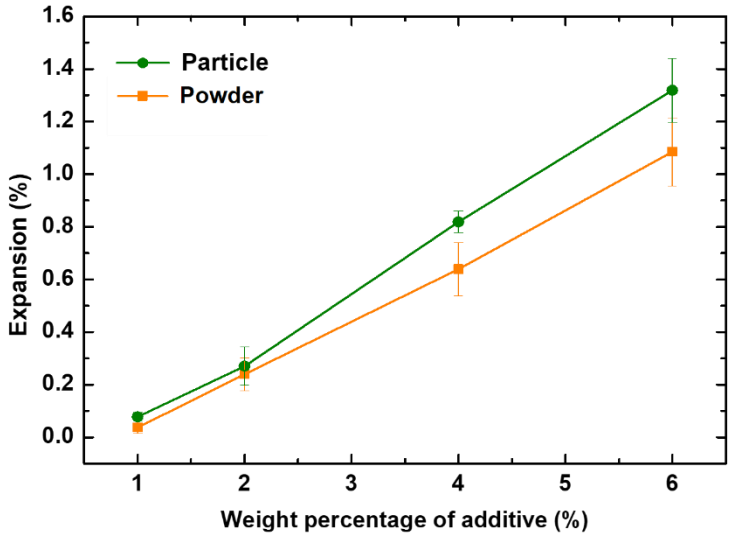

Figure 4.2. The expansion ability of the class G cement with different concentrations of EPON-IPD powder or particle under serving conditions (150℃ and 3000 psi).

For expansive cement composite used in the oil industry, the mixability and the pumpability of additive are both critical characteristics. Therefore, the rheological property is a crucial parameter to evaluate. Rheological measurements can determine the flow characteristics of the cement slurry such as its plastic viscosity, yield point, frictional properties, and gel strength. These properties determine the quality of the final product and ensure that the slurry can be pumped into the well with minimum pressure drops. Viscosity is the most significant property in this regard and it measures the relationship between the shear stress and shear rate. It also plays a critical role in mud removal.

The fitted rheological curves of the plain cement, cement with 6% powder and cement with 6% particle are plotted in Figure 4.3. The shear stress increases with the addition of SMP but the slurry still demonstrates good mixability due to the absence of the unsmooth curve.

Based on the preliminary study of the rheology of the plain cement, the Herschel-Bulkley model is applied here:

$$\tau = \tau_y + k \times \dot{\gamma}^n$$

where τ is the shear stress, $\dot{\gamma}$ is the shear strain rate, τ_y is the Bingham yield stress, k is the consistency index and n is the flow index. Curve fitting was conducted to determine k and n. The obtained values of the Bingham yield stress, consistency index and the flow index are listed in Table 4.1. The value of n indicates that if a system is a shear thinner or shear thicker system. When the n is greater than 1, the shear stress will increase faster with the increasing shear strain rate and this case is called shear thicker. For the shear thicker system, the shear stress will reach the critical value for the pumpability very quickly. In contrast, if the n is less than 1, the shear stress will increase at a reducing rate, although it keeps increasing with shear strain rate. Hence, it is named as shear thinner system. According the values of n in the Table 4.1, the class G cement composites with both the powder and particle EPON-IPD are shear thinner system. This will lead to a good pumpability in practice.

Table 4.1. The simulated parameters of the Herschel-Bulkley model

Samples	$\boldsymbol{\tau_y}$ **Bingham yield stress (Pa)**	$\boldsymbol{k}$ **Consistency index**	$\boldsymbol{n}$ **Flow index**
Plain cement (PC)	3.0	1.05	0.53
PC with 6% EPON-IPD powder	4.8	1.30	0.52
PC with 6% EPON-IPD Particle	6.1	1.38	0.54

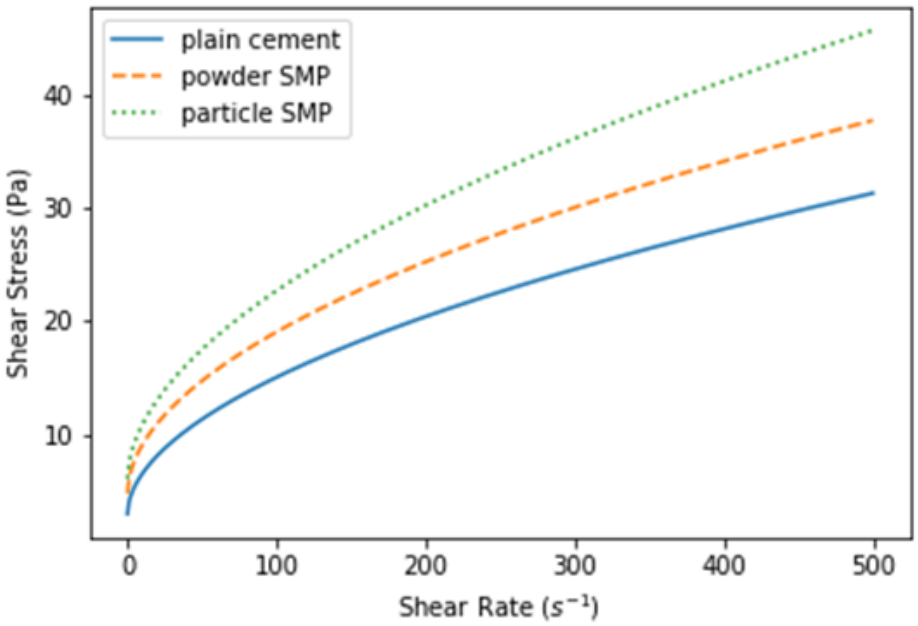

Figure 4.3. Rheological curves for plain cement and cement with 6% concentration of additives, following Herschel-Buckley model.

The Figure 4.4 is showing the samples for compression test and the cracks of the fracture for pure cement (A, B) and the cement with the 4% powder additive (C, D). The cracks are mainly vertical as the normal fracture pattern.

One big concern with expansive cement additives used in the well and petroleum industry is the mechanical properties. For conventional additives, they are difficult to maintain the required mechanical properties, especially for compressive strength. As a class of new additive, it is crucial to evaluate the compressive of the cement composite.

The compressive strength is illustrated in Figure 4.5. It is found that the compressive strength can be enhanced by both powder additive and particle additive. Four percent of the additive lead the cement to the highest strength. By incorporating 4% additives, the compressive strength reaches 27.5MPa and 25.0MPa, for particles and powders, respectively, which is much higher than the plain cement which is only16.3 MPa. Usually, expansive additive is difficult to maintain the

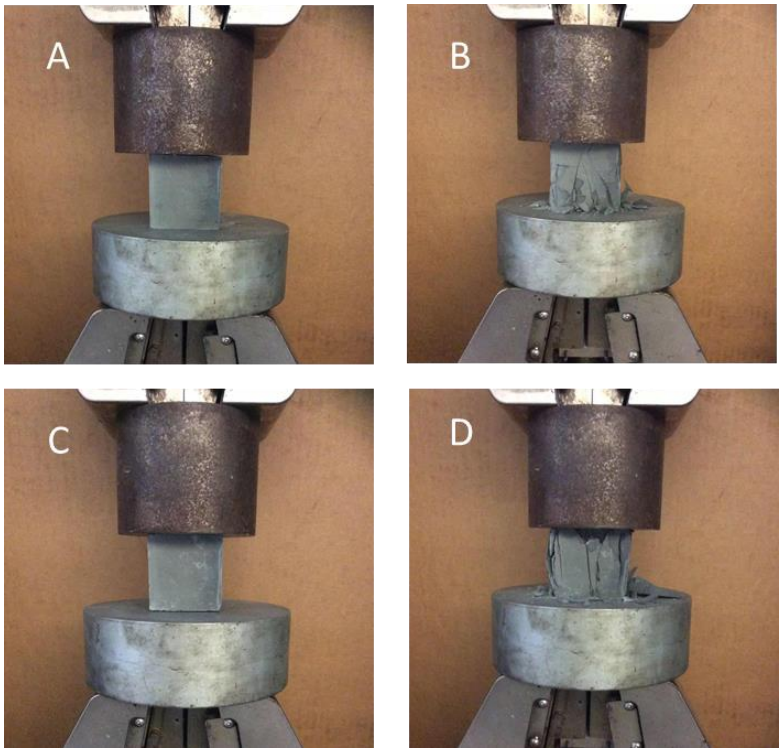

Figure 4.4. The fracture mode of compression for the pure cement (from A to B) and the cement with 4% powder additive (from C to D).

compressive strength, not to mention increasing the compressive strength. Therefore, the SMP additive used in study is unique in terms its ability to enhance the compressive strength, in addition to provide the exceptional expansion. One reason for this is that the inert SMP has higher modulus than the plain cement, and thus the hard particles reinforce the soft cement matrix, leading to enhanced compressive strength and Young's modulus; see Figure 4.5B. SMP in particle form leads to higher compressive strength than SMP in powder form, which may be due to the large interlocking between particles than between powders. For the Young's modulus, the particles and powders do not make much difference, because the stiffness is more dependent on the volume fraction of the additives. Regarding the compressive failure strain, Figure 4.5C, a similar tendency to compressive strength can be seen. With the increase in compressive strength, stiffness, and failure strain, the cement composite is an ideal material for the drilling industry.

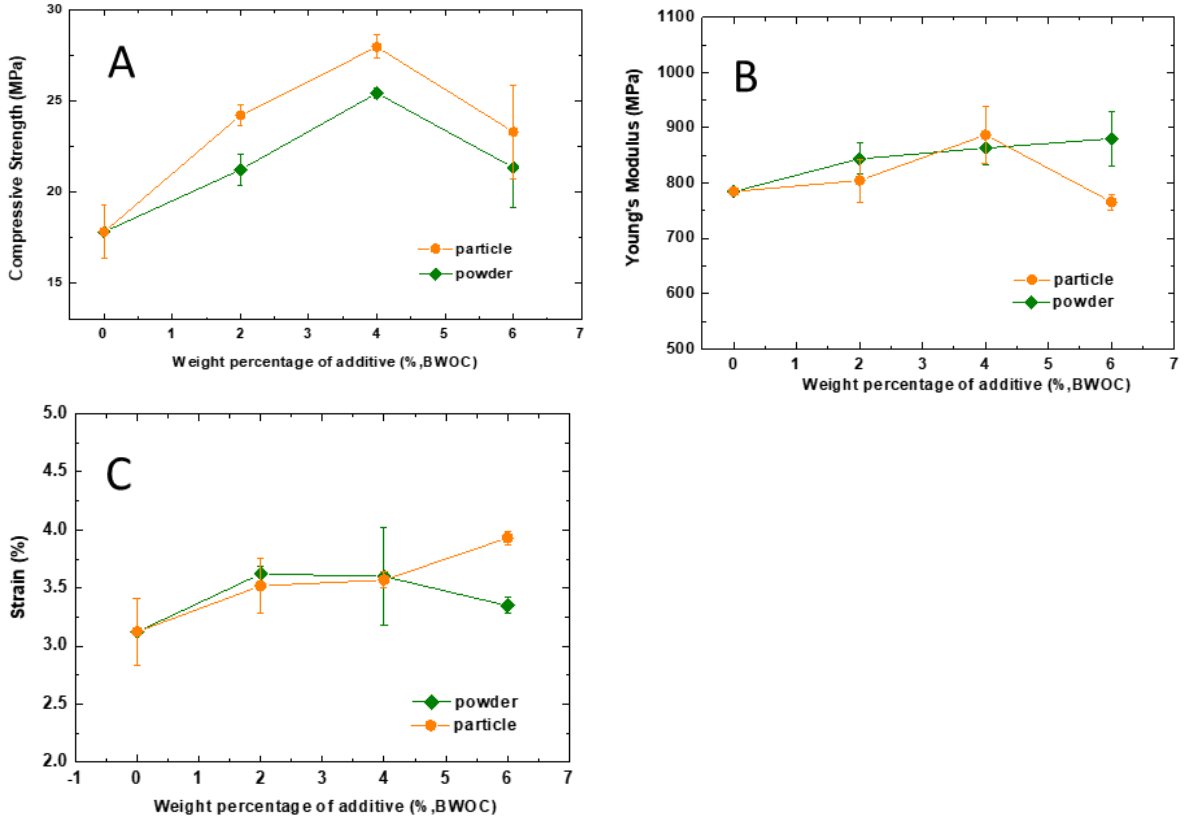

Figure 4.5. The results of compression test: (A) strength, (B) Modulus and (C) Strain.

Once the concentration of the SMP particles or powders reach 6%, the change of the compressive behavior between the two forms of additives becomes complex. The reason may be that, once the inclusions are high enough, the interaction between the inclusions plays an important role. Also, uniform dispersion of the inclusions becomes difficult. Fortunately, with 4% by weight of inclusions, which can be considered as a dilute particulate composite, the expansion is within the ideal or desired range of 0.5% - 1.0%. Together with the optimal mechanical properties, 4% by weight is recommended for underground drilling applications.

The flexural strength also deserves comments. As shown in Figure 4.6, the flexure strength of the cement composite is basically higher than the plain cement. This is highly desired for the composite to resists possible transverse loading.

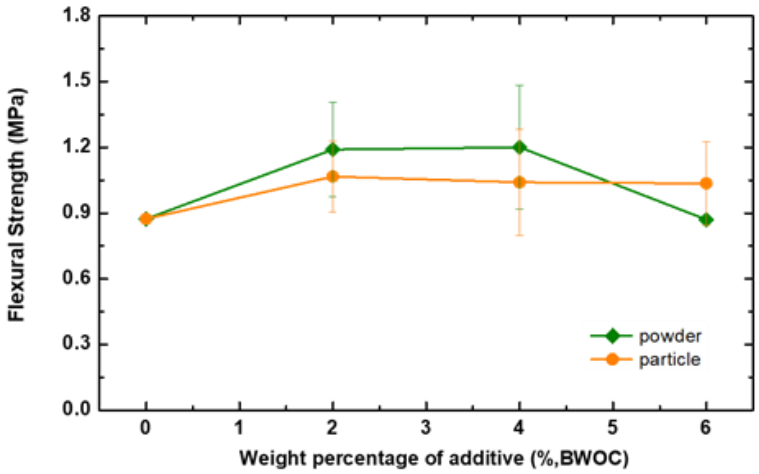

Figure 4.6. The flexural strength of the class G cement with different concentrations of additive in powder or particle form.

Overall, the cement composite can be treated as a particulate composite, which follows a certain rule of mixtures principles, i.e., hard particles in soft matrix, leading to increased strength and stiffness as compared to the plain matrix.

The dispersion of the additives and the interaction between them and the cement matrix normally determine the mechanical properties. Consequently, the morphology and dispersion of the additives in the cement matrix are studied by the scanning electron microscopy (SEM) and the energy dispersive X-ray spectrum (EDS). Figure 4.7 shows the SEM images, which compare the morphology of the pure cement and the cement composites. Typical morphology can be observed such as some crystal rods in the pure cement. From the element mapping in Figure 4.8 and the normal process of the hydration of cement, these long crystal rods should be calcium sulphate and alumina, ferric oxide phase. No special morphology for the polymer powder can be observed. The polymer phase is well mixed with the phase of cement. No phase separation can be found.

Figure 4.8 is comparing the morphology of the pure cement and the cement with the additives. No obvious different can be observed except some long crystal rod in the pure cement. From the

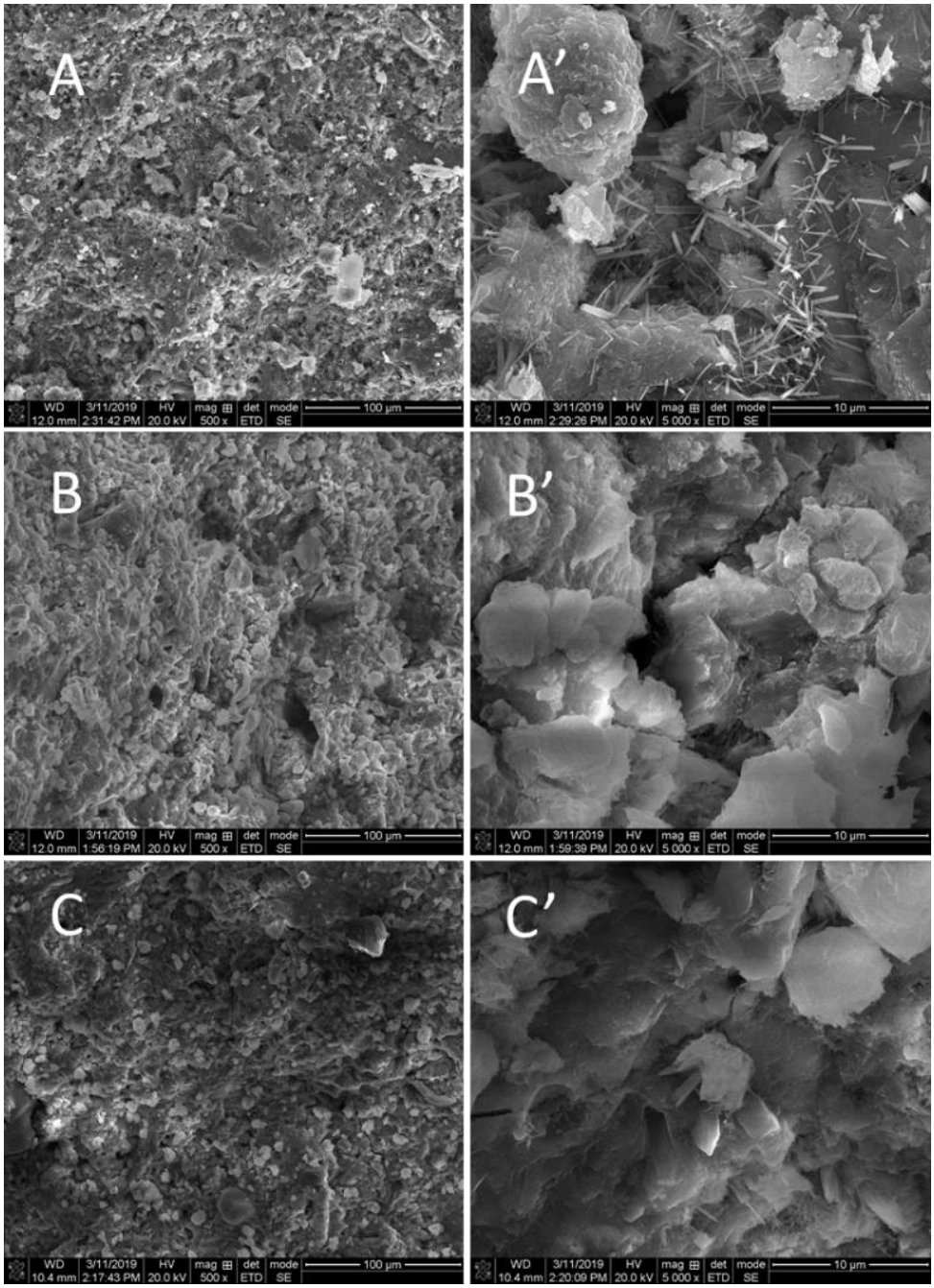

Figure 4.7. The scanning electron microscopy images for the morphology of fracture surface on (A) pour cement under 500× magnification. (A') pour cement under 5000× magnification. (B) cement with 4% powder additive under 500× magnification. (B') cement with 4% powder additive under 5000× magnification. (C) cement with 6% powder additive under 500× magnification. (C') cement with 6% powder additive under 5000× magnification.

element mapping in Figure 4.8, these long crystal rod should be calcium sulphate and alumina, ferric oxide phase. There is no particular morphology for the polymer powder.

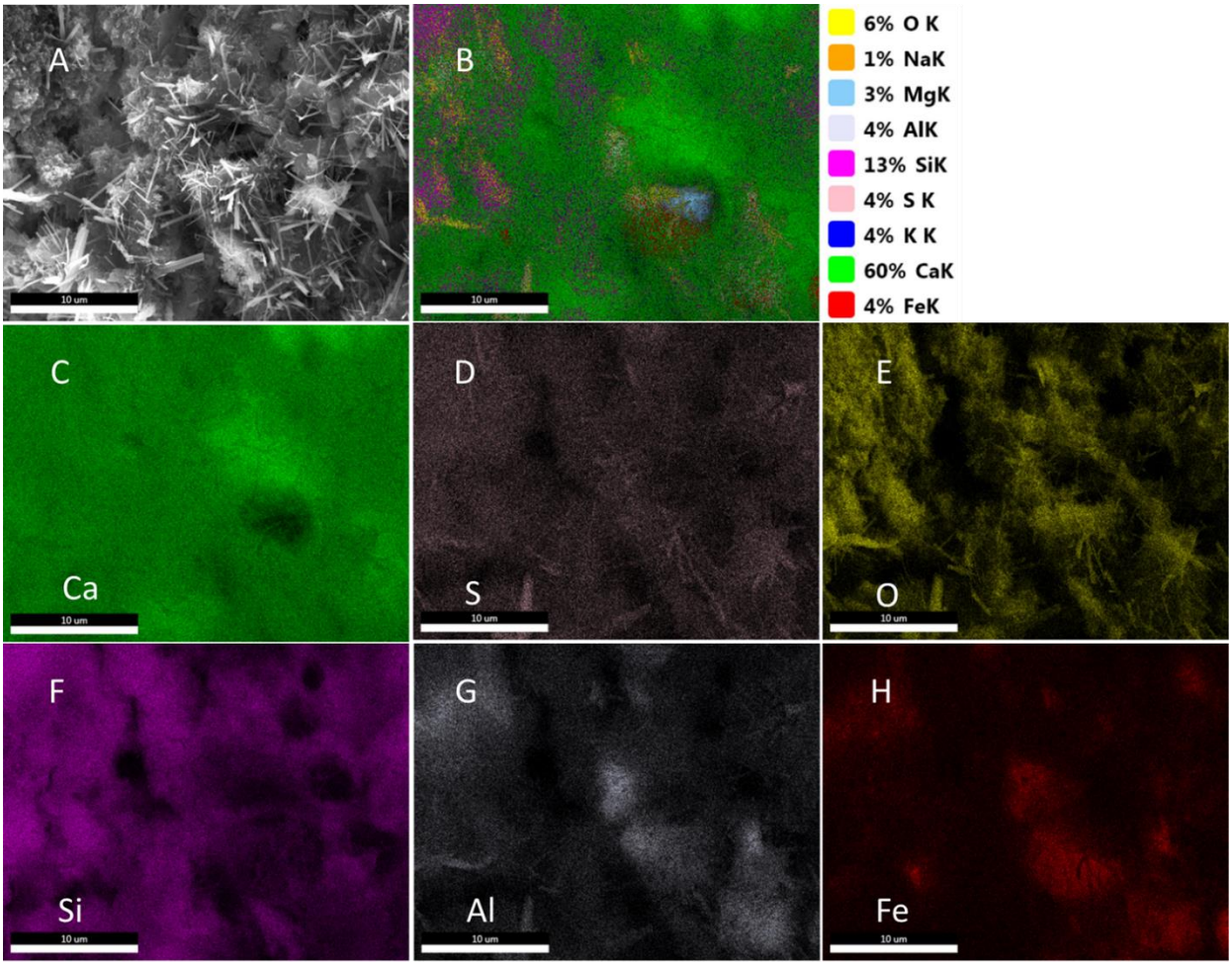

Figure 4.8. The scanning electron microscopy image of (A) the surface of the pure cement and the element mapping: (B) the overlap of all detected elements, (C) element calcium, (D) element sulfur, (E) element oxygen, (F) element silicon, (G) element aluminum, (H) element iron.

From Figure 4.9, the image of the cement with 6% powder additive is illustrated with the element mapping. The Figure 4.9B is an overlap or supposition of all the elements in the composite. Figure 4.9C - Figure 4.9K are the mapping of individual element in the cement composite. The light blue areas show the element carbon rich phase, which represents the polymer additive. The carbon phase is complementary with the rest area which contains calcium as the green color in the Figure 4.9D. The aluminum (Figure 4.9G, grey) and iron (Figure 4.9H, red) are very similar to each other and they are complementary to the silicon (Figure 4.9F, purple). This can separate the

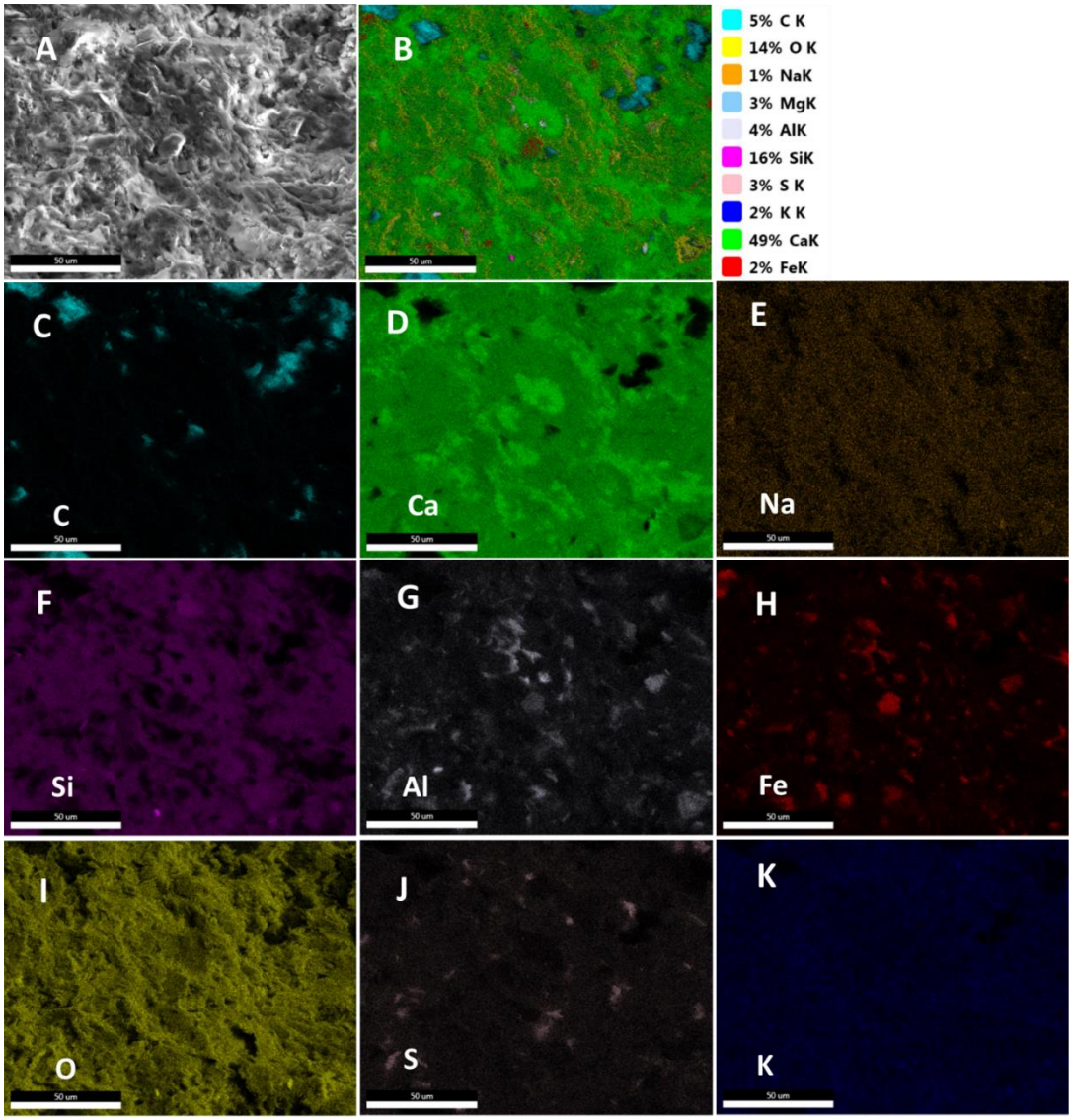

Figure 4.9. The scanning electron microscopy image of (A) the surface of the cement with 6% powder additive and the element mapping: (B) the overlap of all detected elements, (C) element C, this phase indicating the polymer additive, (D) element calcium, (E) element sodium, (F) element silicon, (G) element aluminum, (H) element iron, (I) element oxygen, (J) element sulfur and (K) element potassium.

alumina, ferric oxide, tri-sulfate (Al_2O_3-Fe_2O_3-tri) phase (AFt) and alumina, ferric oxide, mono-sulfate (Al_2O_3-Fe_2O_3-mono) phase (AFm) from the C-S-H (calcium silicate hydrate) phase. By examining the Figure 4.9B with the individual element mappings, it is clear that no phase separation is observed by the morphology of the cement with additive even on the surface of the

fracture. This confirms the polymer powder can interact closely with the grain of the cement. Otherwise, if the SMP powders are pulled out from the cement matrix on the fracture surface, the carbon signature will be lost.

To further examine the interfacial interaction between the SMP and the cement matrix, a linear EDA scanning across the interface was were conducted for a cement composite consisting of 6% of SMP particles, see Figure 4.10A. The gap at the image center shows the edge of the particle and the cement matrix. The cement is on the left-hand side, and the right-hand side is the edge of the particle as pointed in Figure 4.10B. The element calcium and iron are rich at the left-hand side. As shown in the SEM image, they are AFt and AFm phases. When the scanning crosses the gap between the cement and EPON-IPD particle, the element carbon increases immediately, together with the element silicon. Although the calcium decreases significantly in this area, it maintains a certain amount. This suggests that a C-S-H layer grows on the surface of the polymer particle, or even diffused into the SMP particle. Figure 4.10C shows the contact angle test between the cement slurry and the SMP particle. The contact angle is between 30º and 31º, which is very close to the conventional cement and the aggregates [66], suggesting that the cement slurry has a good wettability with the SMP particle. In other words, the SMP particles have good interfacial bonding with the cement matrix, which is the reason for the enhanced mechanical properties of the cement composites.

The hydration process occurring around the polymer additive is hypothesized in Figure 4.11. For the irregularly shaped SMP particle, it has different surface energies depending on its gematrical configuration, such as flat surfaces, rough surfaces and the vertexes. The area with high surface energy will attract more water dissolved with ions. The surface of the polymer is porous and due to the different potential energy between the vacancy in the pores and the water with ions,

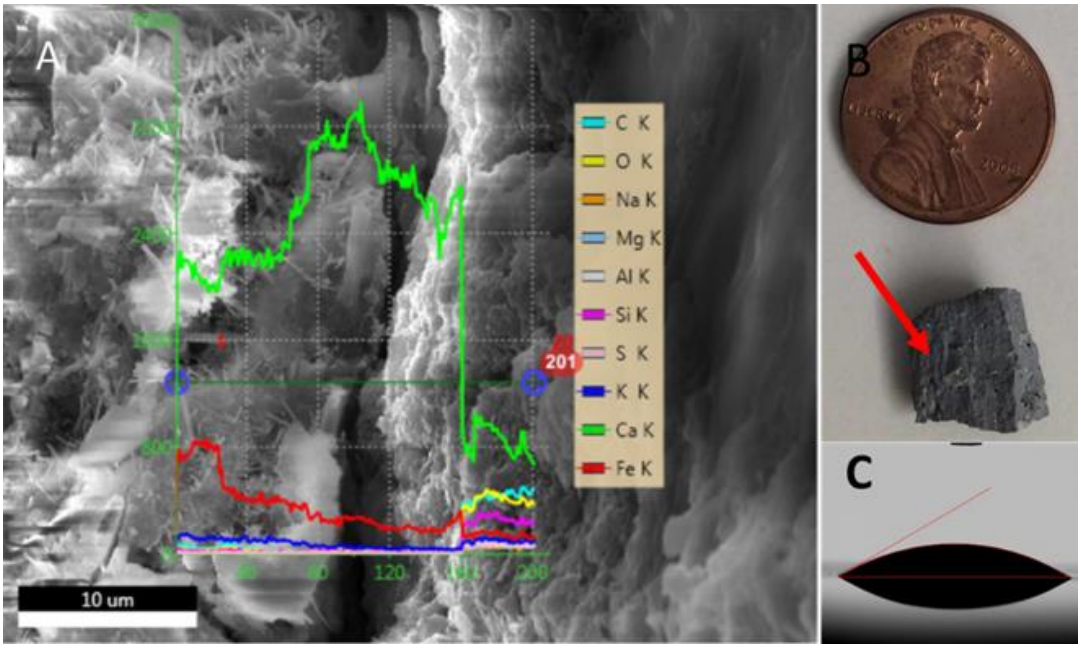

Figure 4.10. (A) The SEM image of the edge of the particle in the cement with 6% particle additive and the linear scanning of the EDS profiles for presenting elements. (B) The sample used for the image. The location of the edge is pointed by the red arrow. (C) The contact angle test of the flat bulky EPON-IPD sample shows the wetting ability.

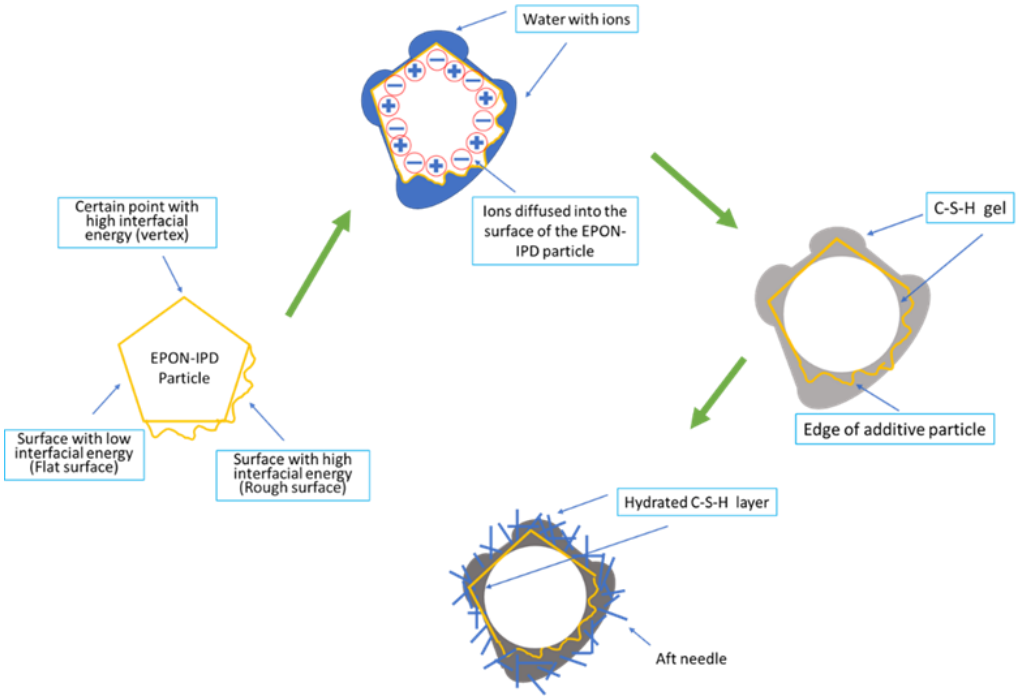

Figure 4.11. The hypothesized hydration process occurring around the EPON-IPD particle.

the ions can diffuse into the surface of the polymer. After hydration, typical C-S-H gel and a solid layer will form. During this process, the Calcium hydroxide, AFt and AFm phase will diffuse out of the C-S-H gel, similar to the conventional hydration process of the cement grain. Subsequently, the needle and flake shape alumina, ferric oxide phase can be found at the connection region between the particle and the cement matrix. Because this C-S-H layer physically joins or bonds the polymer particle and the cement matrix, this cement composite with the EPON-IPD additive can exhibit a high mechanical performance.

4.4. Conclusion

The circumferential expansion ratio of the cement G composite can reach 1.4% by adding 6% by weight of EPON-IPD particle. This new thermoset shape memory network can enhance the mechanical properties of the class G cement in terms of compressive strength, flexure strength, Young's modulus, and compressive failure strain. This excellent but rare characteristics is due to the close interaction between the additive and the cement matrix. A layer of C-S-H is found inside and on the surface of the polymer particle, providing strong interfacial bonding between the SMP particle and the cement matrix. The morphology and particle size also affect the performance of the expansive additive. In general, larger size is beneficial for the expansion and the mechanical properties. The cement composite may find application where both expansion and mechanical properties are critical.

CHAPTER 5. FIBER REINFORCED POLYMER COMPOSITE REBAR MADE BY E-TYPE GLASS FIBER AND EPON-IPD MATERIX

5.1. Introduction

One challenge facing fiber reinforced polymer (FRP) rebar and steel rebar in concrete structures persists in the fact that, for bending members such as beams or slabs, cracks in the tension zone cannot be narrowed or closed. [67, 68] Actually, with time, the cracks will open wider and wider, due to the creep of FRP rebar and steel rebar, and concrete. [69] The wide-opened cracks not only allow corrosion of steel rebars and increase fire and moisture hazard for FRP rebars, but also increase the deflection of the beams or slabs. Sometimes, the deflection may exceed the safety limit.

Such limitations for conventional FRP rebar and steel rebar can be overcome by using shape memory polymer (SMP)-based rebar. SMP rebars, after programming, can store the energy for a long time unless triggered for recovery. Once the cracks open wide enough, the shape recovery of the SMP rebar can be triggered, for instance by heating *in-situ*, or by applying electricity to the SMP rebar if conducting continuous carbon fiber is used to reinforce the SMP matrix, or the SMP matrix is filled in with conducting fillers such as carbon nanotubes, carbon blacks, etc., and the stored stress may be able to close the crack and reduce deflection.

One straight forward way of preparing SMP rebar-reinforced concrete beam is to program the rebar by tension before it is embedded in the tension zone, i.e., the zone beneath the neutral axis of the beam. When triggered, the tension programmed rebar shrinks, and brings the cracked concrete surface in contact. Another way is to prepare curved SMP rebar, and program the rebar by bending, until it becomes a straight rebar. When triggered, the straight rebar tends to go back to the curved shape, leading to closure of the cracks as Figure 5.1.

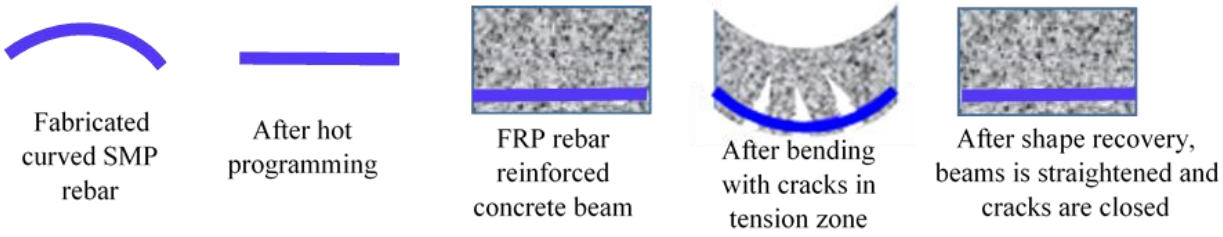

Figure 5.1. Schematic of fabricating curved rebar and its working principle.

Another strategy also can be conducted with the FRP which is not programmed as the Figure 5.2. If the FRP rebar can be cold programmed by the loading and the bending also lead the cracks in the tension zone. The cracks can be closed by the elastic spring back and the shape memory effect. As a result, the reinforced rebar can turn to be straight.

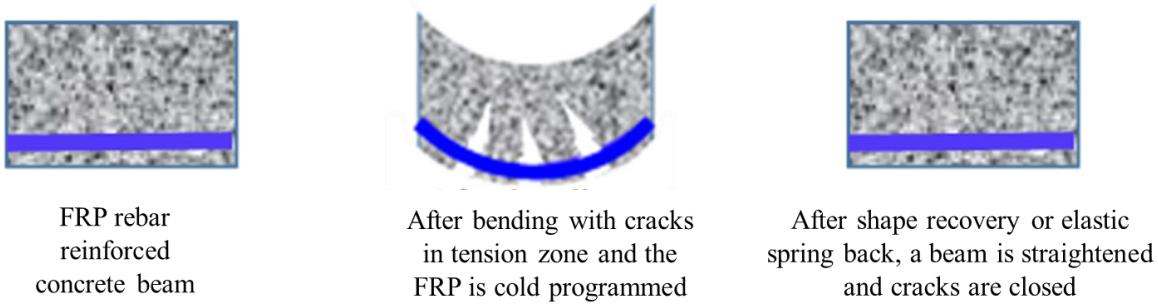

Figure 5.2. Schematic of the working principle for un-programmed FRP.

In this study, both strategies as showed in the Figure 5.1 and Figure 5.2 are considered. The FRP rebar made of E-type glass fiber and the EPON-IPD matrix were fabricated. For the curved rebars, the hot programming and the recovery force test were applied. Due to the programmed rebars were not actually straight and this will bring some trouble for next step of fabrication. The second strategy, then, was used. One more problem may occur for the programmed FRP is that the stored internal energy will reduced the deflection of elastic bending. The FRP may break quickly. The straight FRP with 50% and 70% volume fraction were fabricated for the second strategy. To enhance the interaction of the surface between FRP and the concrete, threads we added to the

straight FPR by curing another layer of EPON-IPD resin. The fabricated FRPs were placed in a wood mold as the design according to the ACI 440-15 standard. The three-point bending test was conducted and the mode of cracks were observed.

5.2. Experimental Study

5.2.1. The Fabrication of the Curved and Straight FRP

The FRP rebars are fabricated by the manual pultrusion as the following steps. First, one end of the glass fiber (Fiberex Technologies, CAN) was soaked in the EPON-IPD resin. This end was then placed in a short Teflon tube with the same diameter which is 6mm as the Teflon tube will be used as the mold during curing. A steel hook was inserted into the glass fiber with resin before the stub was cured by heat gun. The hook is used for pulling the fiber in the later step. After the stub is cured, the rest of fiber was soaked in the EPON-IPD resin in a vacuum oven at 45°C. The vacuum can extract the bubbles in the resin and it also can help the fiber wet and saturate in the resin. When almost no bubble can be extracted, the saturated fiber with resin was pulled into the Teflon tube with 6mm inner diameter manually. The difference between the curved FRP and straight ones is that if the tube is bended or not during the curing. The curvature at the center of the rebar is 2.86/m, or radius of curvature is 0.35 m. The curing was conducted at the 90°C for 45 minutes and then 150°C for 10 minutes for post-curing. The curved and straight FRP are illustrated as the Figure 5.3A and B. The thread was added to the straight FRP to become a rebar by curing another layer of EPON-IPD resin. The threads were formed by another Teflon tube with threads inside. The straight FRP rebar is illustrated in the Figure 5.3C.

5.2.2. Programming and Recovering of the Curved FRP

The cured SMP rebar was programmed by transversely compressing the rebar at 160°C in a designed mold as shown in Figure 5.4. The distance between the two holes is 120mm and the

distance between the top edge of the hole and the top of the mold is 6 mm, which is the diameter of the SMP rebar. After cooling down to room temperature by spreading water, the programmed SMP rebar was obtained. Figure 5.5A shows the programming process in the oven.

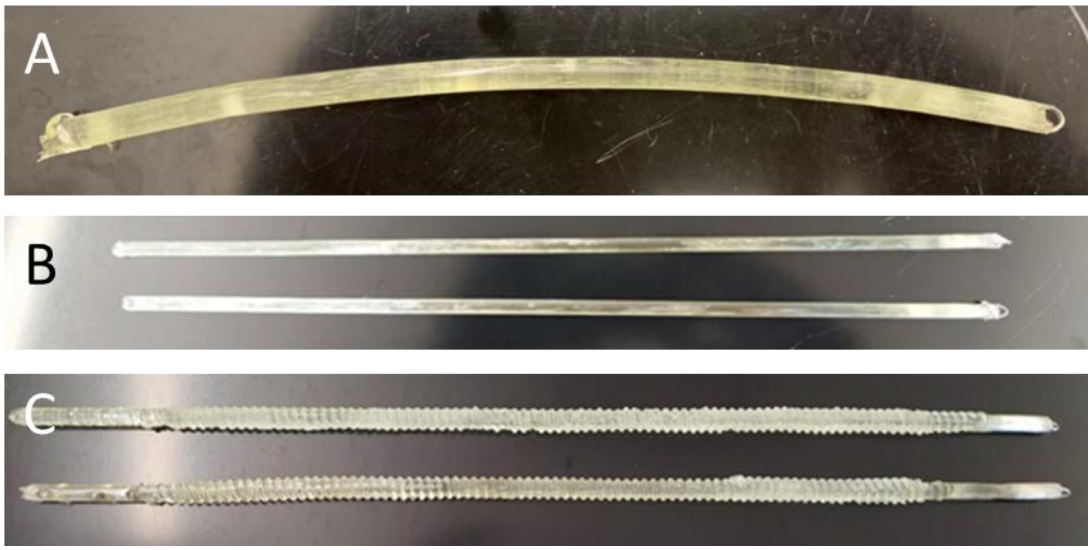

Figure 5.3. The cured SMP FRP rebar after curing (A) curved FPR (B) straight FRP (C) straight FRP rebar with threads.

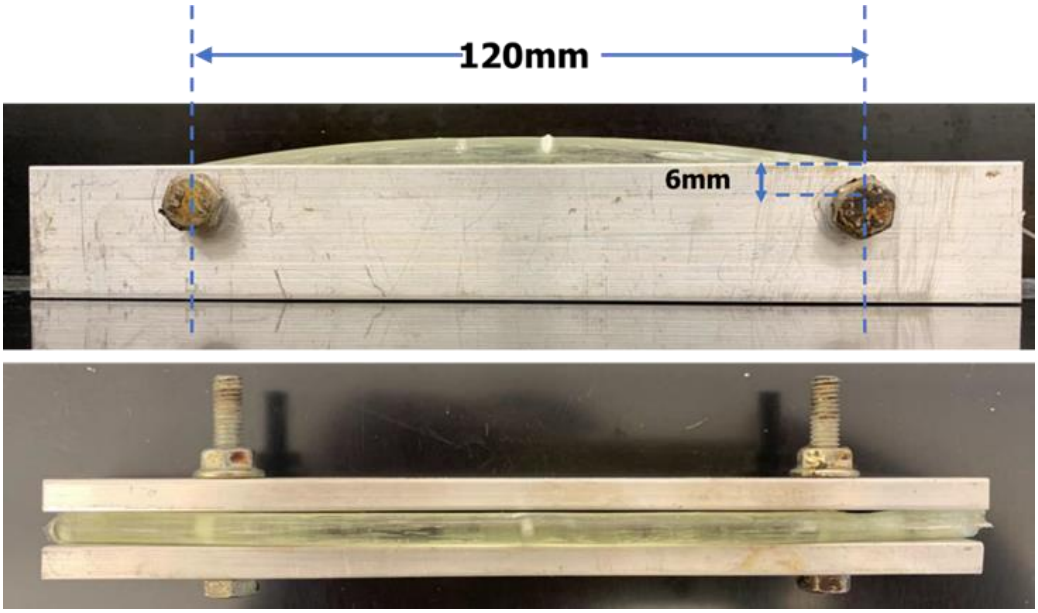

Figure 5.4. The mold used for programming and recovering with the rebar in it (top: side view; bottom: top view).

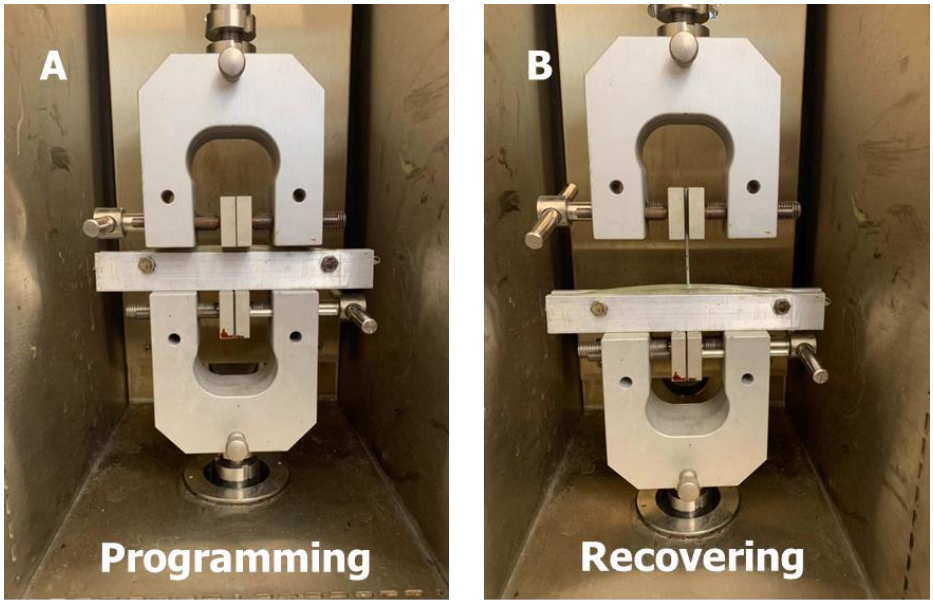

Figure 5.5. Programming and recovering process of the curved rebar in the oven.

The recovery force was obtained by the same mold used in the programming as shown in Figure 5.5B. During stress recovery, the oven was first equilibrated at 160°C for more than one hour. Subsequently, the programed sample and the mold, which were at room temperature, were then placed in the hot oven and let the gripped rod tip touch the middle of the sample but did not apply any force to the rebar. The gripped rod a steel bar; shown in Figure 5.5B. The beam in such configuration is a simply supported three-point bending beam. Because no displacement was allowed during recovery, the recovery of the rebar created force, which was recorded by the MTS machine.

5.2.3. Fabrication of E-glass FRP Rebar Reinforced Concrete Beam

Firstly, the fabricated FRP rebars were placed in the designed molds as showed in the Figure 5.6A. The mold was designed by the ACI 440-15 standard. The width is 37mm and the height is 70mm. The distance between the FRP and the bottom is 12mm. The concrete mix used is QUIKRETE fast-setting concrete mix (50 lb., 10437) purchased from home depot. The strength

can reach to 4000 psi after 28days. The concrete mix was mixed with appropriate water and then it was transferred into the molds as the Figure 5.6B. All samples were placed on the vibration table for 2 minutes after the casing. The samples cured after 14 days are illustrated as the Figure 5.6C. After demolding, the samples for test later are showed in the Figure 5.6D.

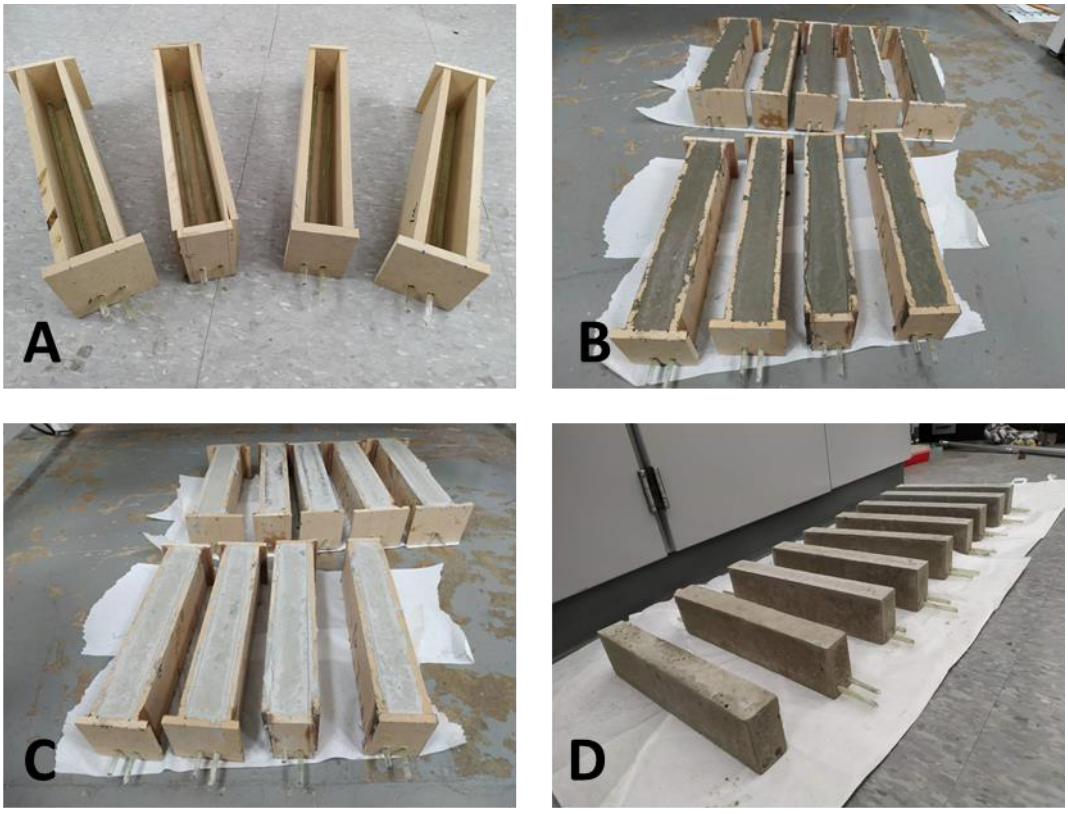

Figure 5.6. The fabrication of the E-glass fiber FRP rebar reinforced concrete beam. (A) The molds with the placed FRP rebar. (B) The cased concrete. (C) The cured samples. (D) The demolded samples for test.

5.2.4. Three-point Bending Test for the FRP Rebar Reinforced Concrete Beam

The three-point bending tests are carried out the setup as the illustrated in the Figure 5.7(A) The distance between the two points on the bottom is 10 inches. The dimension of the beam is showed as the Figure 5.7 (B). The deflection and the loading force are recorded by the MTS machine. The rate for the deflection is 0.5 mm/min.

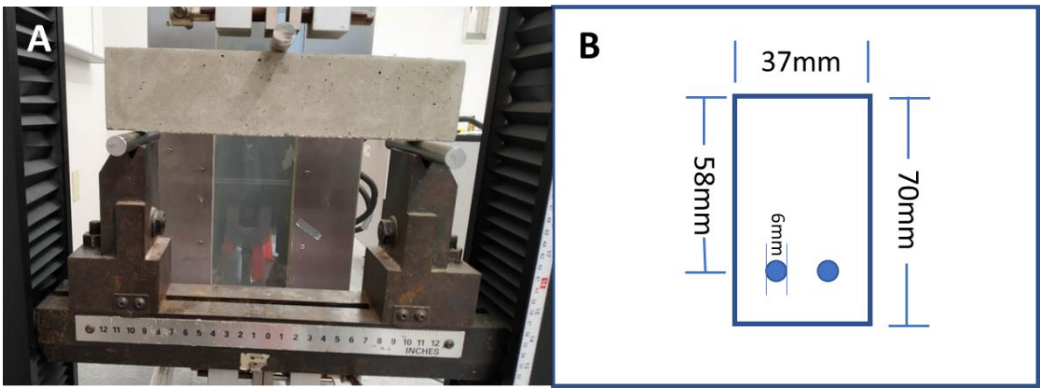

Figure 5.7. (A)Three-point bending test setup for the FRP rebar reinforced concrete beam. (B) The dimension of the concrete beam.

5.3. Result and Discussion

The recovery bending stress is calculated as follow. Based on the equation:

$$\sigma_b = \frac{My}{I}$$

where σ_b is the bending stress. M is the bending moment. In this case, the rebar was a simply supported three-point bending beam, thus $M = 0.5 \times 60\ \text{mm} \times F_r$, where F_r is the recovering force. y is the vertical distance away from the neutral axis and, consequently, it is 3 mm. I is the area moment of inertia. We consider the cross section of the sample is a solid cylinder, hence, $I = \pi d^4/64$. Here d is the diameter of the rebar, which is 6 mm.

From Figure 5.8, the stabilized recovery force is 55 N. Therefore, the maximum recovery bending stress is calculated as follows:

$$\sigma_b = \frac{My}{I} = \frac{0.5 \times 60mm \times 55N \times 3mm}{\pi \times 6^4\ mm^4} \times 64 = 77.8\ MPa$$

The recovery bending stress is a sufficient value for closing the bending cracks at the bottom of a beam. Nevertheless, the curved FRP couldn't be programmed into real straight. And, another issue is the top part of rebar is under the compression. This leads the glass fiber squeezed out or even break the FRP. This limit the possible ability of programming.

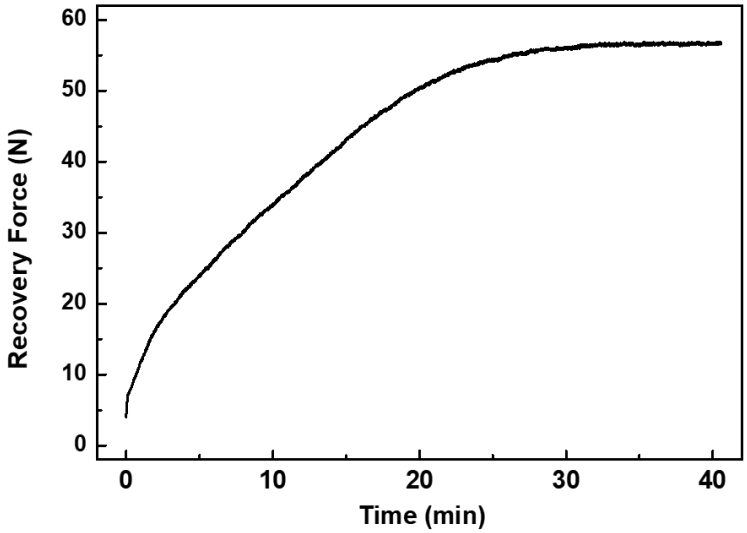

Figure 5.8. Evolution of the recovery force generated by the programmed SMP rebar at 160 °C.

So another strategy is utilized as the following study. The three-point bending data for the plain concrete and reinforced concrete are illustrated in the Figure 5.9. The enhancement of the strength and the deflection can be observed. The cracking process is showed as the Figure 5.10.

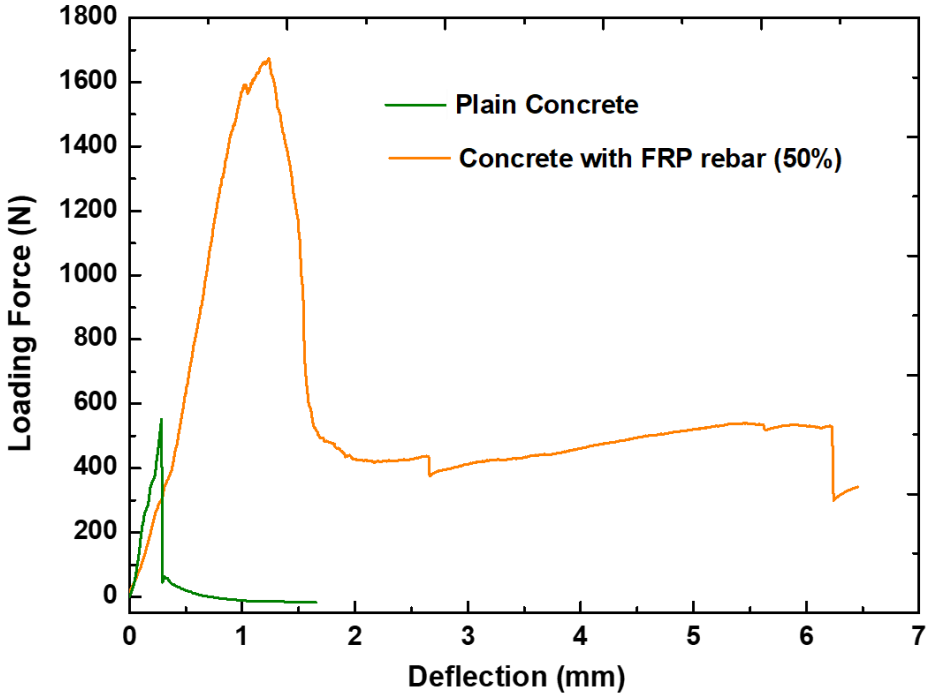

Figure 5.9. The three-point bending test for the plain concrete and the reinforced concrete rebar which the volume fraction of fiber is 50%.

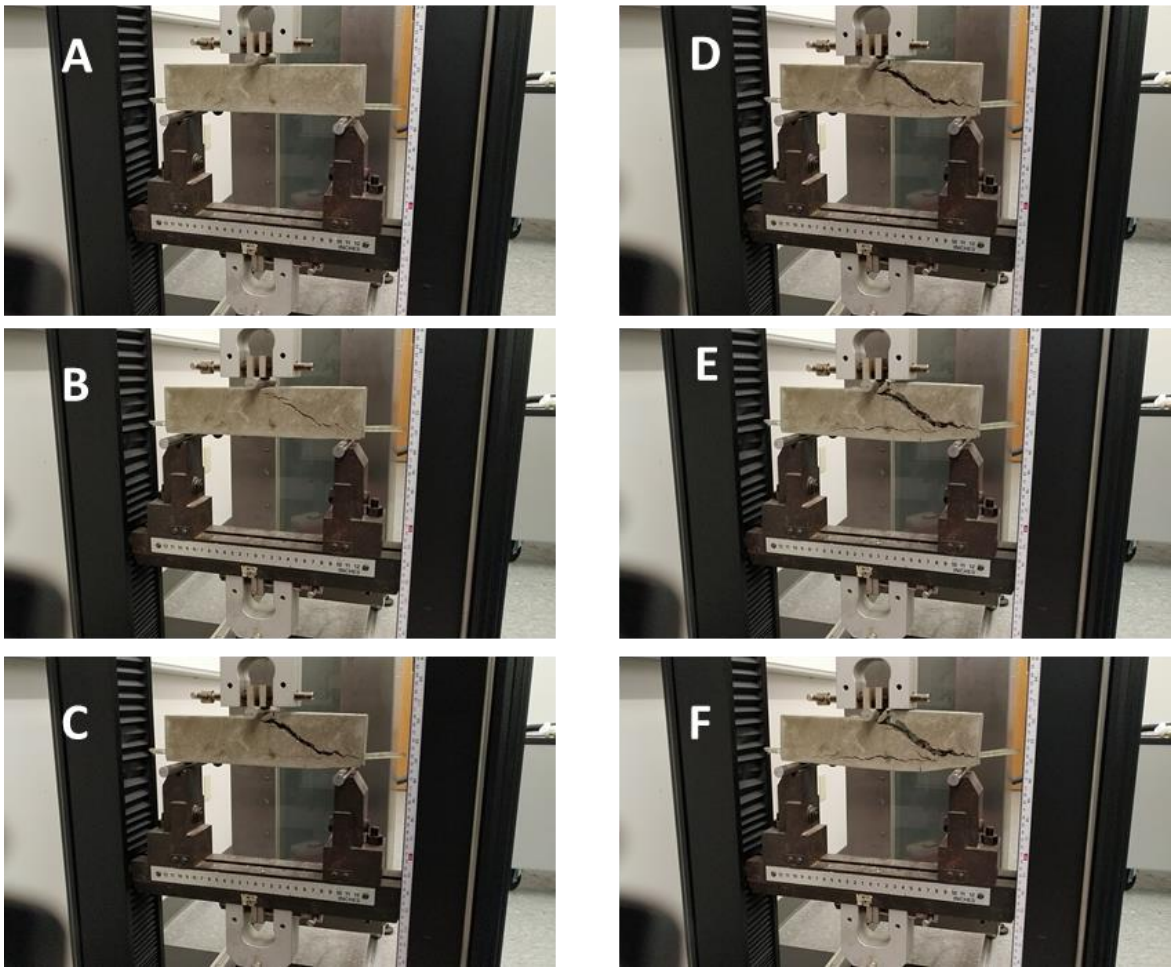

Figure 5.10. The crack process of the concrete beam with the E-glass FRP rebar which the volume fraction of the glass fiber is 50%.

The bending cracks as our designed were not observed. The shearing dominated the cracking. After reconsidering the ratio of the height to length, the sample was cut the top half to obtain a 1/10 ratio which will let the beam bend more than shear. However, the bending induced cracks were not observed neither as showed in the Figure 5.11. The similar situation occurred for the concrete beam with the 70% E-glass fiber volume fraction FRP rebar as the Figure 5.12. This may due to several reasons. Firstly, the strength of the concrete may not strong enough. The high strength concrete and longer curing time may be needed. Secondly, the tensile strength of FRP may be too high. If the FRP is too strong, during the bending process of

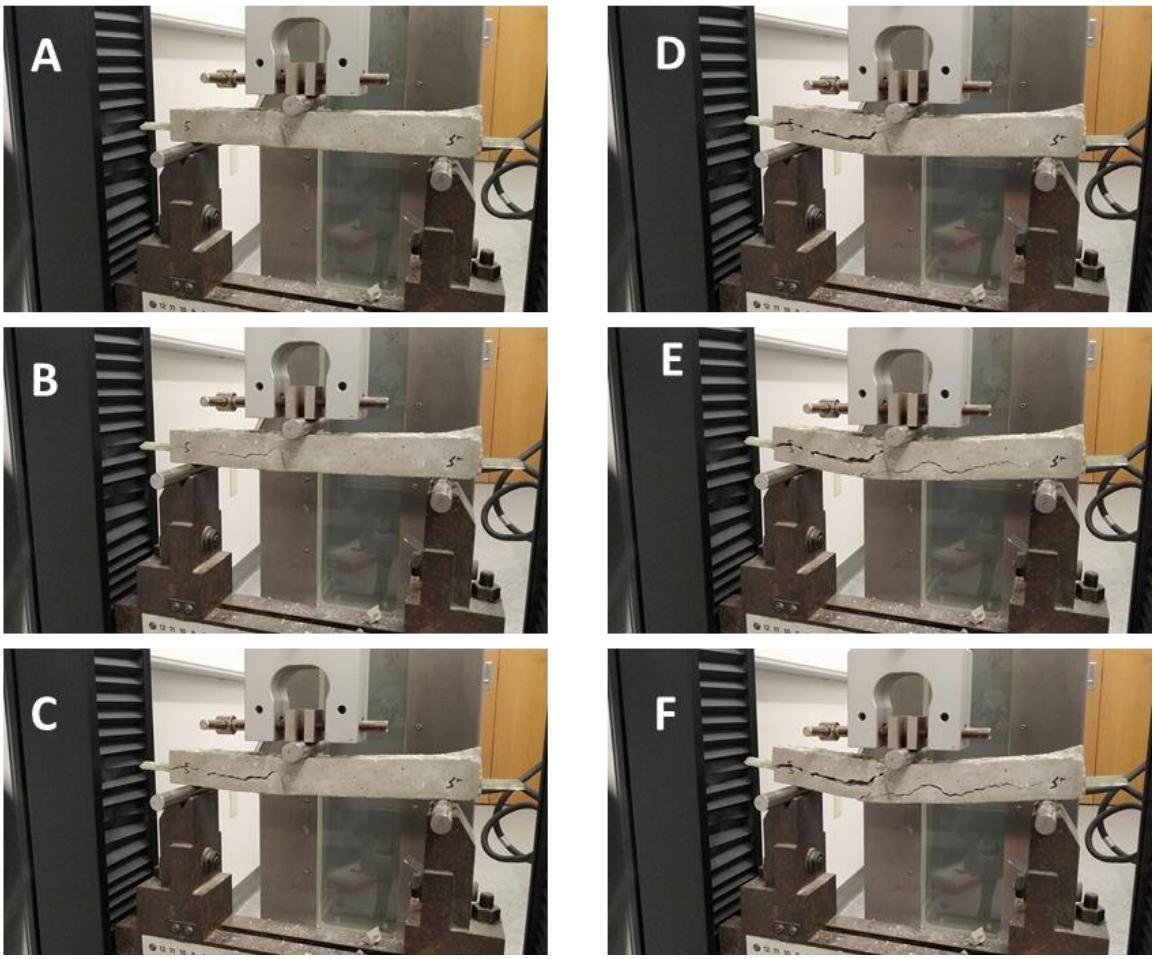

Figure 5.11. The crack process of a concrete beam, which was cut the top half, with the E-glass FRP rebar which the volume fraction of the glass fiber is 50%.

concrete, the bottom half can't really serve as the tension zone. Thirdly, based on the cracks observed in the Figure 5.10 and 5.11, the cracks along the FRP can be observed. This is induced by the shear between the FRP and the concrete matrix which indicating the interaction between the FRP and concrete may not be good enough. The possible method to overcome these problems are discussed in the next chapter for the future work.

5.4. Conclusion

By using the new shape memory polymer EPON-IPD epoxy resin, a strong new type of E-glass fiber FRP rebar reinforced concrete can be obtained. By programming a curved rebar into

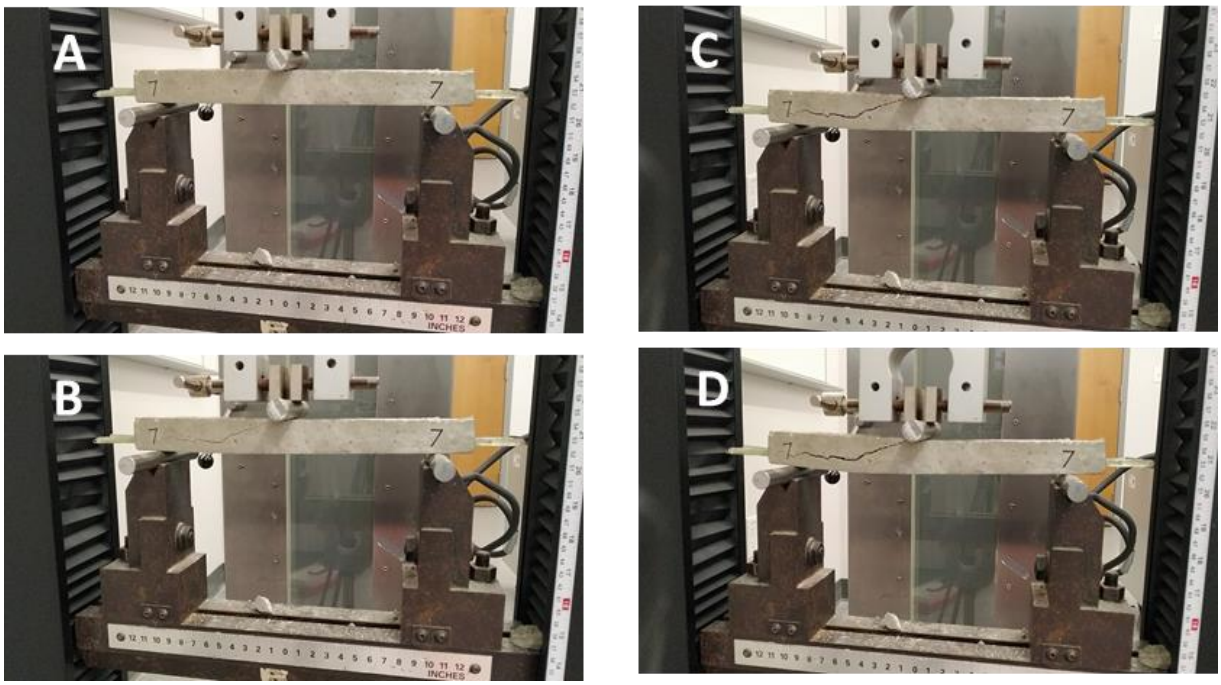

Figure 5.12. The crack process of a concrete beam, which was cut the top half, with the E-glass FRP rebar which the volume fraction of the glass fiber is 70%.

flat, the recovery bending stress as high as 77.8 MPa was achieved. When using the FRP rebar in the concrete beam, the strength can be enhanced and the shearing dominant cracks were observed. For letting the FRP rebar serve for closing the cracks induced by bending, some adjustment should be conducted. The stronger concrete, the narrower FRP and the interaction enhancement can be utilized.

CHAPTER 6 THE FUTURE WORK

The future work includes the further study of the Chapter 5, based on the issues mentioned in it, and it also contains other possible projects can be explored based on the study in Chapter 2 and Chapter 3.

For the project in the chapter 5, the stronger concrete and the less usage of the FRP will be the first step of the future work. To enhance the interfacial bonding between the FRP rebar and the concrete matrix, the FRP can be glued with cured concrete by uncured EPON-IPD resin since this resin itself is a two-component Epoxy adhesive as showed in the Figure 6.1. In this idea, the straight FRP can be utilized as the rebar without threads.

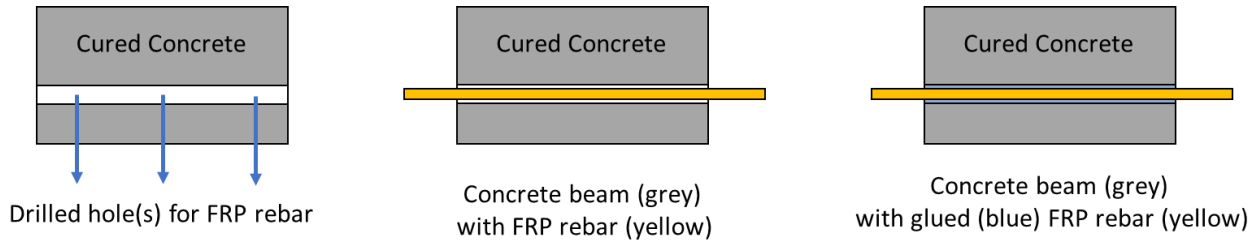

Figure 6.1. The enhancement of the interfacial bonding between concrete beam and FRP rebar by adhesive (EPON-IPD).

As the completed research for chapter 2 and 3, some more possible study can be considered. The thermoset network with other type of steric hindrance can be synthesized and the property can be studied. The thermoset network with the similar or enhanced mechanical property and the shape memory effect can be explored to widen working range of the temperature. By maintaining the necessary property, the wider glass transition temperature for the single network is also can be explored. Some possible molecular structure for the future work has been classified into different catalogs as the Figure 6.2. Besides exploring the new network, fabricating the EPON-IPD into composite is also a direction such as add carbon black or short glass fiber to enhance the mechanical property and adjust the glass transition temperature.

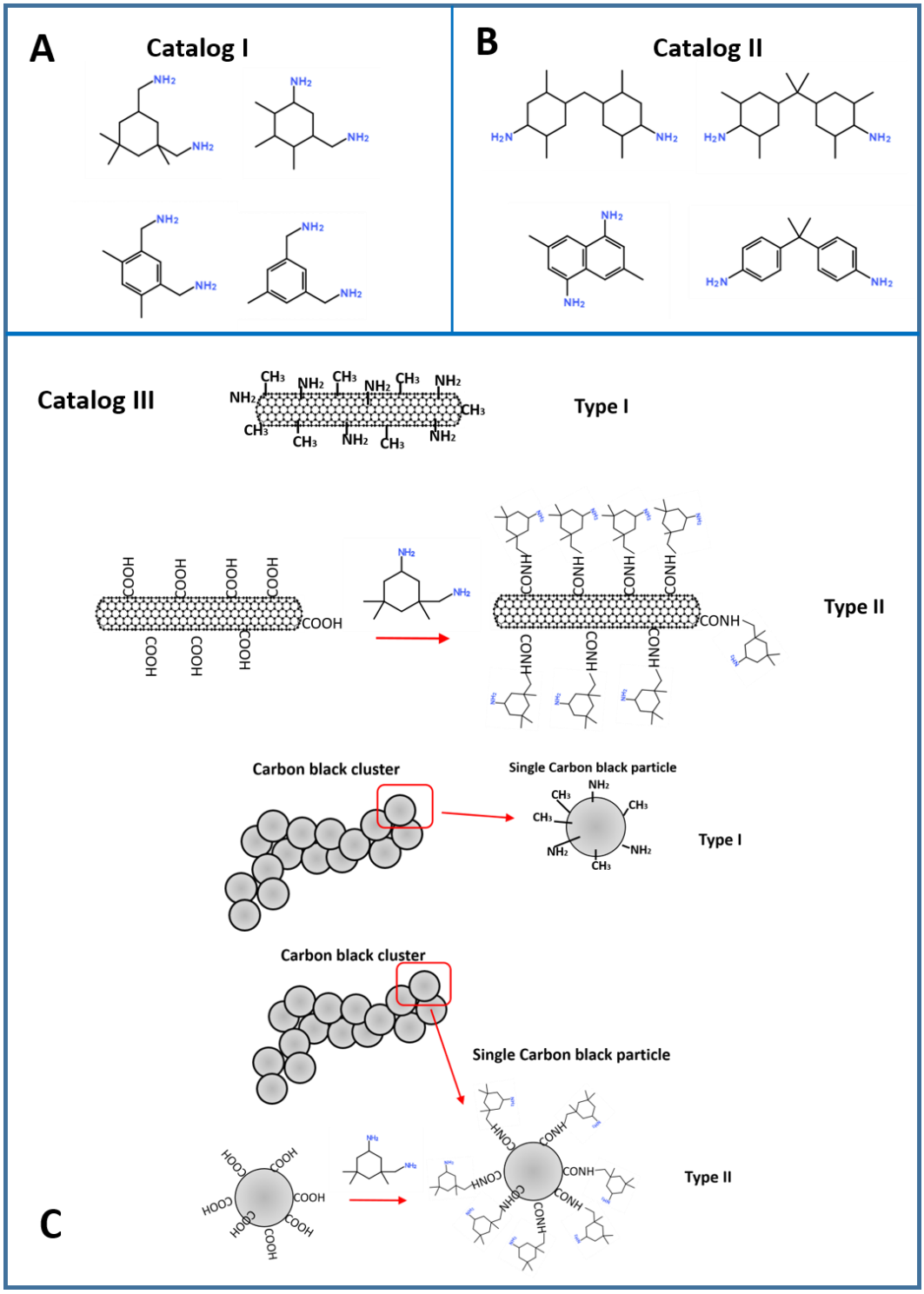

Figure 6.2. Potential molecular structures of amides that can produce enthalpy storage for new thermoset polymer networks.

We think that diamines with rigid cyclic structure which provides the large steric hindrance, such as methyl groups, are potential molecules. They are possible to help the formed thermoset network to store the energy as enthalpy during programming. This catalog of potential molecules are listed in the Figure 6.2A. Moreover, the poly-cyclic and heterocyclic diamines with the groups that can provide steric hindrance are also considered as potential candidates as shown in Figure 6.2B as the second catalog. Other than cyclic, poly-cyclic or heterocyclic structure serving as the rigid structural center, caged structures, such as carbon black, carbon nanotube (CNT) or polyhedral oligomeric silsesquioxanes (POSS), with amino groups, are also possible candidates, once the rigid structural center is surrounded by groups that can provide enough steric hindrance (such as the type I structure shown in Figure 6.2C). We can also graft the IPD onto the surface of acidized carbon black or CNT (such as the type II shown in Figure 6-2C). These structures can be considered as the catalog three. In summary, if the amines have a rigid center, such as cyclic or caged structure, and grafting by these groups may provide steric hindrance, which are the possible chemical structures for the enthalpy storage. Grafting EPON epoxy onto the surface of rigid center such as carbon black, CNT or some nanoparticles, may be another way of synthesizing this type of SMPs.

REFERENCES

1. A. Lendlein, S. Kelch. Shape-memory polymers. *Angew. Chem. Int. Ed.* **41**, 2034-2057, (2002).

2. C. Liu, H. Qin, P.T. Mather. Review of progress in shape-memory polymers. *J. Mater. Chem.* **17**, 1543-1558 (2007).

3. D. M Ratna and J. Karger-Kocsis. Recent advances in shape memory polymers and composites: a review. *J. Mater. Sci.* **43**, 254–269 (2008).

4. W. M. Huang, Z. Ding, C. C. Wang, J. Wei, Y. Zhao, H. Purnawali. Shape memory materials. *Mater. Today* **13**, 54-61 (2010).

5. J. S. Leng, X. Lan, Y. J. Liu, S. Y. Du. Shape-memory polymers and their composites: stimulus methods and applications. *Prog. Mater. Sci.* **56**, 1077-1135, (2011).

6. J. L. Hu, Y. Zhu, H. Huang, J. Lu. Recent advances in shape-memory polymers: structure, mechanism, functionality, modeling and applications. *Prog. Polym. Sci.* **37**, 1720-1763, (2012).

7. H. Meng, G. Li. A Review of stimuli-responsive shape memory polymer composites. *Polymer* **54,** 2199-2221 (2013).

8. Q. Zhao, H. J. Qi, T. Xie. Recent progress in shape memory polymer: new behavior, enabling materials, and mechanistic understanding. *Prog. Polym. Sci.* **49-50**, 79-120 (2015).

9. M. D. Hager, S. Bode, C. Weber, U. S. Schubert. Shape memory polymers: past, present and future developments. *Prog. Polym. Sci.* **49-50**, 3-33 (2015).

10. P. J. Roth, A. B. Lowe. Stimulus-responsive polymers. *Polym. Chem.* **8**, 10-11 (2017).

11. A. Lendlein, R. Langer. Biodegradable, elastic shape-memory polymers for potential biomedical applications. *Science* **296**, 1673-1676, (2002).

12. A. Lendlein, H. Jiang, O. Jünger, R. Langer. Light-induced shape-memory polymers. *Nature* **434**, 879-882, (2005).

13. M. Ma, L. Guo, D. G. Anderson, R. Langer. Bio-inspired polymer composite actuator and generator driven by water gradients. *Science* **339**, 186-189, (2013).

14. X. J. Han, Z. Q. Dong, M. M. Fan, Y. Liu, J. H. Li, Y. F. Wang, Q. J. Yuan, B. J. Li, S. Zhang. pH-Induced Shape-Memory Polymers. *Macromol. Rapid Communi.* **33**, 1055-1060, (2012).

15. Y. Sakata, S. Furukawa, M. Kondo, K. Hirai, N. Horike, Y. Takashima, H. Uehara, N. Louvain, M. Meilikhov, T. Tsuruoka, S. Isoda, W. Kosaka, O. Sakata, S. Kitagawa. Shape-memory

nanopores induced in coordination frameworks by crystal downsizing. *Science* **339**, 193-196, (2013).

16. R. Mohr, K. Kratz, T. Weigel, M. Lucka-Gabor, M. Moneke, and A. Lendlein. nitiation of shape-memory effect by inductive heating of magnetic nanoparticles in thermoplastic polymers. *PANS* **103**, 3540–3545 (2006).

17. P. Miaudet, A. Derré, M. Maugey, C. Zakri, P. M. Piccione, R. Inoubli, P. Poulin. Shape and temperature memory of nanocomposites with broadened glass transition. *Science* **318**,1294-1296, (2007).

18. G. Li, A. Shojaei. A viscoplastic theory of shape memory polymer fibers with application to self-healing materials. *Proc. Roy. Soc. A* **468**, 2319-2346, (2012).

19. N. Lakhera, C. M. Yakachi, T. D. Nguyen, C. P. Frick. Partially constrained recovery of (meth)acrylate shape-memory polymer networks. *J. Appl. Polym. Sci*. **126**, 82-82 (2012).

20. Wang, G. Li, Stress memory of a thermoset shape memory polymer. *J. Appl. Polym. Sci*. **132**, 42112 (2015).

21. M. A. Di Prima, M. Lesniewski, K. Gall, D. L. McDowell, T. Sanderson, D. Campbell. Thermo-mechanical behavior of epoxy shape memory polymer foams. *Smart Mater. Struct.* **16**, 2330–2340 (2007).

22. ASM International. *Atlas of Stress-Strain Curves*-2nd ed. ASM International, OH, (2002).

23. E.L. Kirkby, J.D. Rule, V.J. Michaud, N.R. Sottos, S.R. White, J.A.E. Månson. Embedded shape-memory alloy wires for improved performance of self-healing polymers. *Adv. Funct. Mater*. **18**, 2253-2260, (2008).

24. C.L. Lewis, Y. Meng, and M. Anthamatten. Well-Defined Shape-Memory Networks with High Elastic Energy Capacity. *Macromolecules* **48**, 4918−4926, (2015).

25. G. Li. Self-Healing Composites: Shape Memory Polymer Based Structures. John Wiley & Sons, Inc., West Sussex, UK, (2014).

26. P. M. Ajayan, L. S. Schadler, C. Giannaris A. Rubio. Single-walled carbon nanotube–polymer composites: strength and weakness. Adv. Mater. 12, 750-753 (2000).

27. D. Yang, A. Velamakanni, G. Bozoklu, S. Park, M. Stoller, R. D. Piner, S. Stankovich, I. Jung, D. A. Field, C. A. Ventrice Jr., R. S. Ruoff. Chemical analysis of graphene oxide films after heat and chemical treatments by X-Ray photoelectron and micro-Raman spectroscopy. Carbon 47, 145-152 (2009).

28. G. Hähner. Near edge X-ray absorption fine structure spectroscopy as a tool to probe electronic and structural properties of thin organic films and liquids. Chem. Soc. Rev. 35, 1244-1255 (2006).

29. Koprinarov, A. Lippitz, J. F. Friedrich, W. E. S. Unger, Ch. Wöll. Oxygen plasma induced degradation of the surface of poly(styrene), poly(bisphenol-A-carbonate) and poly(ethylene terephthalate) as observed by soft X-ray absorption spectroscopy (NEXAFS). Polymer 39, 3001-3009 (1998).

30. G. Li, A. Wang. Cold, warm, and hot programming of shape memory polymers. J. Polym. Sci. Part B: Polym. Phys. 54, 1319-1339, (2016).

31. P. B. Bowden. The elastic modulus of an amorphous glassy polymer. Polymer 9, 449-454 (1968).

32. M. Mooney. A theory of large elastic deformation. J. Appl. Phys. 11, 582-592 (1940).

33. M. Mooney. The thermodynamics of a strained elastomer. I. general analysis. J. Appl. Phys. 19, 434-444 (1948).

34. M. Anthamatten, S. Roddecha, and J. Li. Energy Storage Capacity of Shape-Memory Polymers. Macromolecules 46, 4230−4234 (2013).

35. C. C. Hornat, Y. Yang, M. W. Urban. Quantitative predictions of shape-memory effects in polymers. Adv. Mater. 29, 1603334 (2017).

36. P. M. Morse. Diatomic molecules according to the wave mechanics. II. vibrational levels. Phys. Rev. 34, 57-64 (1929).

37. K. Tashiro, G. Wu, M. Kobayashi. Quasiharmonic treatment of infrared and Raman vibrational frequency shifts induced by tensile deformation of polymer chains. J. Polym. Sci. Part B 28, 2527-2553 (1990).

38. R. S. Bretzlaff, R. P. Wool. Frequency shifting and asymmetry in infrared bands of stressed polymers. Macromolecules 16, 1907-1917 (1983).

39. Q. Wei, A.K. Sharma, J. Sankar, J. Narayan. Mechanical properties of diamond-like carbon composite thin films prepared by pulsed laser deposition. Composites: Part B 30, 675–684 (1999).

40. J.J. Aklonis and W.J. MacKnight. Introduction to Polymer Viscoelasticity (2nd Ed.). John Wiley & Sons, (1983).

41. P. J. Flory. Principles of polymer chemistry, Cornell University Press, Ithaca, NY, (1953).

42. W.J. Taylor. Average length and radius of normal paraffin hydrocarbon molecules. J. Chem. Phys. 16, 257-267 (1948).

43. Lossier, H. and Caguol, A. 1944, Expanding cements and their application-self-stressed concrete, Genie Civil (Paris), 121, 61-65.

44. Klein, A. Troxell, G. E., 1958, Studies of calcium sulfoaluminate admixtures for expansive cements, Proceedings. ASTM, 58, 986-1008.

45. Nagataki, S., Gomi, H, 1998, Expansive admixtures (mainly ettringite), Cement and Concrete Composites, 20, 163-170.

46. Parker, P. N., Wahl, W. W., 1966, Expanding cement-A new development in well cementing, Journal of petroleum technology, 18, 559-564.

47. Garter, L. G., Waggoner, H. F., George C., 1966, Expanding cements for primary cements, 18.

48. Mo L., Deng M., Tang M., 2010, Effect of calcination condition on expansion property of MgO-type expansive agent used in cement-based materials, 40, 437-446.

49. Mo L., Meng L., Al-Tabbaa A., Deng M., 2015, Deformation and mechanical properties of the expansive cements produced by inter-grinding cement clinker and MgOs with various reactivities, Construction and building materials, 80, 1-8.

50. Saidin S., Sonny I., Nuruddin M. F., 2008, A new approach for optimizaing cement design to elimate microannulus in steam injection wells, International petroleum technology conference, Kuala Lumpur, Malaysia, SPE paper No. IPTC-12407-MS.

51. Dahi Taleghani, A., Li, G., Moayeri, M., 2017. Smart Expandable Cement Additive to Achieve Better Wellbore Integrity. J. Energy Resour. Technol. 139, 062903.

52. Santos, L., Taleghani, A.D., Li, G., 2018. SPE-191822-18ERM-MS Smart Expandable Polymer Cement Additive to Improve Zonal Isolation 7–11.

53. Kinik, K., Wojtanowicz, A.K., 2011. Environmental Risk of Sustained Casing Pressure. SPE Am. E&P Heal. Safety, Secur. Environ. Conf. 459–467.

54. Jiang, M., Michael Griffin, W., Hendrickson, C., Jaramillo, P., Vanbriesen, J., Venkatesh, A., 2011. Life cycle greenhouse gas emissions of Marcellus shale gas. Environ. Res. Lett. 6.

55. Dahi Taleghani, A., Wang, W., 2016. Emergence of Delamination Fractures Around the Casing and Its Stability. J. Energy Resour. Technol. 139, 012904.

56. Baumgarte, C., Thiercelin, M., Klaus, D., 1999. Case Studies of Expanding Cement To Prevent Microannular Formation, in: SPE Annual Technical Conference and Exhibition. Society of Petroleum Engineers, Houston, TX.

57. Bois, A.-P., Garnier, A., Rodot, F., Sain-Marc, J., Aimard, N., 2011. How To Prevent Loss of Zonal Isolation Through a Comprehensive Analysis of Microannulus Formation. SPE Drill. Complet. 26, 13–31.

58. Vignes, B., Safety, P., Aadnoy, B.S., 2008. SPE / IADC 112535 Well-Integrity Issues Offshore Norway, in: SPE/IADC Drilling Conference. Orlando, p. 8.

59. Chenevert, M.E., Shrestha, B.K., 1987. Shrinkage Properties of Cement, in: Annual Technical Conference and Exhibition of the Society of Petroleum Engineers. pp. 49–57.

60. De Andrade, J., Sangesland, S., Todorovic, J., Vrålstad, T., 2015. Cement Sheath Integrity During Thermal Cycling: A Novel Approach for Experimental Tests of Cement Systems, in: SPE Bergen One Day Seminar. Bergen, p. 16.

61. Jafariesfad, N., Gong, Y., Geiker, M.R., Skalle, P., 2016. Nano-Sized MgO with Engineered Expansive Property for Oil Well Cement Systems, in: SPE Bergen One Day Seminar.

62. Thomas, J., Musso, S., Catheline, S., Chougnet-Sirapian, A., Allouche, M., 2014. Expanding Cement For Improved Wellbore Sealing: Prestress Development, Physical Properties, And Logging Response, in: SPE Deepwater Drilling and Completions Conference.

63. Nelson, E.B.&, Guillot, D., 2006. Well Cementing, 2nd ed. Schlumberger.

64. Goboncan, V.C., Dillenbeck, R.L., 2003. Real-Time Cement Expansion / Shrinkage Testing Under Downhole Conditions For Enhanced Annular Isolation. Proc. SPE/IADC Drill. Conf. l, 1–9.

65. van Eijden, J., Cornelissen, E., Ruckert, F., Wolterbeek, T., 2017. Development of Experimental Equipment and Procedures to Evaluate Zonal Isolation and Well Abandonment Materials, in: SPE/IADC Drilling Conference and Exhibition.

66. N. S. Klein, J. Bachmann, A. Aguado, B. Toralles-Carbonar, 2012. Evaluation of the wettability of mortar component granular materials through contact angle measurement. Cement and Concrete Research. 42, 1611-1620.

67. H. A. Abdalla, 2002. Evaluation of deflection in concrete members reinforced with fibre reinforced polymer (FRP) bars. Composite Structure, 56, 63-71.

68. A. K. EI-Sayed, E. EI-Salakawy, B. Benmokrane, 2007. Mechanical and structure characterization of new carbon frp stirrups for concrete members. Journal of Composite Construction, 11, 352-362.

69. C. M. L. Tavares, M. C. S. Ribeiro, A. J. M. Ferreira, R. M. Guedes, 2002. Creep behavior of FRP-reinforced polymer concrete. Composite Structures, 57, 47-51.

VITA

Jizhou Fan was born and grew up in Harbin, China. He earned his Bachelor of Science degree for applied chemistry major from Sun-Yet Sen University (SYSU) in 2010. During his time in SYSU, he published two journal papers and obtained the best undergraduate student thesis award in department of chemistry and chemical engineering by the supervision from Dr. Liqun yang. He joined the department of chemistry in Central Michigan University (CMU) in the fall of 2010 for pursuing the Master of Science degree. He published two first author papers and one co-author paper during this three-year studying supervised by Dr. Bingbing Li. He started his doctoral study in Louisiana State University (LSU) in the fall of 2013 and joined into Dr. Guoqiang Li's polymer material and composite group in department of mechanical and industrial engineering since the fall of 2014. By Dr. Li's educating, advising and inspiring, seven journal papers have been published. One of them was published on the Nature Communication in 2018. He obtained his outstanding research assistant award of department of mechanical and industrial engineering for the academic year between 2017-2018. One undergraduate student supervised by him won the first place of poster presentation competition in summer research experiences for undergraduates (REU) program.